NTNU – Trondheim
Norwegian University of
Science and Technology

Design and Analysis of an X-band Phased Array Patch Antenna

Fredrik Gulbrandsen

Electronics Engineering
Submission date: June 2013
Supervisor: Egil Eide, IET
Co-supervisor: Asgeir Nysæter, FFI

Norwegian University of Science and Technology
Department of Electronics and Telecommunications

Project Description

The goal is to design and analyze an X-band (8-9 GHz) antenna array. The starting point will be a developed X-band aperture coupled stacked patch antenna element that is to be modified and used as the antenna element in the array antenna.

Key tasks will be to achieve satisfactory impedance, antenna pattern and polarization over the desired scan range and frequency bandwidth by including the effect of mutual coupling between the antenna elements. Other tasks will be to reduce backwards radiation and scan angles with zero antenna effect due to destructive interference.

The design should be simulated with contacts for connection to a nearby TX/RX module, and it should be able to handle the temperature rise due to 50 W power amplifiers. The goal is to arrive at a design that can be demonstrated in a functional model.

If time permits the task also includes testing of the finished antenna in an anechoic chamber with the reporting of test results and comparisons with and comparisons with simulated results.

Abstract

An 8x8 array antenna has been designed for a frequency band of 8-8.5 GHz. The design has been made as a part of a project to develop a digital, active MIMO radar at the Norwegian Defence Research Establishment (FFI).

The array consists of 64 resonant aperture stacked patch (ASP) antennas. An element spacing of 16.5 mm ensures that no grating lobes occur over the entire scan range. A scan range of -55° to 55° and -45° to 45° have been achieved in the E-plane and H- plane respectively. This scan range was achieved using wide band antenna elements.

Methods to improve the scan range and the reflection coefficient such as electromagnetic bandgap (EBG) material, defected ground structures (DGS), and adaptive matching circuits was investigated. All three alternatives were discarded due to either added complexity to the design or problems incorporating the methods into the design.

The array has achieved a half power beam width of 14° when scanned in broadside direction. The efficiency of the array is 0.96 which is an important result considering that 50 W is to be applied to each element.

The antenna element used in the array was based on a design developed during the specialization project. Measurements on this antenna element were conducted and large deviations between measured and simulated input impedance were discovered. These deviations were found to be caused by mechanical properties of the antenna element. The antenna element was improved and better compliance between measured and simulated results has been achieved.

Sammendrag

Et 8x8 array antenne har blitt designet for et frekvensbånd på 8-8,5 GHz . Designet er utført som en del av et prosjekt for å utvikle en digital, aktiv MIMO radar på Forsvarets forskningsinstitutt (FFI).

Arrayet består av 64 resonant aperture stacked patch (ASP) antenner. En element avstand på 16,5 mm sikrer at ingen gitterlober oppstår for skanneområde. En skannområde på -55 ° -55 ° og -45 ° -45 ° er oppnådd i E-planet og H-planet respektivt. Dette skanneområde ble oppnådd ved hjelp av antenne elementer med et bredt frekvensbånd.

Metoder for å forbedre skanneområde og refleksjon koeffisienten som elektromagnetisk båndgap (EBG) materialer, defekte jordplan strukturer (DGS), og adaptive matchende kretser ble undersøkt. Alle tre alternativer ble forkastet på grunn av enten lagt kompleksiteten i design eller problemer med å gjøre det arbeidet.

Array antennen har oppnådd en half power beam width på 14° i bredside retningen. Strålingseffektiviteten til matrisen er 0,96, noe som er et viktig resultat tatt i betraktning at 50 W inngangs effekten på hvert element

Antennen element som brukes i arrayet var basert på et design utviklet i løpet av spesialiseringsprosjektet. Målinger på dette antenne elementet ble gjennomført og store avvik mellom målt og simulert inngangsimpedans ble oppdaget. Disse avvikene ble funnet å være forårsaket av de mekaniske egenskapene til antenneelementet. Antenneelementet ble forbedret og bedre samsvar mellom de målte og simulerte resultater har blitt oppnådd.

Preface

This thesis is submitted in partial fulfillment of the requirements for the degree of master of science at the Department of Electronics and Telecommunications, Norwegian University of Science and Technology (NTNU). The work was conducted during the winter and spring of 2013 under the supervision of Egil Eide and was submitted to NTNU June 17th, 2013. The assignment was given by the Norwegian Defence Research Establishment (FFI) as part of a project to develop an experimental MIMO radar.

Acknowledgments

First and foremost I want to thank my supervisor at FFI Asgeir Nysæter for the opportunity to work with this project and for facilitating the work. His help has been invaluable to the project, he has provided me with all necessary tools and equipment for solving the assignment and for that I am very grateful.

I also want to thank Yoann Paichard and Karina Vieira Hoel their technical insight has been very helpful.

Last but not least I want to thank Egil Eide my supervisor at NTNU for coffee and waffles at meetings, and of course valuable advice on the antenna design and the report.

Trondheim, Norway, June 2013
Fredrik Gulbrandsen

Contents

List of figures

List of tables

Acronyms

ACSP - Aperture- Coupled Stacked Patch antenna

ASP - resonant Aperture Stacked Patch antenna

DGS - Defected Ground Structure

EBG - Electromagnetic BandGap

HPBW - Half-Power BeamWidth

MIMO - Multiple Input Multiple Output

PA - Power Amplifier

TE- Transverse Electric

TEM - Transverse ElectroMagnetic

TM- Transverse Magnetic

VSWR - Voltage Standing Wave Ratio

1 Introduction

This report presents the design and analysis of an X-band 8x8 phased array patch antenna. The antenna will be used in an active radar system for experimenting with MIMO algorithms. The antenna is designed to have a center frequency of 8.25 GHz and a frequency band of 8-8.50 GHz. The work presented here is the continuation of last fall's specialization project where an aperture-coupled stacked patch antenna was designed. This antenna has been used as a building block for the array antenna.

The report consists of seven chapters. After the introduction the necessary theoretical background is presented. Then a chapter describing the antenna element follows, including a short summary of the design, and a comparison between measured and simulated results. The design of the array and all the steps and choices made are thoroughly explained in chapter four. Important results are presented in chapter five, and then discussed in the next chapter. In the end the conclusion follows.

1.1 Background

Today radar systems are used in many different applications, from large military systems which are used to detect ballistic missiles, to smaller commercial systems as car radars. To increase the range of possible applications much emphasis is put on developing cheap and compact radar systems. In many applications it is desirable to use phased array antennas, this often leads to expensive and large radar systems which limits the possible applications. However, the development of patch antennas has enabled cheap, lightweight, and compact phased array antennas. Combining patch arrays with new semiconductor circuits it is now possible to make cheaper and more compact radar systems.

Work is constantly being done to discover new ways of improving radar performance. Recently it has been discovered that use of Multiple Input Multiple Output (MIMO) techniques have the potential to enhance radar performance. MIMO techniques was originally developed for wireless communication systems to increase capacity. Development of a MIMO radar is currently being conducted at FFI (Forsvarets Forskningsinstitutt). The goal is to build an active radar system with a phased array antenna to test MIMO algorithms. This report presents the design of the phased array antenna.

A project goal has been to build a cheap and compact 8x8 array using patch antenna elements. The array should be designed for a frequency band of 8-8.5 GHz and should be linearly polarized. Goals during the antenna development have been to achieve a high scan range, a high radiation efficiency and a low reflection coefficient. Each antenna element need to handle up to 50 W of input power and the system impedance is 50 Ω.

The antenna element used in the array was developed in the specialization project last fall [1]. An aperture-coupled stacked patch antenna was designed with a frequency band of 8-8.5 GHz. It has been produced and measured results are presented later in the report.

2 Theoretical background

This chapter presents the most important theoretical background used in the design of the array. This project is based on work done in the specialization project conducted last fall (2012), this work is described in [1]. Topics such as antenna parameters, microwave theory and patch antennas are presented in [1]. These topics are of importance for this project as well, but to keep the page number down and the focus on array antennas it was chosen to put these topics in Appendix A.

2.1 Array

An array antenna consists of multiple antenna elements which are grouped together to form one antenna. Grouping antenna elements together results in several advantageous properties such as; higher directivity compared to a single antenna element, it enables electronic steering of the beam, and control over the radiation pattern (i.e. control over side lobe levels, and null points). These properties are mainly due to the positive and negative interference that occur when the fields from each antenna elements combine. The antenna elements need not be identical, but identical antenna elements makes the analysis easier and is more practical in most applications. The radiation properties of an array antenna are controlled by the antenna element, the geometry of the array, and the amplitude and phase of the excitation of each element.

In this section two different ways of modeling arrays are presented and compared; first the classic approach, then an approach using Floquet analysis. Important topics such as mutual coupling, scanning, scan blindness and grating lobes are also discussed.

2.1.1 Classic array analysis

Classic array analysis uses the superposition principle where the total field is obtained by vector adding the fields produced by each antenna element. Figure 1(a) shows a linear array of N identical elements. The radiated electrical field from a single element at an observation point (r, θ, φ) can be expressed as [2, p. 2]

$$\boldsymbol{E}_{se} = A\frac{e^{-jk_0 r}}{r}\boldsymbol{E}_{ep}(\theta, \varphi) \tag{2.1}$$

where A is the amplitude of the input excitation, r is the distance from the antenna element to the observation point and $\boldsymbol{E}_{ep}(\theta, \varphi)$ is the element pattern.

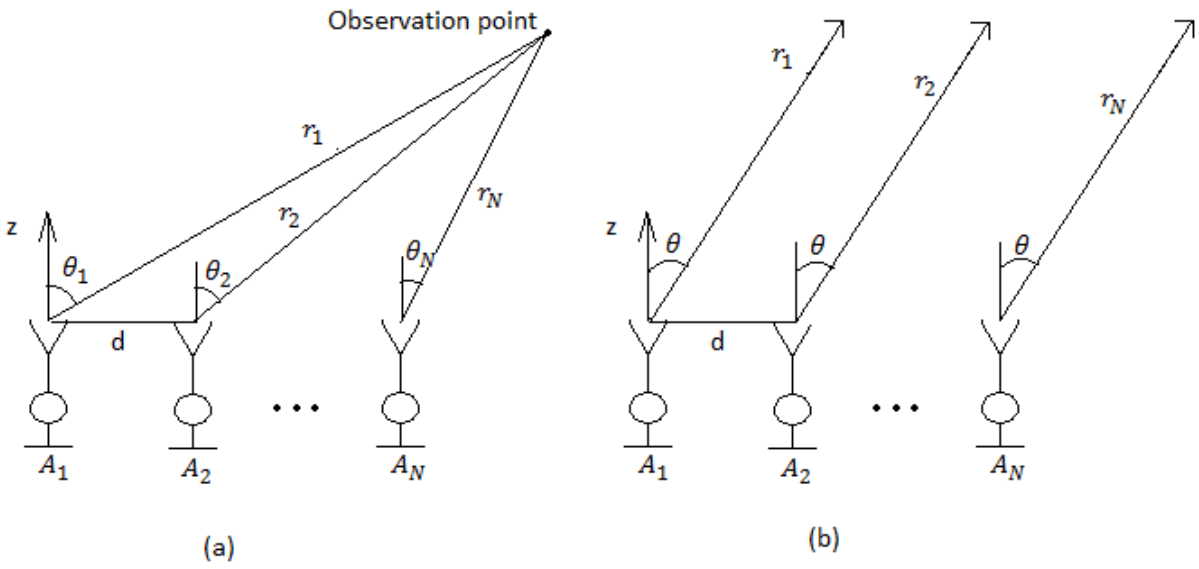

Figure 1: (a) Linear array. (b) Linear array where the observation point is placed in the far field.

The total field of the array is the vector sum of the fields from the antenna elements

$$\boldsymbol{E}_t = A_1 \frac{e^{-j(k_0 r_1)}}{r_1} \boldsymbol{E}_{ep}(\theta_1, \varphi_1) + A_2 \frac{e^{-j(k_0 r_2 - \beta)}}{r_2} \boldsymbol{E}_{ep}(\theta_2, \varphi_2) + \cdots + A_N \frac{e^{-j(k_0 r_N - (N-1)\beta)}}{r_N} \boldsymbol{E}_{ep}(\theta_N, \varphi_N). \tag{2.2}$$

Here β is the phase difference between elements. Assuming the observation point is located in the far-field, several simplifications can be made as shown in Figure 1(b). Mathematically the simplifications are

$$\begin{gathered} \theta_1 \simeq \theta_2 \simeq \cdots \simeq \theta_N \\ \varphi_1 \simeq \varphi_2 \simeq \cdots \simeq \varphi_N \\ r_n \simeq r_1 - (n-1) d \, sin\theta \, cos\varphi \quad \text{for phase variations} \\ r_n \simeq r_1 \simeq \cdots \simeq r_N \quad \text{for amplitude variations} \end{gathered} \tag{2.3}$$

where d is the element spacing. A looser approximation of r_n can be used for the amplitude term since $1/r$ changes slowly. For the phase term a much stricter approximation must be used since e^x changes rapidly. Inserting these approximations into (2.2) gives

$$\boldsymbol{E}_t = A_1 \frac{e^{-jk_0 r_1}}{r_1} \boldsymbol{E}_{ep}(\theta_1, \varphi_1) + A_2 \frac{e^{-j(k_0(r_1 - d\,sin\theta\,cos\varphi) - \beta)}}{r_1} \boldsymbol{E}_{ep}(\theta_1, \varphi_1) + \cdots + A_N \frac{e^{-j(k_0(r_1 - (N-1)d\,sin\theta\,cos\varphi) - (N-1)\beta)}}{r_1} \boldsymbol{E}_{ep}(\theta_1, \varphi_1) \tag{2.4}$$

which can be written as

$$\boldsymbol{E}_t = \frac{e^{-jk_0 r_1}}{r_1} \boldsymbol{E}_{ep}\,(\theta_1, \varphi_1)\,(A_1 + A_2 e^{j(k_0 d\,sin\theta\,cos\varphi + \beta)} + \cdots + A_N e^{(N-1)j(k_0 d\,sin\theta\,cos\varphi + \beta)}). \tag{2.5}$$

This expression can be divided into two parts

$$\boldsymbol{E}_t = \boldsymbol{E}_{se} \times AF \tag{2.6}$$

where $\boldsymbol{E}_{se}$ is the field produced by a single element as given in (2.1), and AF is the array factor depending on the geometry of the array, and amplitude and phase difference of the excitation.

$$AF = \sum_{n=1}^{N} A_n\, e^{j(n-1)(k_0 d\,sin\theta\,cos\varphi + \beta)} \tag{2.7}$$

(2.6) is called pattern multiplication and is valid when the array consists of identical elements.

This analysis has not taken into account mutual coupling between elements. Mutual coupling will lead to different element patterns for each element and therefore the pattern multiplication is not valid.

2.1.1.1 Array factor

To get a deeper understanding of the array factor equation (2.7) is applied to a linear uniform array[1] located on the x-axis. The array factor can then be written as

$$AF = \sum_{n=1}^{N} e^{jk_0(n-1)(d\,sin\theta + \beta)} \tag{2.8}$$

[1] Same spacing and amplitude of excitation.
[2] Software used in the design.

which again can be written as [3, p. 294]

$$AF = \frac{1}{N}\left[\frac{sin\left(\frac{N}{2}\psi\right)}{sin\frac{1}{2}\psi}\right] \tag{2.9}$$

where

$$\psi = k_0 d\ sin\theta + \beta. \tag{2.10}$$

Equation (2.9) is the normalized array factor of a linear array located on the x-axis. Figure 2 shows (2.9) for various values of N and d. It should be noted that a larger N gives a narrower major lobe. A larger element spacing will also give a narrower major lobe. This means that the directivity of an array can be increased by either increasing the number of elements or the element spacing. It is also seen that increasing N gives a lower side lobe level.

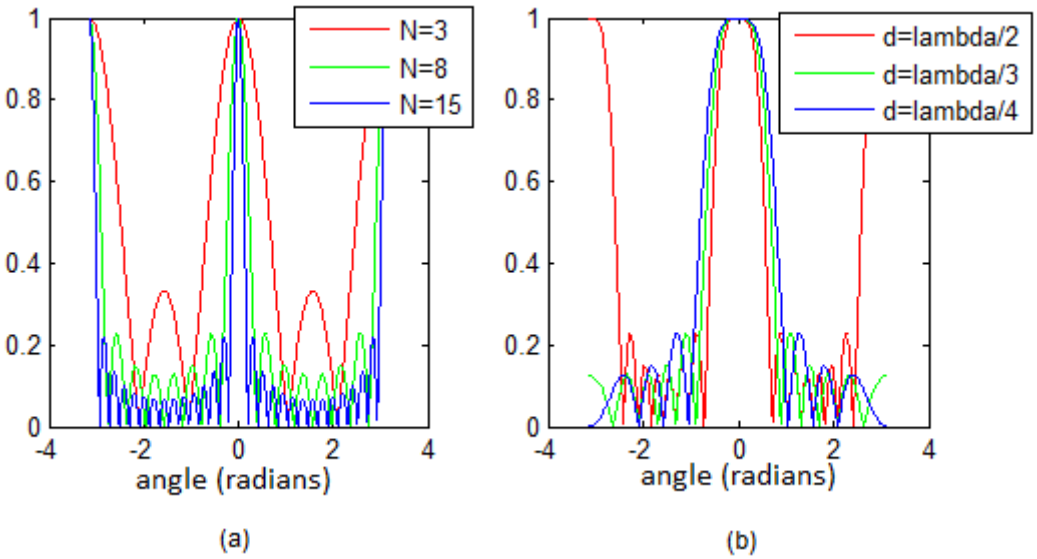

Figure 2: Plot of the normalized array factor using different numbers of elements(a), and different element spacing (b).

Because of the periodic nature of the sine function, equation (2.9) has an infinite number of maxima. These are found using

$$\tfrac{1}{2}(k_0 d\ sin\theta + \beta) = \pm m\pi \qquad m = 0, 1, 2, \ldots \tag{2.11}$$

and they are located at

$$\theta = sin^{-1}\left[\frac{-\beta \pm 2m\pi}{k_0 d}\right] \qquad m = 0, 1, 2, \ldots \tag{2.12}$$

The first maximum is called the major lobe and occurs when

$$k_0 d\ sin\theta + \beta = 0. \tag{2.13}$$

The other maxima are called grating lobes. Grating lobes are unwanted in most applications since they transmit and receive energy in unwanted directions. Grating lobes occur when the spacing between elements are large enough to permit in-phase addition of radiated fields in more than one direction [3, p. 352]. To avoid grating lobes the array should be designed so that $|k_0\ d\ cos\theta + \beta| < 2\pi$. Solving with respect to d gives

$$d_{max} < \left|\frac{\lambda_0 - \beta_{max}}{sin\theta_{max}}\right|. \tag{2.14}$$

where $k_0 = 2\pi/\lambda_0$. β_{max} is the largest phase difference and is found using (2.16). Inserting (2.16) into (2.14) gives

$$d_{max} < \left|\frac{\lambda_0}{sin\theta_{max} - sin\theta_{Smax}}\right|. \tag{2.15}$$

θ_{max} is chosen so that d_{max} is minimized, this is the angle where the first grating lobe will occur. θ_{Smax} is the scan angle that maximizes β. The largest value the denominator of equation (2.15) can achieve is 2, this happens when $\theta_{Smax} = \pm 90°$. Making the element spacing less than $\lambda_0/2$ will therefore ensure that no grating lobes occur for any scan angle. Equation (2.15) can be used to optimize the element spacing for a given scan angle.

2.1.1.2 Scanning

By varying β in (2.13) the direction of the major lobe can be steered. This is called phase steering and is widely used in many applications such as radar and communication systems. It makes it possible to change the direction of the major lobe without moving the antenna mechanically. To determine what phase difference to use for a wanted scan angle θ_S (2.13) is solved with respect to β.

$$\beta = -k_0 d\ cos\theta_S \tag{2.16}$$

For a scan range of 0°-180°, β has to vary from $-k_0 d$ to $k_0 d$.

When the major lobe is pointed in a direction that is perpendicular to the array it is called a broadside array, $\beta = 0$ is needed to achieve this. When the major lobe is pointed in a

direction that is parallel to the array it is called an end fire array, $\beta = \pm k_0 d$ is needed to achieve this. The radiation pattern of an end fire array is shown in Figure 3(a).

To avoid grating lobes when scanning an array, equation (2.15) can be used. It gives an upper limit on the element spacing. Choosing the element spacing just smaller than d_{max} will ensure that the grating lobe will not reach maximum strength, but a large lobe will still be present. This can be seen in Figure 3(b), where the array factor of a linear array in end fire mode is plotted. The element spacing is $\lambda_0/2.1$. It is observed that a large part of the grating lobe is still present. To further reduce this lobe the element spacing should be decreased.

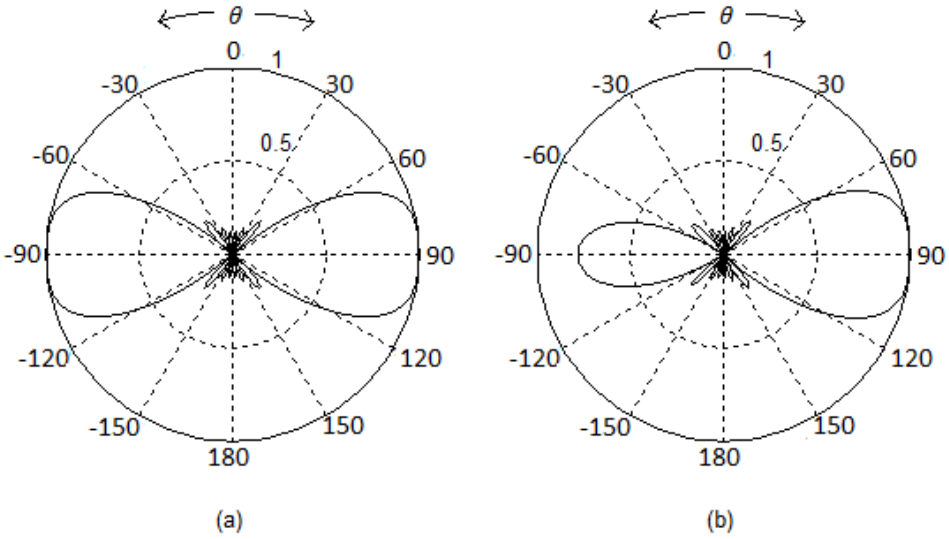

Figure 3: Array factor of a linear array in end fire mode (a) $d = \lambda_0/2$ (b) $d = \lambda_0/2.1$

When scanning an array a phenomenon called beam broadening will occur. An array has the narrowest main beam at broadside, but the main beam will broaden when scanned away from broadside. This can be seen from the directivity equation for a broadside array [3, p. 315]

$$D_0 \simeq 2\left(1 + \frac{L}{d}\right)\left(\frac{d}{\lambda_0}\right) \tag{2.17}$$

D_0 is the maximum directivity of the array, which is an indication on the width of the main beam, and L is the total length of the array. As seen in Figure 4 the effective length of the array will be reduced when the beam is scanned away from broadside. Effective length is defined as the length of the array seen from the observation point.

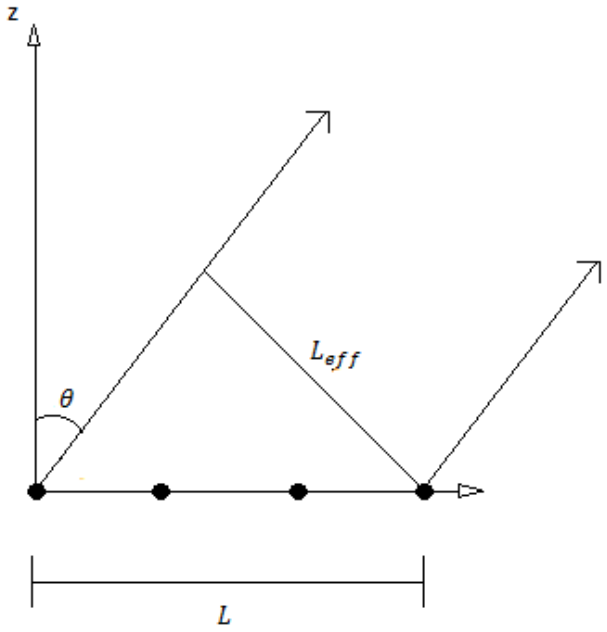

Figure 4: Effective length of a scanned array.

The effective length is given by

$$L_{eff} = L\cos\theta. \tag{2.18}$$

To determine the beam broadening factor, the directivity for a variable scan angle θ_S is divided by the maximum directivity.

$$\frac{D(\theta_S)}{D_0} = \frac{2\left(1+\frac{L_{eff}}{d}\right)\left(\frac{d}{\lambda_0}\right)}{2\left(1+\frac{L}{d}\right)\left(\frac{d}{\lambda_0}\right)} = \frac{\left(1+\frac{L\cos\theta_S}{d}\right)}{\left(1+\frac{L}{d}\right)} \simeq \cos\theta_S \tag{2.19}$$

The last step can be done if $L \gg d$. Equation (2.19) says that the maximum directivity of an array at any scan angle θ_S is the maximum directivity of an array in broadside reduced by a factor of $\cos\theta_S$, or mathematically

$$D(\theta_S) = D_0\ \cos\theta_S \tag{2.20}$$

where D_0 is given by equation (2.17). This is a crude first order approximation of the beam broadening effect, but it illustrates the point.

A more precise model of the beam broadening is given in [3, p. 304]. Here the half-power beamwidth is given as a function of scan angle

$$\Theta_h = cos^{-1}\left[\sin\theta_S - 0.443\frac{\lambda_0}{L+d}\right] - cos^{-1}\left[\sin\theta_S + 0.443\frac{\lambda_0}{L+d}\right] \quad (2.21)$$

Equation (2.21) is accurate around broadside and becomes less accurate for scan angles closer to end fire.

To compare these two methods both equation (2.20) and (2.21) are plotted in Figure 5.

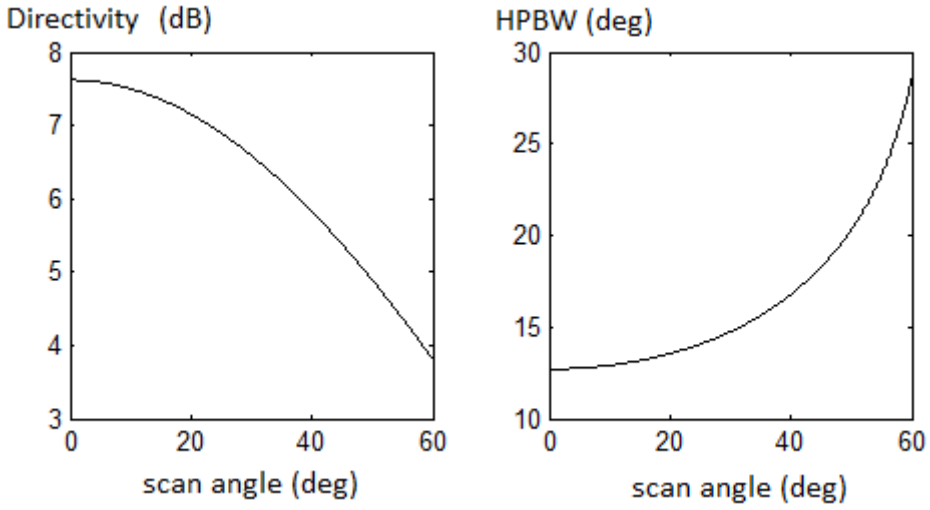

Figure 5: (a) Plot of $D_0\ cos\theta_S$. (b) Half-power beamwidth plotted against scan angle

When comparing the two plots in Figure 5 one has to remember that the directivity and the half-power beamwidth has opposite characteristics (when the directivity increases the HPBW decreases). When doing that it is clear that the two models have similar but inverse characteristics.

Beam broadening is a limiting factor in phase-steered array antennas being used in radar applications. The reason for this is that the angular resolution of a radar is determined by the half-power beamwidth [3, p. 43]. A large beamwidth gives a low angular resolution. The beamwidth will increase as the beam is scanned away from broadside, thus lowering the angular resolution. In order to satisfy the angular resolution requirement, the array should be designed so that the specified angular resolution are met at the maximum scan angle.

It is not only the array factor that determines the performance of the scanning array. It is clear from pattern multiplication that the element pattern will equally affect the total radiation

pattern of the array. It is therefore important to consider the element pattern when designing an array. Figure 6 shows the effect of the element pattern on the total radiation pattern.

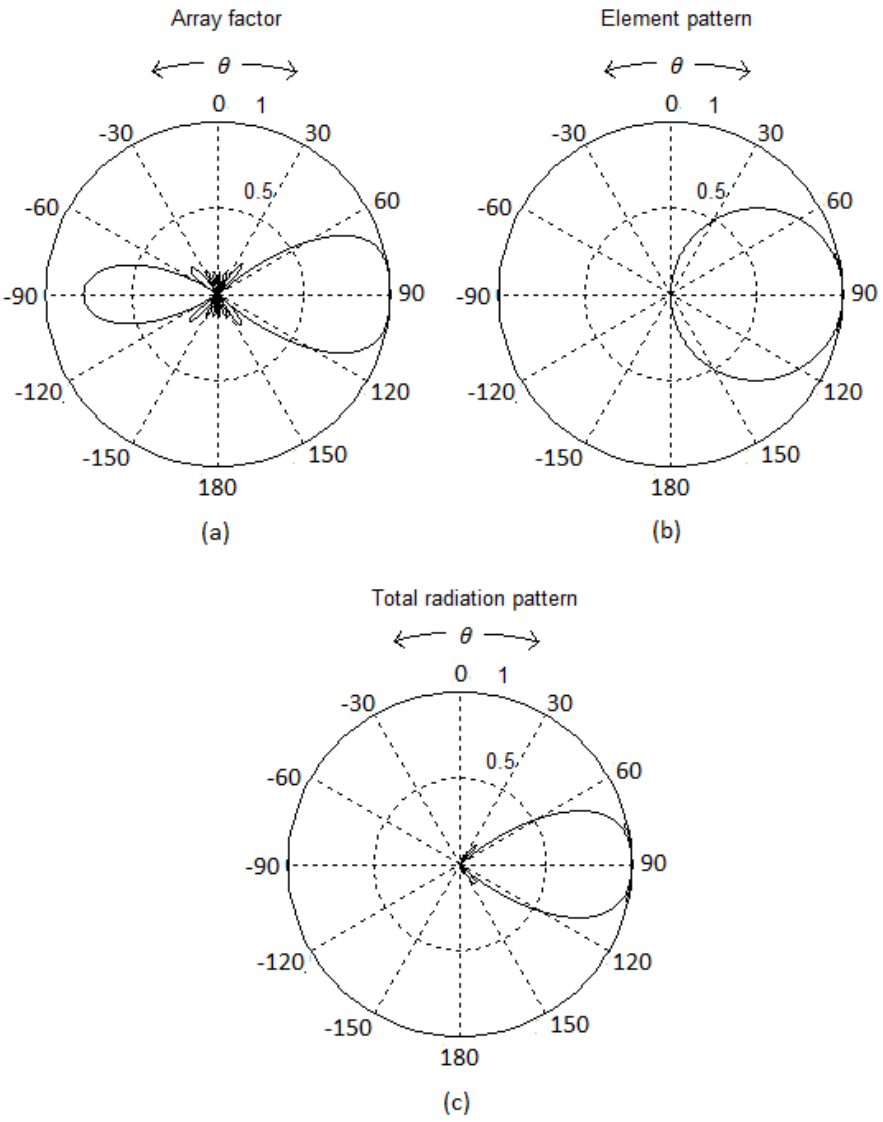

Figure 6: Example of pattern multiplication. (a) Array factor. (b) Element pattern. (c) Total radiation pattern

The element pattern will introduce scan loss. This occurs when the gain of the antenna element is not constant over the entire scan range. This leads to a main beam with different gain for different scan angles. Scan loss is given as [2, p. 13]

$$Scan\ loss\ at\ \theta_0 = 20\ log\left|\frac{G_{max}}{G(\theta_0, 0)}\right| \tag{2.22}$$

where G is the gain of the antenna element, G_{max} is the maximum gain, and θ_0 is a specific direction. An element often has the highest gain in the broadside direction and then the gain

decreases to the sides. If the gain decreases rapidly the main beam will be severely attenuated when scanned off broadside. If the main beam of the array factor was scanned towards 60° instead of 0° in Figure 6, it would be damped by the element pattern. So an optimal element pattern for scanning applications is constant over the entire scan range. This means that the major lobe of the array factor is affected equally over the entire scan range.

The scan loss property is not only negative. An element pattern with near constant gain over the entire scan range and then rapidly decreasing gain will not affect the major lobe but will decrease the side lobes and backwards radiation. This is seen in Figure 6 where the element pattern completely removes the backwards radiation.

2.1.1.3 Planar array

The planar array is a two dimensional structure, unlike the linear array which is one dimensional. This extra dimension gives the planar array several advantageous properties. The main beam can be steered in any direction, it has a more symmetrical pattern and lower side lobe levels [3, p. 349]. The planar array can have many different lattice structures. A general lattice structure is shown in Figure 7. Here d_x and d_y are the length and height of the unit cell, and γ is the unit cell angle. Together these parameters describe the lattice structure.

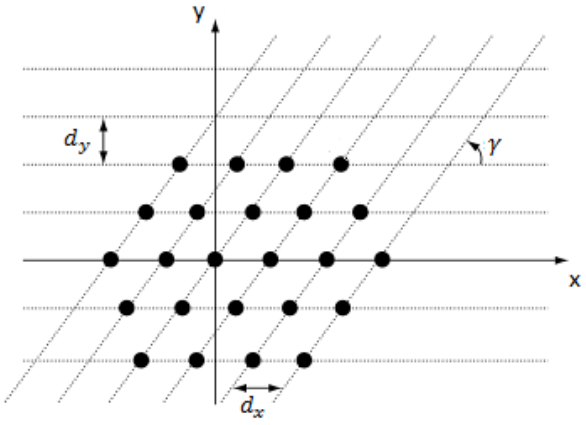

Figure 7: General lattice structure [2, p. 19].

A common lattice structure is the rectangular grid, in this case $\gamma = 90°$. This makes d_x and d_y the element spacing. Figure 8 shows the geometry of a rectangular array in the x-y plane. If identical antenna elements are used, then pattern multiplication will apply.

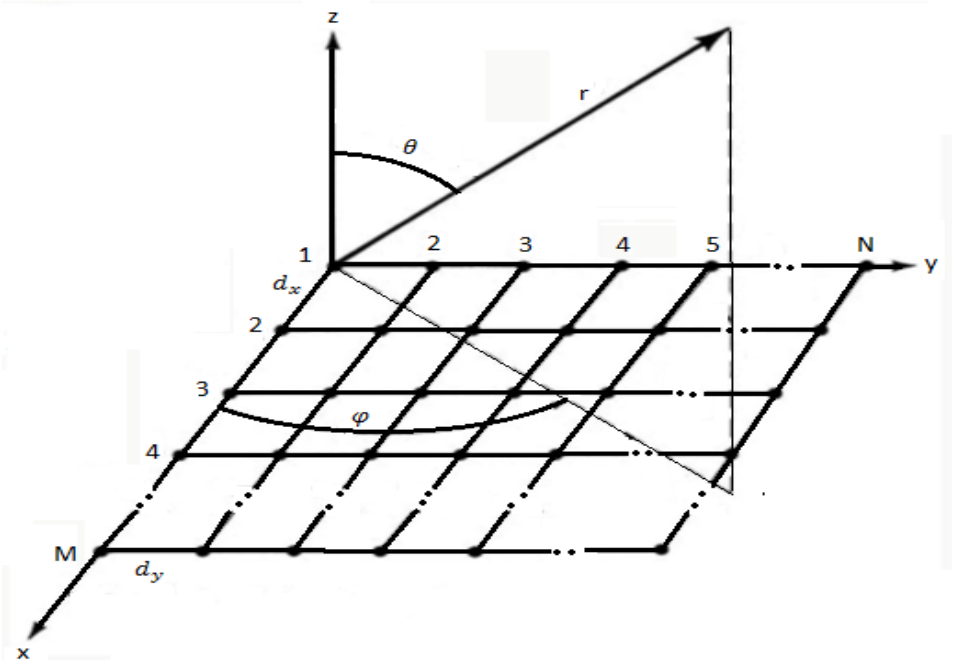

Figure 8: Rectangular array [3, p. 350]

The rectangular array can be seen as multiple linear arrays lined up besides each other. The array factor is therefore given as [3, p. 351]

$$AF_{rec} = \sum_{n=1}^{N} A_{1n} \left[\sum_{m=1}^{M} A_{m1}\, e^{j(m-1)(k_0 d_x \sin\theta \cos\varphi + \beta_x)} \right] e^{j(n-1)(k_0 d_y \sin\theta \sin\varphi + \beta_y)} \qquad (2.23)$$

Here A_{m1} and A_{1n} represents the amplitudes, and β_x and β_y is the phase difference between elements in x and y direction respectively. From equation (2.23) it can be seen that the array factor of a rectangular array is the product of the array factors of a linear array in x and y-direction.

$$AF_{rec} = AF_{lin,x}\, AF_{lin,y} \qquad (2.24)$$

Assuming uniform amplitude the normalized array factor can be written as [3, p. 351]

$$AF(\theta,\varphi) = \left\{ \frac{1}{M} \frac{sin\left(\frac{M}{2}\psi_x\right)}{sin\left(\frac{1}{2}\psi_x\right)} \right\} \left\{ \frac{1}{N} \frac{sin\left(\frac{N}{2}\psi_y\right)}{sin\left(\frac{1}{2}\psi_y\right)} \right\} \qquad (2.25)$$

where M is the number of elements in x-direction and N is the number of elements in y-direction.

$$\psi_x = k_0 d_x \, sin\theta \, cos\varphi + \beta_x$$
$$\psi_y = k_0 d_y \, sin\theta \, sin\varphi + \beta_y \tag{2.26}$$

The maxima of each factor of (2.25) are given as

$$(k_0 d_x \sin\theta \cos\varphi + \beta_x) = \pm 2m\pi \qquad m = 0, 1, 2, \ldots$$
$$\left(k_0 d_y \sin\theta \sin\varphi + \beta_y\right) = \pm 2n\pi \qquad \text{n} = 0, 1, 2, \ldots \tag{2.27}$$

As for the linear array the first maximum is the major lobe and the other maxima are grating lobes. To locate grating lobes the equations under can be used [3, pp. 352-353]

$$\varphi = tan^{-1}\left[\frac{\sin\theta_S \sin\varphi_S \pm n\lambda_0/d_y}{\sin\theta_S \cos\varphi_S \pm m\lambda_0/d_x}\right] \tag{2.28}$$

and

$$\theta = sin^{-1}\left[\frac{\sin\theta_S \cos\varphi_S \pm m\lambda_0/d_x}{\cos\varphi}\right]$$
$$= sin^{-1}\left[\frac{\sin\theta_S \sin\varphi_S \pm n\lambda_0/d_y}{\sin\varphi}\right] \tag{2.29}$$

For a grating lobe to exist both forms of (2.29) must give the same θ value. Since the array factor of a rectangular array is given by the product of array factors for linear arrays in x and y-direction, a relationship between equation (2.15) and equations (2.28) and (2.29) is expected. This is confirmed by applying equations (2.28) and (2.29) on a linear array in x-direction ($\varphi = 0°$, $\varphi_S = 0°$, m=1, and n=0). This results in

$$\theta = sin^{-1}[\sin\theta_S \pm \lambda_0/d_x] \tag{2.30}$$

which gives

$$d_x = \left|\frac{\lambda_0}{\sin\theta - \sin\theta_S}\right|. \tag{2.31}$$

This is the same equation as (2.15). The first grating lobes of a rectangular array will occur either at ($\theta = \pm 90°,\ \varphi = 0°$) or ($\theta = \pm 90°,\ \varphi = 90°$) depending on the scan angle. (2.15) can therefore be used to determine the maximum element spacing for rectangular arrays. To avoid grating lobes make $d_x < \lambda_0/2$ and $d_y < \lambda_0/2$ [3, p. 352].

As for a linear array the rectangular array can be phase-steered. The difference is that the main beam of the rectangular array can be pointed in any direction. Scanning is done by controlling the phase difference between elements in both x and y-direction. From (2.27) the β_x and β_y can be determined for a given scan angle (θ_S, φ_S)

$$\beta_x = -k_0 d_x \sin\theta_S \cos\varphi_S$$
$$\beta_y = -k_0 d_y \sin\theta_S \sin\varphi_S \quad (2.32)$$

The half-power beamwidth of a large rectangular array near broadside is approximately by [3, p. 357]

$$\Theta_h = \sqrt{\frac{1}{cos^2\theta_S \left[\Theta_{x0}^{-2}\, cos^2\varphi_S + \Theta_{y0}^{-2}\, sin^2\varphi_S\right]}}. \quad (2.33)$$

Here Θ_{x0} and Θ_{y0} are the half-power beamwidths of broadside linear arrays in x and y-direction respectively and can be determined using equation (2.21). For $\varphi_S = 0°$ equation (2.33) reduces to

$$\Theta_h = \frac{\Theta_{x0}}{\cos\theta_S} \quad (2.34)$$

The half-power beamwidth increases with a factor of $1/\cos\theta_S$ when scanned away from broadside. This result supports the beam broadening factor that was derived earlier in the chapter.

2.1.2 Floquet analysis

[2, pp. 61-154]

Another and relatively new method of analyzing arrays is the Floquet modal based approach. A brief overview of this approach is given here since HFSS[2] uses Floquet analysis to simulate arrays. It is also of interest to compare the results from the classical approach to results from the Floquet modal based approach. Floquet analysis has some advantages over the classical approach. These advantages are that it considers the effect of mutual coupling on both the input impedance of the antenna elements and the element pattern, and it models scan blindness. Even though the two approaches are very different it will be shown that results obtained by the classical approach is recreated by Floquet analysis.

Floquet analysis works only for infinite arrays. For this reason the accuracy of the method when analyzing a finite array can be doubted, but [2] shows that the performance of a finite array can be determined accurately using infinite array results. This is done by exciting only a finite amount of elements in the infinite array and leaving the other elements unexcited when analyzing the array. This gives a good approximation of a finite array. Another reason why accurate results can be expected is that central elements in a relatively large array experiences

[2] Software used in the design.

approximately the same mutual coupling as elements in an infinite array. This means that their input impedance and element radiation pattern are similar.

The basis of Floquet analysis for arrays is the Floquet series. It is similar to a Fourier series except for an additional periodicity in phase. A function with both periodic magnitude and phase but with different periodicities is given as [2, p. 65]

$$h(x) = \sum_{n=-\infty}^{\infty} f(x - nd)e^{-jn\beta}. \tag{2.35}$$

$f(x)$ is a complex function and β is a real constant. This function has a periodicity of d, and the phase of $h(x)$ decreases by β every interval $\Delta x = d$. Doing a Floquet series expansion on (2.35) gives [2, p. 66]

$$h(x) = \frac{2\pi}{d} \sum_{n=-\infty}^{\infty} \tilde{f}\left(\frac{2n\pi + \beta}{d}\right) e^{-\frac{j(2n\pi+\beta)x}{d}} \tag{2.36}$$

where $\tilde{f}(k_x)$ is the Fourier transform of $f(x)$, $k_x = 2n\pi + \beta/d$ is the spectral frequency. How these equations can be used to model an array is presented below.

Figure 9 shows a linear infinite array of y-directed uniform current sources, the current sources are surface currents so z=0. The current excitation function is given as [2, p. 70]

$$\vec{I} = \hat{y} \sum_{n=-\infty}^{\infty} f(x - nd)e^{-jn\beta} \tag{2.37}$$

where d is the element spacing and β is the phase difference between the elements. The current excitation function is more or less identical to equation (2.35), so a Floquet series expansion can be used to describe the electromagnetic fields produced by this array. When sources can be described by functions of the same form as equation (2.35) they are called Floquet sources.

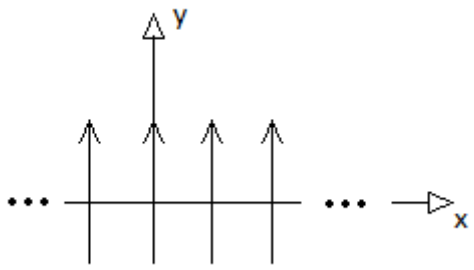

Figure 9: Linear infinite array

The electromagnetic field components produced by the current sources are given by [4, p. 601]

$$\vec{H} = \frac{1}{\mu}\nabla \times \vec{A}$$
$$\vec{E} = \frac{1}{j\omega\varepsilon}\nabla \times \vec{H} \tag{2.38}$$

ε and μ are permittivity and permeability, respectively. $\vec{A}$ is a vector potential and needs to be determined before the electric and magnetic fields can be found. The vector potential is determined by using the inhomogeneous Helmoltz equation [4, p. 339]

$$\nabla^2\vec{A} + k_0^2\vec{A} = -\mu\vec{J} \tag{2.39}$$

where $\vec{J}$ is the current density and k_0 is the free space wave number. Since the current sources are y-directed $\vec{A} = \hat{y}A_y$, equation (2.39) can then be written in scalar form as

$$\nabla^2 A_y + k_0^2 A_y = -\mu J_y. \tag{2.40}$$

The current sources lies on the surface and therefore J_y can be expressed by [2, p. 71]

$$J_y = \delta(z)\sum_{n=-\infty}^{\infty} f(x - nd)e^{-jn\beta} \tag{2.41}$$

$\delta(z)$ is the Dirac delta function and it ensures that the current density is zero for $z \neq 0$. Doing a Floquet series expansion on the right side of (2.41) and inserting into (2.40) gives

$$\nabla^2 A_y + k_0^2 A_y = -\delta(z)\frac{2\pi\mu}{d}\sum_{n=-\infty}^{\infty}\tilde{f}\left(\frac{2n\pi+\beta}{d}\right)e^{-\frac{j(2n\pi+\beta)x}{d}}. \tag{2.42}$$

A solution for A_y is given by [2, p. 72]

$$A_y = \frac{\pi\mu}{jd}\sum_{n=-\infty}^{\infty}\frac{\tilde{f}(k_{xn})}{k_{zn}}e^{-jk_{xn}x - jk_{zn}z} \qquad z > 0 \tag{2.43}$$

where

$$k_{xn} = \frac{2n\pi + \beta}{d}$$
$$k_{zn}^2 = k_0^2 - k_{xn}^2 \tag{2.44}$$

Using (2.38) the electric field is found to be [2, p. 71]

$$E_y = -\frac{\pi\omega\mu_0}{d}\sum_{n=-\infty}^{\infty}\frac{\tilde{f}(k_{xn})}{k_{zn}}e^{j\omega t - jk_{xn}x - jk_{zn}z} \qquad z > 0 \tag{2.45}$$

were the time factor $e^{j\omega t}$ is added. The exponential term in (2.45) is a Floquet mode. Comparing (2.45) with the equation below will help interpret the result.

$$E_x^+(z,t) = Re\left[E_0^+ e^{j\omega t - k_0 z}\right] \tag{2.46}$$

This equation represents a plane wave propagating in z-direction, it is polarized in x-direction and has an amplitude of E_0^+ [4, p. 356]. The similarities in the exponential terms of (2.45) and (2.46) leads to the conclusion that each Floquet mode represents a plane wave and that the total electric field E_y is the summation of all these plane waves. Each mode has its own propagation direction relative to the z-axis which is given by [2, p. 72]

$$\tan\theta_n = \frac{k_{xn}}{k_{zn}} = \frac{\frac{2n\pi + \beta}{d}}{\sqrt{k_0^2 - \left(\frac{2n\pi + \beta}{d}\right)^2}} \tag{2.47}$$

This equation can be simplified to (see Appendix E)

$$\sin\theta_n = \frac{-\beta - 2\,n\,\pi}{k_0 d} \tag{2.48}$$

This is the same equation as (2.12), which gives the direction of every maxima of (2.9). This means that the Floquet modes propagates in the same direction as the maxima of (2.35). The n=0 Floquet mode is the main beam and the other modes represent grating lobes. For a

Floquet mode to become a propagating grating lobe k_{zn} has to be real, if not it is a evanescent Floquet mode and does not propagate. For k_{zn} to be real

$$k_0 \geq \left|\frac{2n\pi + \beta}{d}\right| \tag{2.49}$$

This equation can be used to find the maximum element spacing of the array to avoid grating lobes. From equation (2.48) the phase difference β for a given scan angle θ_S can be determined, this is then inserted into equation (2.49), which gives

$$k_0 < \left|\frac{2n\pi - k_0\, a \sin\theta_S}{d}\right| \tag{2.50}$$

Solving with respect to d gives

$$d < \left|\frac{\lambda_0}{1 + \sin\theta_S}\right| \tag{2.51}$$

where $k_0 = 2\pi/\lambda_0$. This equation is the same as (2.15). The results obtained in (2.48) and (2.51) shows that both approaches produces same results.

2.1.2.1 Scan blindness

Scan blindness occurs when the reflection coefficient approaches unity for a given scan angle. This means that the array reflects all the incoming energy, and will therefore not radiate. For patch array scan blindness is mainly caused by surface waves [3, p. 866]. Scan blindness is detrimental to the scan performance of the array and needs to be accounted for. One advantage of Floquet analysis is that scan blindness can be analyzed.

In Floquet analysis scan blindness occurs when the propagation constant of a guided mode coincides with that of a Floquet mode. The modes will couple strongly which leads to a resonance and all the energy will then be reflected back into the circuit [2, p. 79]. For a patch array the guided mode will be surface waves excited by each patch.

2.1.3 Mutual coupling

Mutual coupling is an important phenomenon and needs to be taken into account when designing arrays. When antenna elements are put in proximity of each other, like in an array, their fields will couple together and change the antenna element properties. Mutual coupling will affect the input impedance of the elements and the elements radiation patterns [3, p. 468]. Parameters controlling the level of mutual coupling are; the element spacing, the relative placement and the radiation pattern of the elements [3, p. 478].

To explain the basic mechanisms of mutual coupling a simple example is presented. Two antennas are placed in the vicinity of each other. Only one antenna is excited and therefore radiates. Some of the energy will reach the second antenna and excite a current. The second antenna will then start to radiate, and some of the energy will reach the first antenna. This will alter the current distribution on the first antenna and therefore alter its input impedance. In summary, an antenna placed in vicinity of another object will experience a change in the current distribution which leads to a change in input impedance.

In an array the mutual coupling can be caused by several types of fields. For patch arrays the mutual coupling is mainly caused by; space waves which has a radial variation of $1/r$, higher order waves which has a radial variation of $1/r^2$, and surface waves with a radial variation of $1/r^{1/2}$. Because of different radial variation terms, each field will dominate the mutual coupling at different separations. Space waves and higher order waves will dominate at small separations while the surface waves will dominate at larger separations [3, pp. 857-858].

In patch antennas a large part of the mutual coupling is caused by surface waves. They travel along interfaces between media with different dielectric constants.

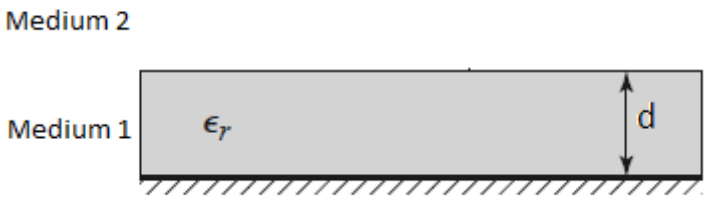

Figure 10: Grounded dielectric slab

When moving away from the interface between two media, the surface waves decay exponentially. Both TM[3] and TE[4] modes can exist. The TM_0 mode is the fundamental mode and has zero cut-off frequency. The cut-off frequency of a TM_n mode traveling on a grounded dielectric slab is given by [5, p. 137]

$$f_c = \frac{nc}{2d\sqrt{\epsilon_r - 1}}, \quad n = 0,1,2,3 \ldots\ldots \tag{2.52}$$

where d is the height of the dielectric slab, ϵ_r is the dielectric constant and c is the velocity of light in vacuum. From this equation one can see that to minimize the number of TM modes excited one has to make the dielectric layer thin and keep the dielectric constant low. The same is true for TE modes.

[3] In a TM mode the magnetic field components are transverse to the propagation direction
[4] In a TE mode the electric field components are transverse to the propagation direction

In rectangular patch arrays the level of coupling between elements is dependent on the relative placement of the elements. The reason for this is that the dominant surface wave mode is the TM_0 and that mode couples more strongly in the E-plane direction [3, p. 858].

The input impedance of an array will change as a function of scan angle because the mutual coupling between the elements change for different scan angles.

2.2 Tools

2.2.1 HFSS

HFSS is a 3D full wave electromagnetic field simulator. It uses the finite element method together with adaptive meshing to solve the wave equations. If a 3D model has been made HFSS sets up the mesh automatically. HFSS computes S-parameters, it can calculate and plot both the near and far field radiation and compute important antenna parameters such as gain and radiation efficiency.

To verify the accuracy of HFSS an antenna has been simulated in both HFSS and a similar software package called CST. The results are shown in Figure 11.

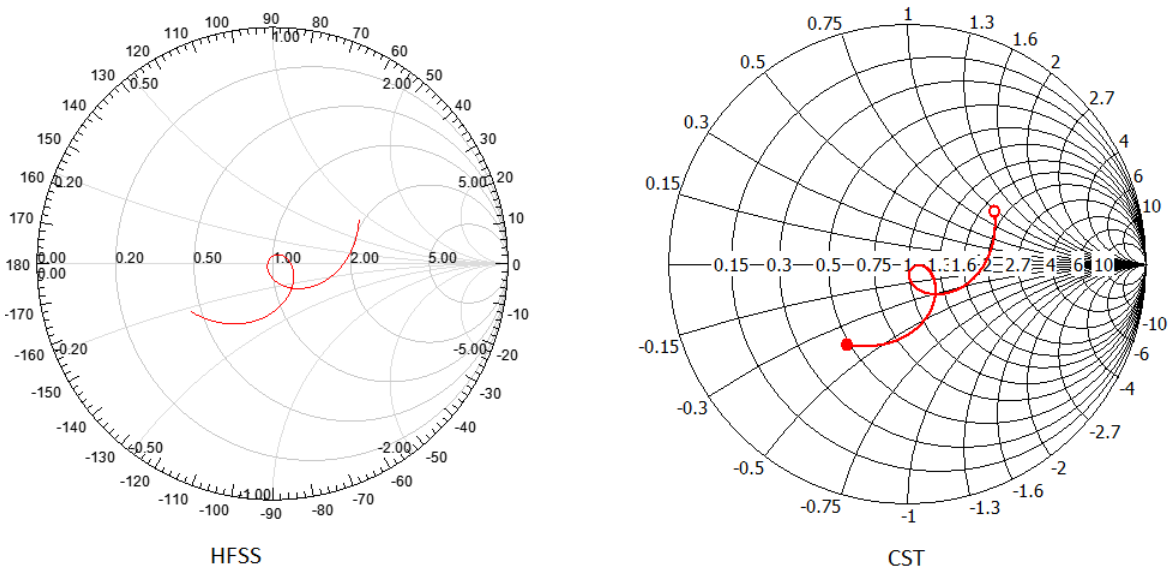

Figure 11: Comparison of HFSS and CST

The results are relatively similar, which is a good indication that HFSS has the required accuracy.

2.2.1.1 Array simulation

HFSS has three standard methods for modeling and simulating arrays; the Finite Array method, the Finite Array domain decomposition (DDM), and the unit-cell with Floquet ports.

The first method, the Finite Array method is the straight forward approach to model and simulate an array. Here the entire array is modeled in HFSS with each antenna element having its own excitation. This is the most accurate method, but it demands large amounts of memory and it is very time consuming. It is therefore not an efficient method to use when tuning an array.

The second method, the Finite Array DDM is an accurate method including mutual coupling between elements and edge effects[5]. This method is almost as accurate as the first method but demands less memory and are faster. This method uses two techniques to decrease solving time and memory use. The first technique is the domain decomposition (DDM). It divides the array into smaller parts and solves each part on different computers. This reduces the simulation time. The second technique is the use of a unit cell. The simulator will use the mesh obtained when simulating the unit cell on all the antenna elements in the array. This saves time and memory since the meshing procedure is both time consuming and memory demanding. Even though this method is far more efficient than the first method it is still too slow for tuning an array.

The third method uses the unit cell and Floquet ports. The Floquet port enables HFSS to do a Floquet analysis as described in the theory chapter. This means that the array is approximated as an infinite array and edge effects are therefore ignored. However it does take into account mutual coupling between elements. This method will give accurate results for antenna elements in the middle of the array and the larger the array is the more accurate the method becomes. This is due to the infinite array approximation. The solving time is highly reduced and much less memory is needed, since only the unit cell is simulated. This method is therefore the best one for tuning an array.

[5] Antenna elements on the edge will have different properties from elements placed in the middle.

3 The antenna element

The design of the antenna element was done in the specialization project and is described in detail in [1]. A short summary of the design is presented here. Measured results are presented and compared to the simulated results. It is recommended to read Appendix A.1 before reading this chapter if one is not familiar with patch antennas.

3.1 Design

The design was based on the basic patch antenna. This was done for several reasons; it is a well known technology widely used in many applications, it is relatively cheap and easy to manufacture, it also enables the mounting of electronic components on the back side, but most important the patch antenna enables design of compact and lightweight arrays.

Four different methods for feeding the patch antenna were considered; the microstrip line feed, probe feed, aperture-coupled feed, and proximity feed. The aperture-coupled feed was chosen due to a better fit for this application. It gives low cross polarization, low spurious feed radiation and it is beneficial that the antenna can be fed from the backside when implementing an array.

The required frequency band of the antenna is 8-8.50 GHz with a center frequency of 8.25 GHz. For a patch antenna the biggest limitation on the bandwidth is the input impedance. A low reflection coefficient over the frequency band is necessary because of the large amount of power delivered by the power amplifier (PA). Three techniques for increasing the bandwidth and improving the reflection coefficient was considered; resonant aperture, aperture-coupled stacked patch (ACSP) and resonant aperture stacked patch (ASP). The ACSP was chosen because it has lower backwards radiation than the other two alternatives considered. Low backwards radiation is important for this application because of the electronic components on the backside of the antenna, and more power directed forward gives a longer radar range.

The materials used are important both for the electronic and thermal properties of the antenna. A Hi-Lo dielectric constant configuration has been used [6]. The lower patch is etched on a substrate with a high dielectric constant and the upper patch is etched on a substrate with lower dielectric constant. This reduces the surface wave loss, decrease cross-polarization, and further increase the bandwidth of the antenna.

For the lower layers of the antenna the Rogers XT/duroid 6035HTC was chosen. This substrate has a low loss tangent and high thermal conductivity minimizing the temperature rise in the antenna. A foam type substrate was chosen for the upper layer to obtain a low dielectric constant. The material used is Rohacell 71 IG. The upper patch is etched on a thin layer of Rogers RT/duroid 5880 which is placed on top of the foam substrate. This is done since etching of copper is not possible on the Rohacell 71 IG. The properties of the materials used are listed in the Table 1

Table 1: Properties of Rogers XT/duroid 6035 HTC, Rogers RT/duroid 5880 and Rohacell 71 IG

Parameter	6035HTC	5880	71 IG	Units
Dielectric constant	3.6	2.2	1.09	
Loss tangent	0.0013	0.0009	0.0034	
Thermal conductivity	1.44	0.20		W/m/K
Thermal coefficient of ϵ_r	-66	-125		Ppm/C

The two patches were made rectangular to reduce cross polarization. The feed line was designed to have a characteristic impedance of 50 Ω. For increased level of coupling and reduced backwards radiation a H-shape slot was used.

A ground shield was added behind the slot to reduce the backward radiation and to increase the area where the electronic components can be placed. The slot is surrounded by tightly spaced vias which connects the two ground planes. The vias form a cage reducing the excitation of waves that can travel through the substrate.

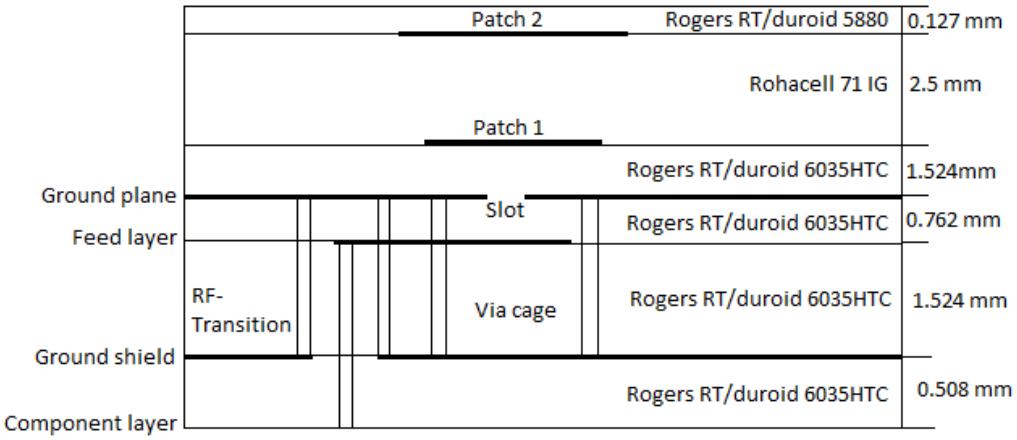

Figure 12: Side view of the ACSP antenna with ground shield, via cage and RF-transition

Since the feed and component layers are separated by the ground shield a RF-transition has been made. This structure is designed to transfer the RF signal from the component layer to the feed layer without any leakage. It consists of a center via that connects the two layers through a hole in the ground shield. The center via is surrounded by other vias. They work as the outer conductor of a coaxial cable and holds the fields inside the structure so that leakage is minimized.

No mathematical model of this antenna was found but guidelines [7] [8] and design examples [9] [10] exist. These guidelines and design examples were used together with HFSS to design the antenna in a step by step process. The slot size, patch sizes, and substrate thicknesses were adjusted to achieve the wanted properties.

3.2 Production

The antenna shown in Figure 12 is a complicated construction. It consists of six copper layers, both blind[6] and buried[7] vias and three different substrate types. This makes the production expensive and technically difficult, and therefore, additional steps was done to make the antenna ready for production. The final stack up can be seen in Figure 13.

Because of the foam substrate the antenna had to be produced in three parts and assembled using plastic screws[8]. The number of via types was reduced by redesigning the RF-transition as can be seen in Figure 13. A surface mounted SMA connector was placed on the component layer to enable antenna measurements.

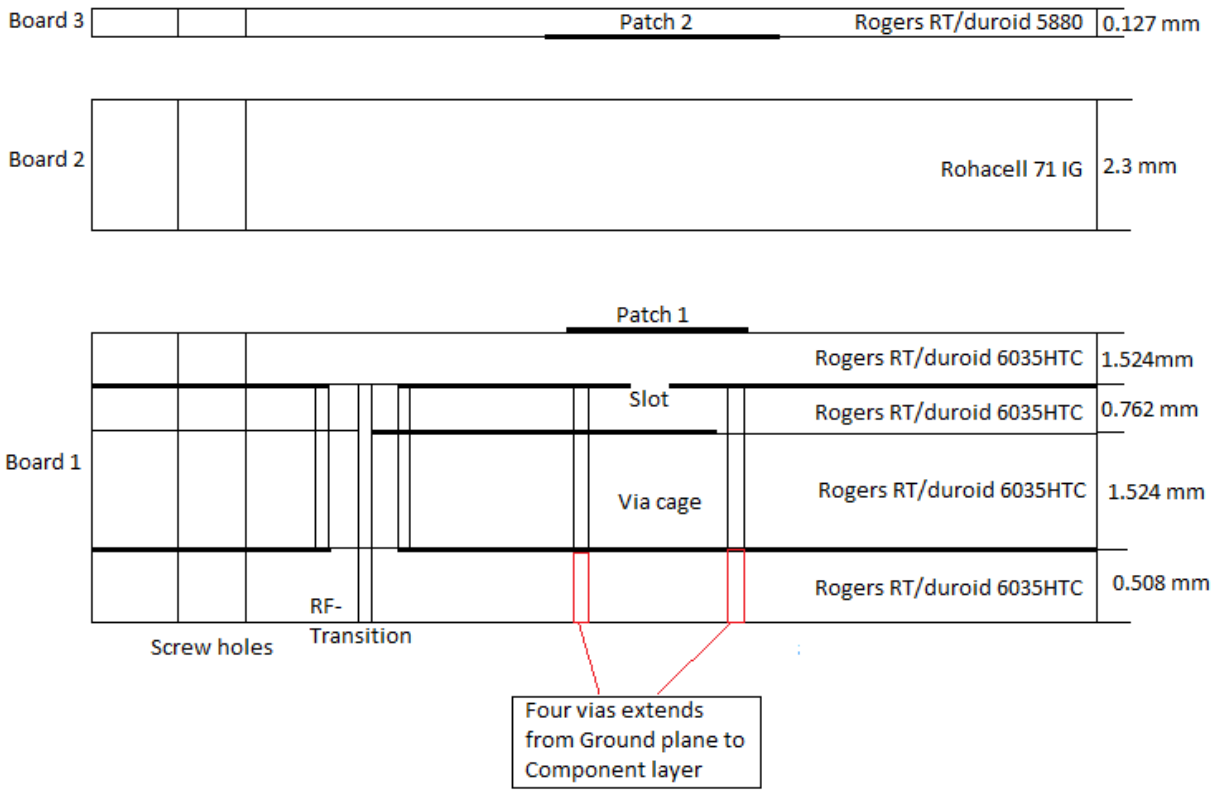

Figure 13: Side view of the production ready antenna

[6] A via that starts at a outer layer and ends in a middle layer.
[7] A via that starts and ends in middle layers.
[8] No bonding material was found that could be used without deforming the foam substrate.

3.3 Simulation and measured results

For simulation or measurement of the antenna input impedance a reference point is needed. The reference point used when tuning the antenna in HFSS is shown in Figure 14 (point A). It was placed at this position to ensure a good match for the power amplifier, since the PA was to be placed in this area. The simulated results using A as the reference point are shown in Figure 15. Measuring the input impedance directly at this point is difficult so a SMA connector was added. To ensure good compliance between measured results and simulated results it was necessary to use the same reference point for both simulation and measurements. Two alternatives could be used to achieve this; a SMA connector could be included in the model, or the connector could be calibrated away during measurements, this would move the reference point from B to A. The first alternative was chosen since the latter alternative are less accurate owing to the abrupt transition from the coax connector to the microstrip line.

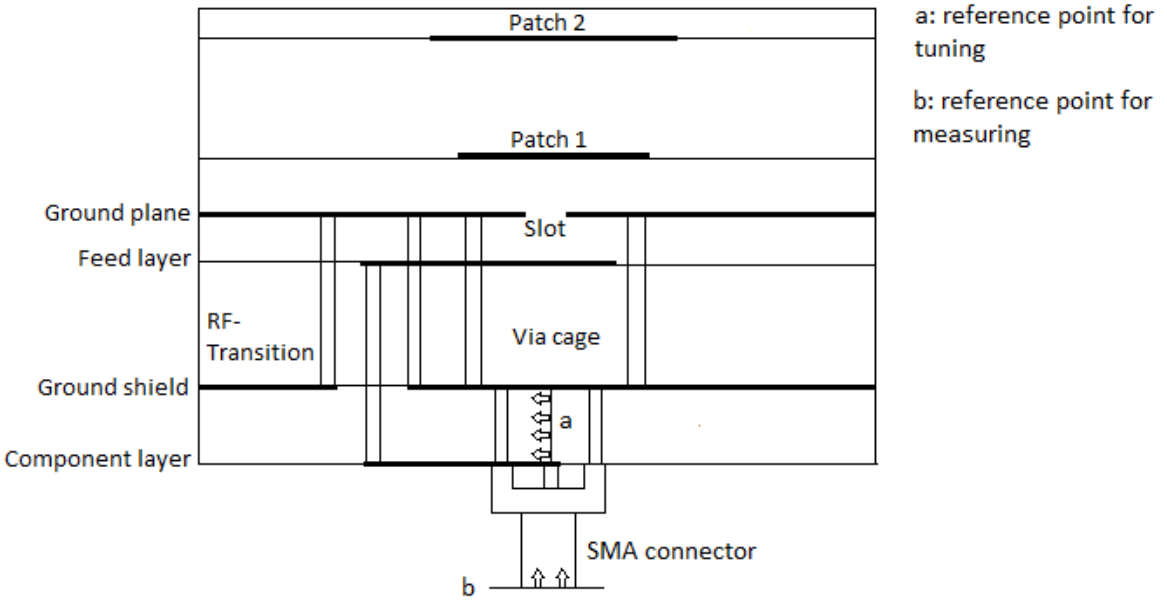

Figure 14: Side view of antenna with reference points.

A SMA connector was modeled in HFSS and new simulations were conducted with the reference point moved to point B. The results are shown in Figure 16. As expected the input impedance of the antenna has changed after moving the reference point. The two main reasons for the change are the adding of the transmission line and the transition from coax to microstrip line. When adding length to a transmission line the change in input impedance can be predicted by using the following equation [5, p. 59].

$$Z_{in} = Z_0 \frac{Z_L + jZ_0 \tan \beta l}{Z_0 + jZ_L \tan \beta l} \tag{3.1}$$

Here Z_0 is the characteristic impedance of the transmission line, and Z_L is the load impedance, which in this case is the input impedance of the antenna at reference point A. l is the additional length of transmission line and β is the phase constant. In this case equation (3.1) would not give an accurate prediction since the transition from coax to microstrip line also affects the result.

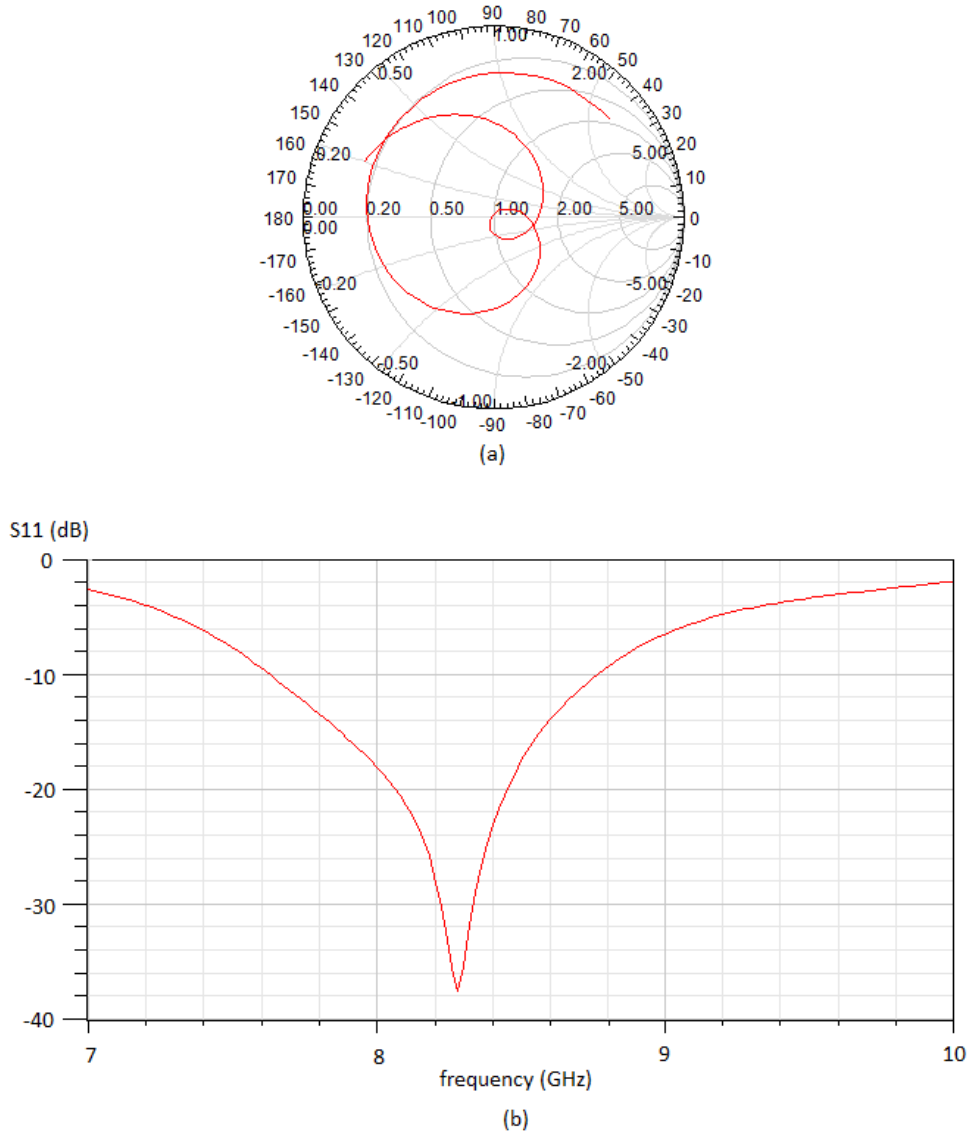

Figure 15: The simulated reflection coefficient (S11) for reference point A plotted in a Smith chart (a) and in dB as a function of frequency (b).

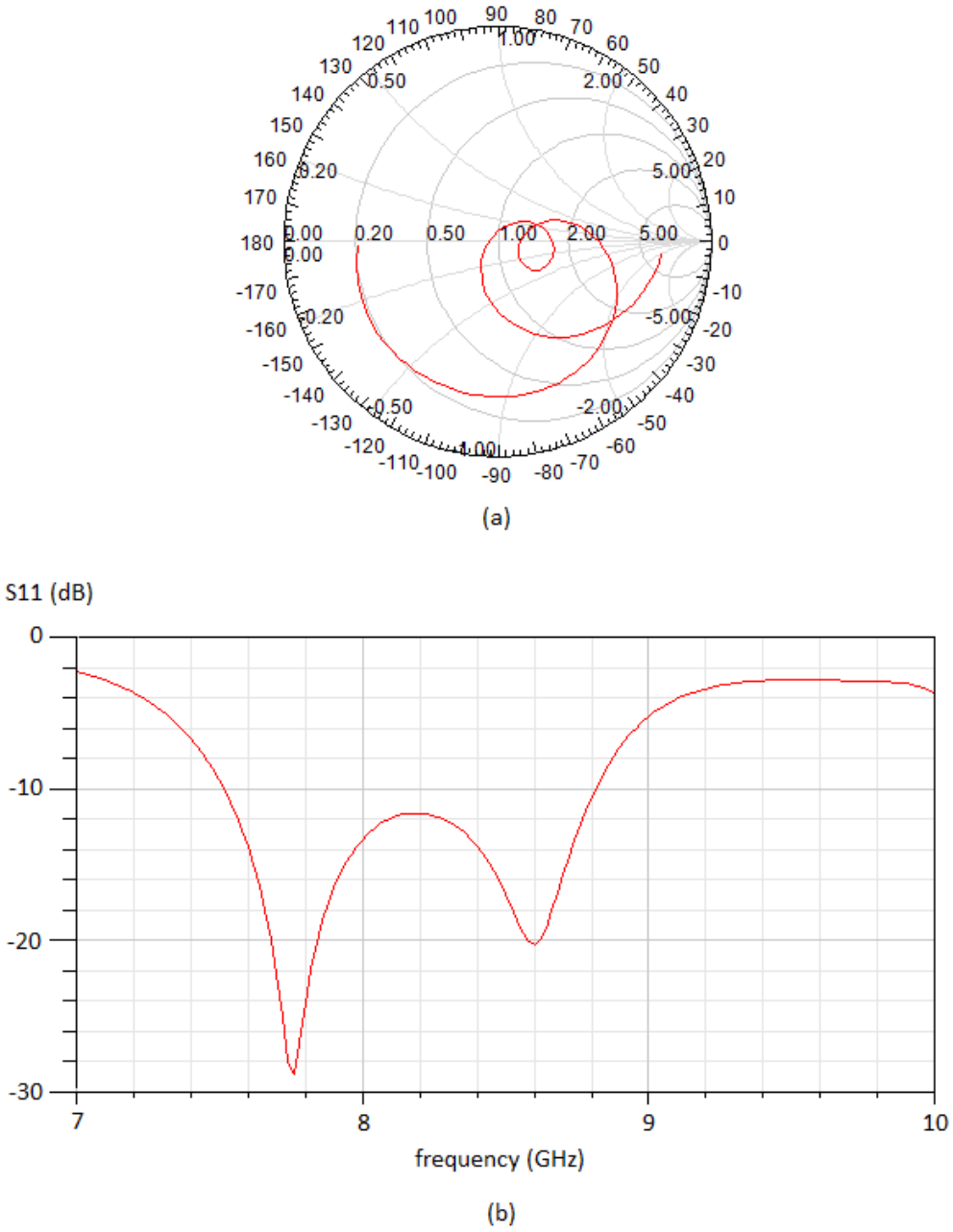

Figure 16: The simulated reflection coefficient (S11) for reference point B plotted in a Smith chart (a) and in dB as a function of frequency (b).

A network analyzer was used to measure the input impedance of the antenna. After calibration the reference point for the measurement was located at point B. So identical reference points for measurement and simulation were obtained and therefore similar results were expected. The measurement results are shown in Figure 17.

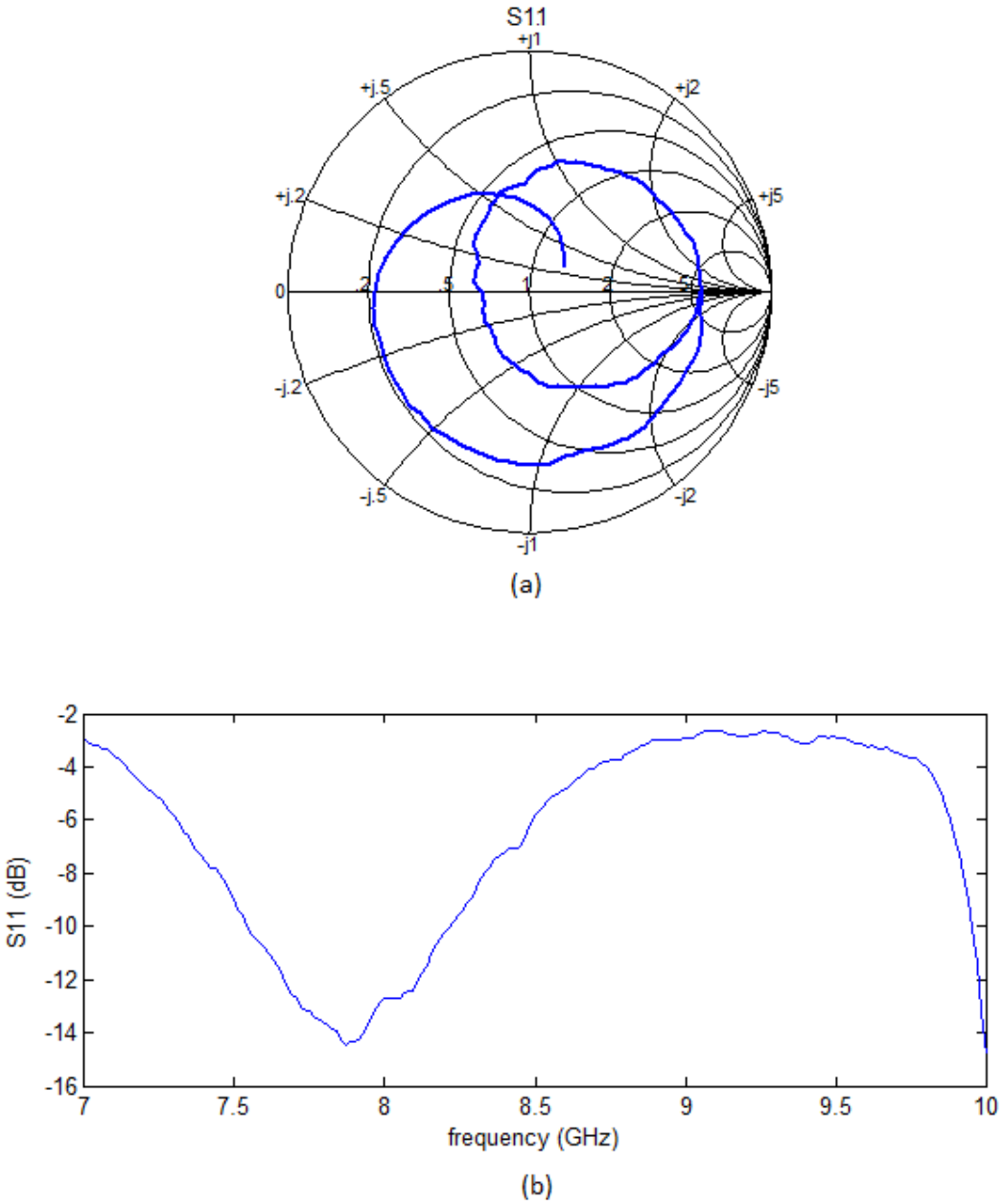

Figure 17: The measured reflection coefficient (S11) for reference point A plotted in a Smith chart (a) and in dB as a function of frequency (b).

To measure the radiation pattern the new antenna hall at NTNU was used. The antenna was placed in an anechoic chamber across from a reference antenna. Then the radiation pattern was measured by rotating the antenna and exciting the reference antenna. Simulated and measured results are presented in Figure 18 and Figure 19. A description of the measurements and more results can be found in Appendix B.

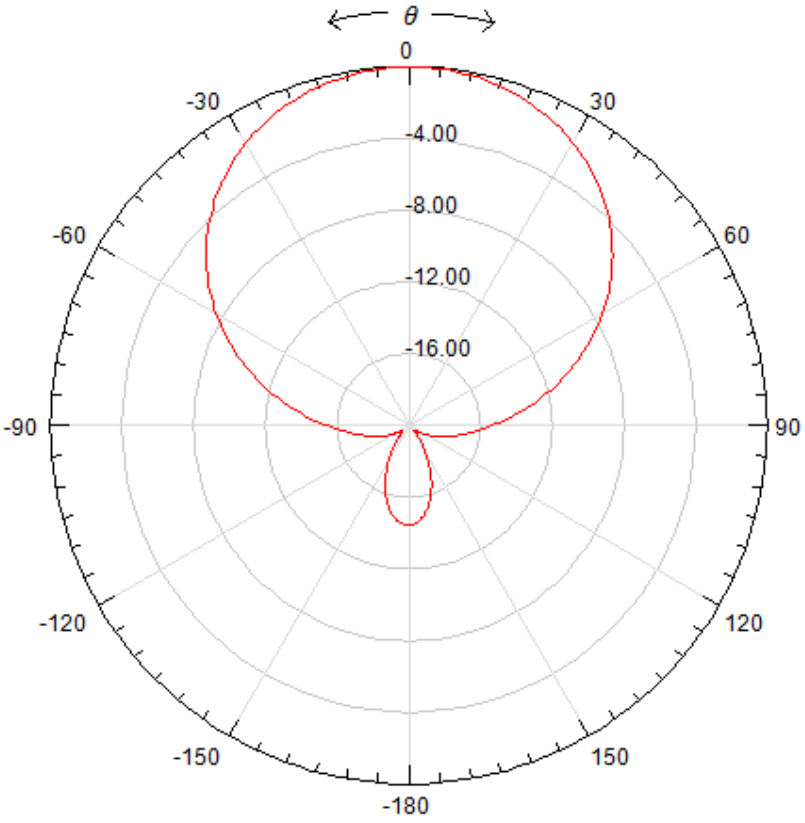

Figure 18: Simulated radiation pattern in normalized dB measured at 8.25 GHz in the H-plane (ϕ=90).

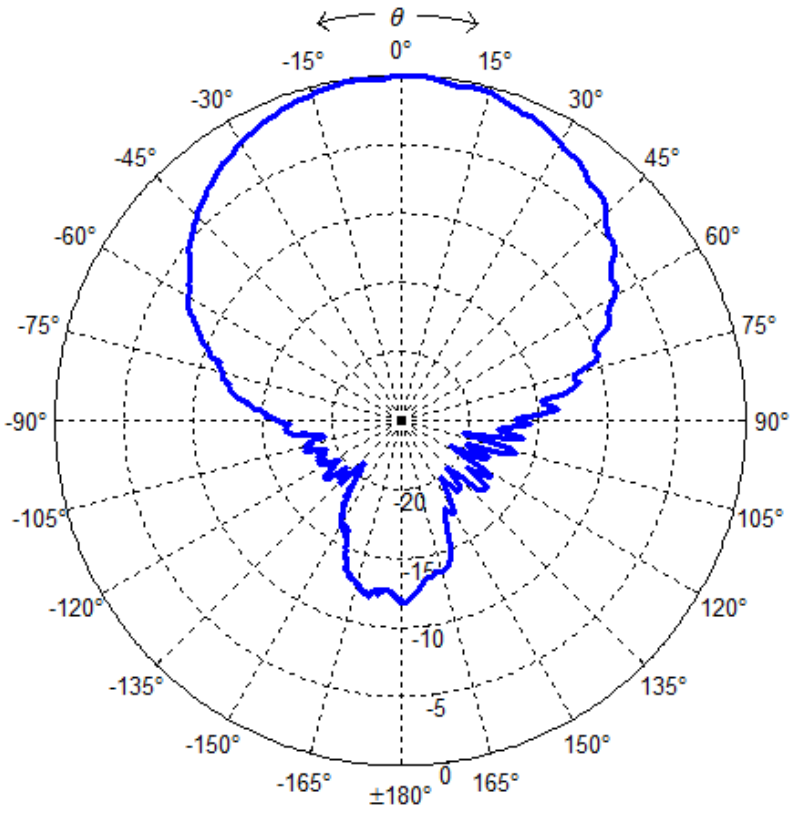

Figure 19: Measured radiation pattern in normalized dB measured at 8.25 GHz in the H-plane (ϕ=90).

3.4 Analysis of the results

3.4.1 Input impedance

As seen from the results presented in the section above (Figure 16 and Figure 17) there were large deviations between the measured and simulated input impedance. This presented a severe problem that had to be solved. One important reason for producing the antenna elements was to test the accuracy of HFSS. It is difficult to tune the array using HFSS if not better compliance between simulation and measured results can be achieved. Several possible reasons for these deviations were investigated.

- Inaccuracies in the simulator.
- Bad simulation setup.
- Measurement errors
- Production errors.
- Bad modeling of the SMA connector.

HFSS is a commercial software used by many antenna developers. It is therefore unlikely that inaccuracies in the simulator causes such large deviations as experienced in this case. Also results from [9] show that HFSS can produce simulation results giving good compliance with measured results.

To eliminate the possibility of a bad simulation setup an expert from ANSYS[9] was consulted. The simulation setup was inspected and improved. The improvements led only to small changes in the simulation results. It was therefore concluded that the simulation setup was not the reason for the large deviations.

Five antennas were produced and measurements of their input impedance were performed. Only small deviations between the antenna input impedances were observed. To decrease the probability of measurement errors two different network analyzers were used and all the measurements were performed three times on different occasions. The difference in results between the two network analyzers were negligible. It was also negligible differences between the three measurements. Since no large deviations occurred between the different measurements it was concluded that it is unlikely that measurement errors were the reason for the large deviations.

The next error source investigated was production errors. This was the most likely cause of error because of the complicated structure of the antenna. In this report production errors are used as a collective term for all error sources that causes differences between the manufactured antenna and the antenna model[10]. Production errors occur during the manufacturing process and can for example be differences in dimensions owing to process variations, it can be caused by use of wrong materials, or it can be due to incorrect thickness

[9] The company that makes HFSS.
[10] The simulated antenna.

of a substrate layer. These differences will of course lead to deviations between measured and simulated results.

Process variations is random variations in the process that every fabrication process suffers from. It will lead to differences between the manufactured antenna and the simulated antenna, but most importantly it will lead to differences between each antenna element. When measuring the input impedance of each antenna only small differences in results were observed. This is a strong indication that the process variations are small and therefore not the reason for the large deviations between measured and simulated results.

In cooperation with the manufacturer several errors were discovered. First a different bonding material than ordered was used. The bonding material had a different dielectric constant, but because the bonding material is thin only small changes in the input impedance were expected. Simulations confirmed this. The gerber files[11] had been converted from millimeters to inches, introducing small errors. Simulations showed that these errors were too small to affect the results noticeably.

To verify the antenna dimensions a digital caliper was used for measurements of the antenna dimensions. The results are listed in Table 2.

Table 2: Measured antenna dimensions and corresponding dimensions of the antenna model.

	Antenna 2	Antenna 3	Antenna 4	Antenna 5	Antenna model
Total thickness (mm)	7.12	7.10	7.10	7.10	7.03
Thickness of board 1(mm)	-	4.58	4.58	4.58	5.6
Thickness of board 2 (mm)	-	2.42	2.43	2.42	2.3
Patch 1 (mm)	-	10.5x8	10.48x8	10.49x7.97	10.5x8
Patch 2 (mm)	-	13.23x11.5	13.33x11.48	13.23x11.5	13.3x11.5

The measurements showed that board 2, which is the foam layer, was thicker for the manufactured antennas than for the antenna model. The thickness of the foam layer determines the level of coupling between the two patches and are therefore a crucial parameter. A difference of 0.1 mm would lead to observable change in input impedance. Simulations done with a foam thickness of 2.4 mm confirmed this. Simulations showed also that the 0.1 mm difference in foam thickness was not solely responsible for the deviations. The measured dimensions of both patch 1 and patch 2 corresponded well with the antenna model.

Board 3, which is the top layer of the antenna, has a thickness of 0.127 mm. The layer was chosen to be thin to minimize the effect on the antennas properties. During the design of the antenna element the mechanical properties of the top layer were not considered. This oversight turned out to be a crucial mistake. The thin top layer was not rigid and a large bulge

[11] Industry standard file that are used in producing PCBs

was formed on the antenna when it was mounted. This increased the distance between the patches and therefore decreased the level of coupling between the patches which in turn lead to changes in the input impedance.

This error was detected early and tried to be solved by adding a foam layer on top to press the bulge down. The idea was to use a material with a low dielectric constant, in order to not affect the properties of the antenna. It was assumed that the foam layer was so rigid that the bulge was removed. New measurements did not show any large improvements, and it was concluded that the bulge did not cause the deviations.

To isolate the error source the input impedance of only board 1 was measured. Doing this would determine if the error source was located in the upper parts or the lower parts of the antenna. The measured and simulated input impedance of board 1 are shown in Figure 20 and Figure 21.

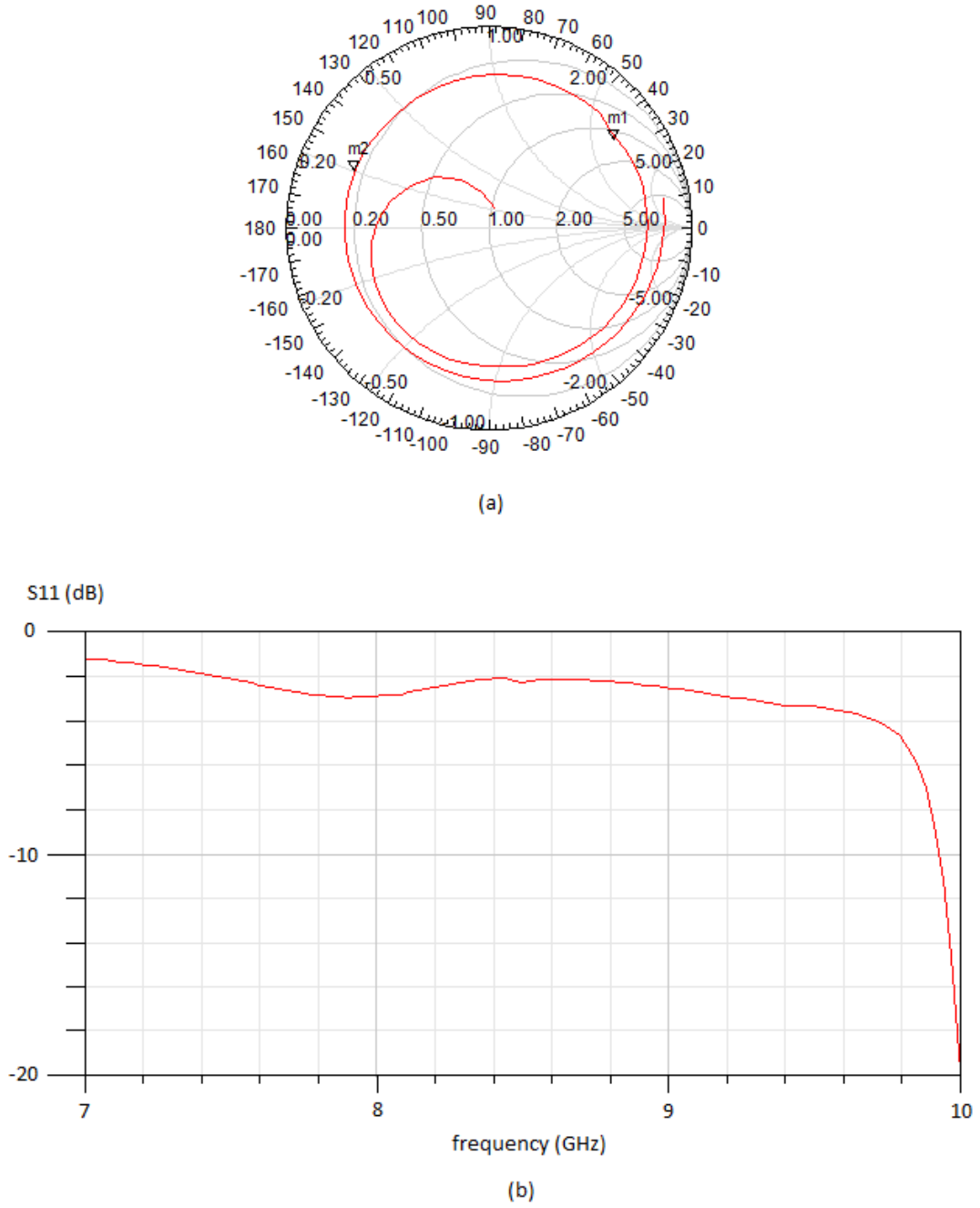

(a)

(b)

Figure 20: The simulated reflection coefficient (S11) of board 1 plotted in a Smith chart (a) and in dB as a function of frequency (b).

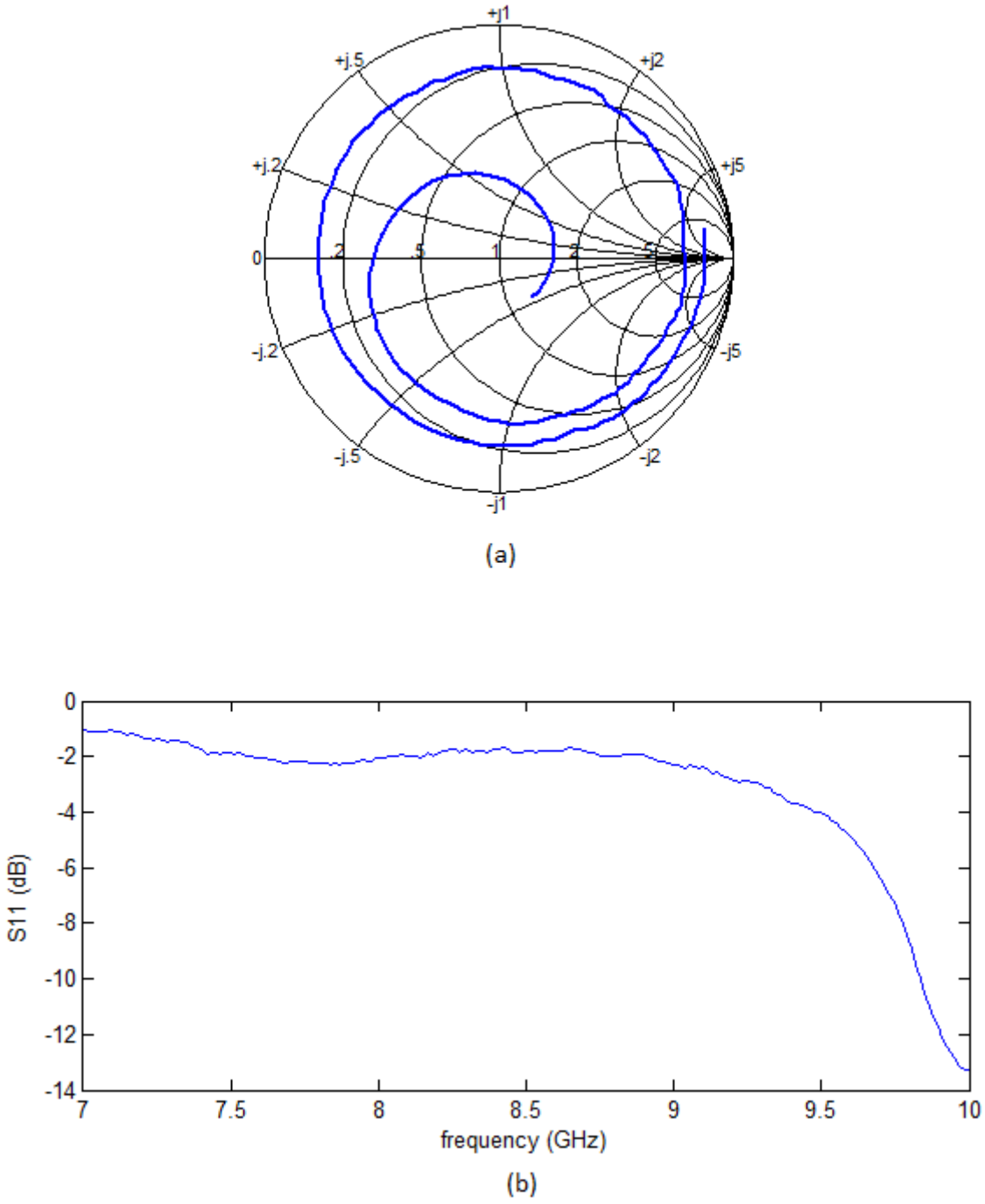

Figure 21: The measured reflection coefficient (S11) of board 1 plotted in a Smith chart (a) and in dB as a function of frequency (b).

Comparing Figure 20 and Figure 21 it is seen that the simulated input impedance and measured input impedance are quite similar. It was therefore concluded that the error source most likely was located in one of the two upper boards. This significantly decreased the number of possible error sources. The remaining error sources were either a different dielectric constant of the foam substrate or a wrong distance between the patches.

Simulations with different dielectric constants were conducted but no results matched the measured results. This alternative was therefore eliminated as a possible error source. Then simulations with different distances between the patches were done and results similar to the measured result were observed. One of these results is plotted in Figure 22.

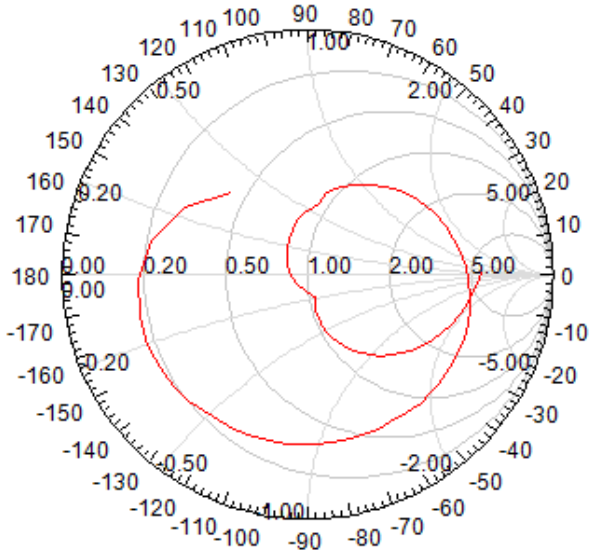

(a)

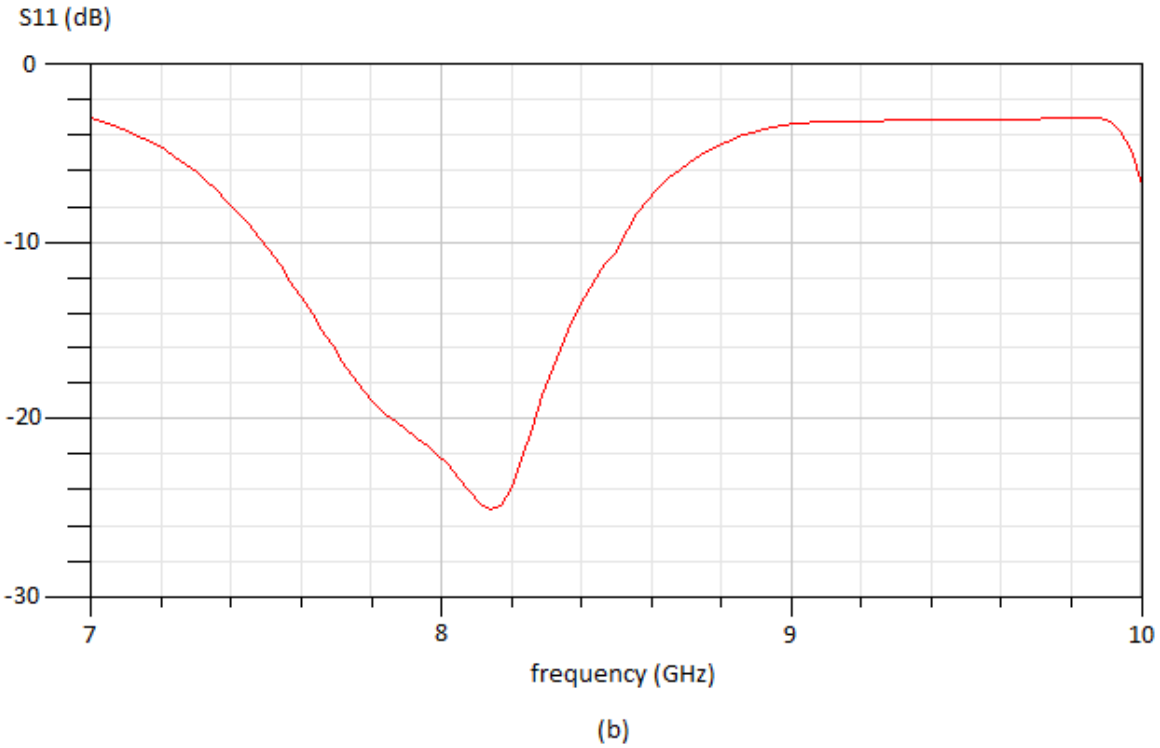

(b)

Figure 22: Simulated reflection coefficient of the antenna element with a foam thickness of 3 mm plotted in a Smith chart (a), and in dB as a function of frequency (b).

To obtain the results plotted in Figure 22 a distance between the patches of 3 mm was used. This is an error of 0.7 mm. Comparing the simulated results in Figure 22 with the measured results in Figure 17 similarities can clearly be seen. This was a strong indication that the deviations were caused by the wrong distance between the patches. The assumption of a foam layer rigid enough to remove the bulge was wrong and unnecessary time was spent in searching for another error.

A new top layer was designed using the same type of substrate (Rogers RT/duroid 5880) with a thickness of 1.575 mm. This thickness ensured that the substrate was rigid. The thick substrate altered the input impedance of the antenna, and the dimensions of patch 2 were therefore used to tune the input impedance in order to obtain a low reflection coefficient. Simulated and measured results of this antenna are presented in chapter 5.

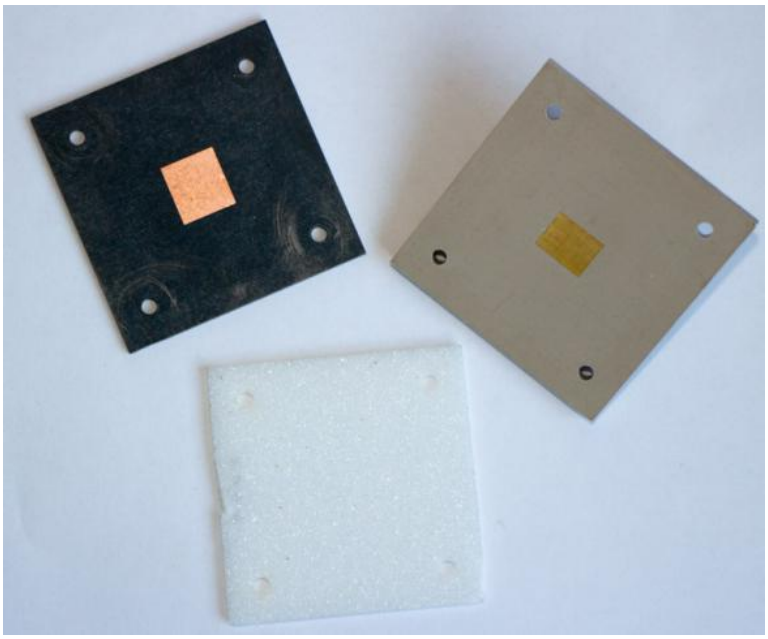

(a)

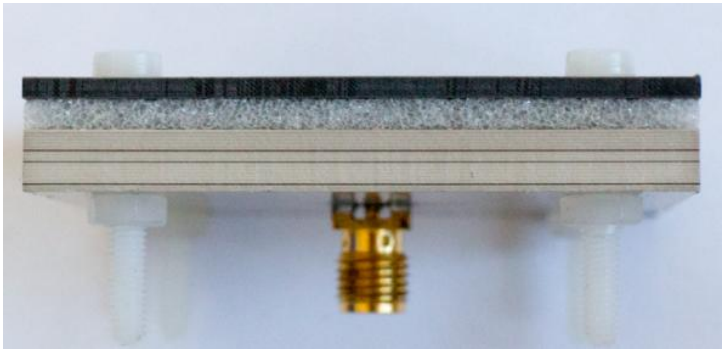

(b)

Figure 23: (a) A view of the three boards. (b) Side view of the modified antenna element.

3.4.2 Radiation pattern

Figure 18 and Figure 19 shows the simulated and measured radiation pattern of the antenna element. Comparing the shape of these plots it is seen that good compliance between measured and simulated results have been achieved, especially in the forward direction. The simulated half-power beam width (HPBW) is 77° and the measured HPBW is 77.4°. Both HPBWs is taken in the H-plane.

The large deviations between the antenna model and the manufactured antenna did not affect the radiation pattern. The reason for this is, as discovered in [1], that the radiation properties of the antenna is far less affected by changes in the geometry compared to the input impedance. This means that deviations between the antenna model and the manufactured antenna do not affect the radiation pattern as much as the input impedance.

4 Design of the array

In this chapter the design of the array antenna is presented. The design procedure is described and all choices done during the design are explained. The original antenna element presented in chapter 3 had to be modified owing to required element spacing and production cost. These modifications are presented. Also methods for increasing the scan range are discussed, such as DGS, EBG, and adaptive matching circuits.

4.1 Design procedure

A set of specifications are used as a starting point for a system design. For an array specifications such as directivity, side lobe level, and scan range, are used to determine the geometry and overall setup. For example a minimum requirement for the directivity gives a limit on the minimum number of elements, and if a limit on the maximum side lobe level is given, the use of a nonuniform amplitude distribution should be considered.

For this project the specifications are listed in Table 3.

Table 3: Specifications

Specification	Value
Size	8x8
Frequency band	8 - 8.5 GHz
Polarization	Linear
Scan direction	Horizontal and vertical
Maximum reflection coefficient	-10 dB
Scan range	Maximize
Grating lobes	No

From Table 3 the first thing that can be noticed is that the size of the array is given. This puts a limit on the maximum obtainable directivity of the array, as can be seen from equation (2.17).

No specification on maximum side lobe level was given and no limit was made. The reason for this is that the side lobe level is reduced by individual amplitude weighting of the radar channels and this is not part of the assignment. It should be mentioned that the use of an 8x8 array puts a limit on the minimum obtainable side lobe level for a uniform array. This can be seen from Figure 2 in the theory chapter.

To determine the maximum element spacing without exciting any grating lobes a maximum scan range needs to be set. Since it is specified that the scan range should be maximized one could set the scan range to be $-90°$ to $-90°$. No previous work was found where such a large scan range was achieved. A scan range of $-90°$ to $90°$ was therefore deemed as unrealistic.

Refs. [10], [11], [12] and [13] report that scan ranges close to $-70°$ to $70°$ had been achieved. The maximum scan range was therefore set to be $-70°$ to $70°$. This scan range applies in both vertical and horizontal planes.

When developing the antenna element no mathematical model was found and therefore an iterative trial and error process was used to design the antenna element. For an array mathematical models do exist, as presented in the theory chapter. These were used to design the array and predict its properties.

First the geometry of the array was determined. It was then discovered that the original antenna element needed modifications, a new antenna element was therefore designed. A model of the array was made in HFSS and simulated using the unit cell and Floquet port simulation setup. This simulation setup was used to tune the input impedance of the array so that a -10 dB reflection coefficient was achieved over as wide scan range as possible. To increase the scan range several methods were investigated; electromagnetic bandgap materials (EBG), defected ground structures (DGS) and adaptive matching circuits. Because of problems explained later none of these methods were used.

Reaching the specified scan range was a challenge, but [10]- [13] suggest that a large bandwidth gives a large scan range. The bandwidth of the antenna was therefore increased, and larger scan ranges were achieved.

To verify the simulation results obtained by using the unit-cell and Floquet ports simulation setup a more extensive simulation setup was used, namely the Finite Array DDM method.

4.2 Array design

4.2.1 Geometry of the array

The geometry of the array means its mechanical structure, like the number of elements, the spacing between elements, or the lattice structure. The geometry has a large effect on the array properties, especially the radiation pattern. This can be seen from equation (2.25), which is the array factor for a rectangular array. The geometry of the array will also to a lesser degree affect the element pattern. The reason is that the level of mutual coupling between elements is dependent on the distance and relative placement of these elements.

Important properties of a radar antenna are the half-power beamwidth (HPBW), the maximum side lobe levels, and the grating lobes. In a radar application a narrow main beam is important to achieve a high angular resolution. Low side lobe levels are important to eliminate reflections through the side lobes. Grating lobes are not wanted since large amounts of energy will be transmitted and received in unwanted directions, which will lead to detection of targets at different directions than the main beam. The properties discussed above are all controlled by the geometry of the array.

As shown in the theory chapter the width of the main beam is controlled by the number of elements in x and y-direction, and the element spacing. So to obtain a narrow main beam either a large number of elements, large element spacing, or both could be used. A large number of elements will also reduce the side lobe levels. If the element spacing is larger or equal to half the wavelength grating lobes will occur for large scan angles. This puts a limit on the element spacing. The element spacing should be as large as possible without any grating lobes occurring, so that the directivity is maximized and the mutual coupling between elements is minimized.

Since an 8x8 array was specified the only parameters left to decide for the geometry was the lattice structure and element spacing d_x and d_y. A quadratic lattice structure was chosen, this means that $d_x = d_y$. This was done because the scan range in both x and y-directions should be equal. It also gives the option for both horizontal and vertical polarization since the array can be tilted 90° without any change in properties except for polarization.

To determine the element spacing equation (2.15) (repeated here for convenience) were used to establish an upper limit on the element spacing.

$$d_{max} < \left| \frac{\lambda_0}{sin\theta_{max} - sin\theta_{Smax}} \right|. \tag{4.1}$$

This equation is derived for linear arrays, but will work for a quadratic array as shown in the theory chapter. Using the wavelength corresponding to the highest frequency (8.5 GHz) and $\theta_{Smax} = 70°$. For an array scanned to 70° the first grating lobe will occur at -90°, therefore $\theta_{max} = -90°$. This gives a maximum element spacing of 18.2 mm. Making the element spacing smaller than 18.2 mm guarantees that no grating lobe will reach its maximum level for the entire scan range. However, large parts of the first grating lobe will be visible if the element spacing is not made small enough. HFSS was therefore used to find an element spacing that reduced the grating lobe to the same level as the side lobes. This was achieved with an element spacing of 16.5 mm.

4.2.2 Antenna element

Since the element spacing was determined to be 16.5 mm the antenna element needs to fit inside a 16.5x16.5 mm^2 area. The original antenna element could not fit inside this area and therefore was made smaller. To achieve a smaller area the RF-transition was moved closer to the via cage and the size of the via cage was reduced. These changes ensured that the antenna element would fit inside the given area.

One of the specifications for the original antenna element was that electronic components should be mounted directly on the backside of the antenna element. An extra layer of substrate was therefore added. This specification was no longer valid and therefore the extra component layer was removed. This reduces the production cost since one less substrate layer

is used. The SMA connector was placed directly over the RF-transition on the ground shield. This removes the need for extra vias that connects the connector to a ground plane.

In chapter 3 the problems of using a too thin top layer were discussed. For the new design a thicker substrate was therefore used. A thickness of 0.508 mm was chosen. This is still thin, but together with a bonding material the problems encountered when using a thin top layer should be solved.

The stack up of the new antenna element can be seen in Figure 24.

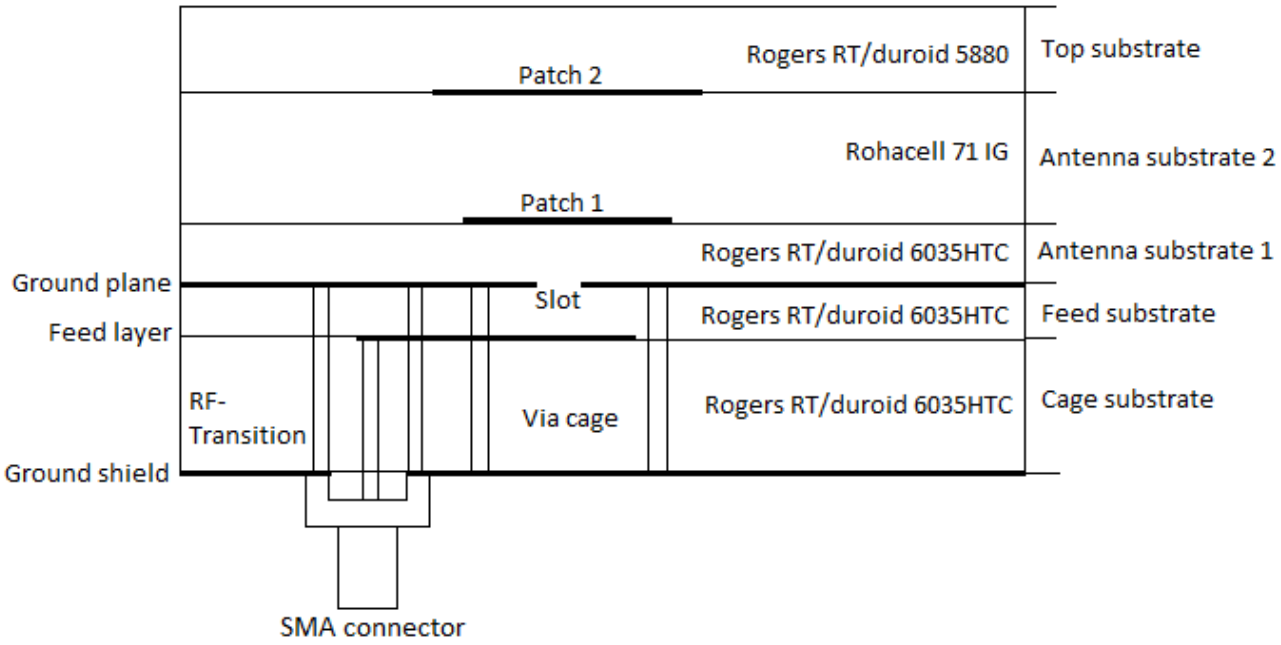

Figure 24: The new antenna stack up

From Figure 13 it is seen that the original antenna element had a hole in the ground plane where the RF-transition ended. This was done to reduce the complexity of production, since one less via type was needed. This hole in the ground plane was not optimal since it gave a slightly skewed radiation pattern and increased levels of cross polarization. In the new antenna element the hole was removed, as can be seen in Figure 24

To increase the bandwidth of the original antenna element the aperture coupled stacked patch (ACSP) configuration as presented in the theory chapter was used. For reasons discussed in more detail later in the report the ACSP configuration could not be used. Instead the resonant aperture stacked patch (ASP) configuration was used. This means that the length of the slot was increased to such an extent that the slot became a radiating element.

The final dimensions of the antenna element can be found in Appendix D

4.2.3 Element pattern

From pattern multiplication it is clear that the radiation pattern of an array is not only dependent on the array factor but also on the single element pattern. It is therefore important that the antenna element has a radiation pattern that fits the application. For this application the optimal radiation pattern is shown in Figure 25(a)-(b). The two plots shows the radiation pattern in the θ-plane and φ-plane. The optimal pattern in the θ-plane is a perfect half circle. This means no radiation in the backwards direction, and a constant gain over $-90° \leq \theta \leq 90°$. Constant gain over the scan range is important since the main beam will not experience scan loss. The optimal pattern in the φ -plane is a perfect circle (the antenna is omnidirectional). This means that the main beam can be scanned in any φ-direction without suffering scan loss. The optimal single element pattern shown here will enable a full scan in the forward direction and remove all backwards radiation. The scan volume is a half -sphere. This pattern is impossible to obtain in practice, but patch antennas can approximate it.

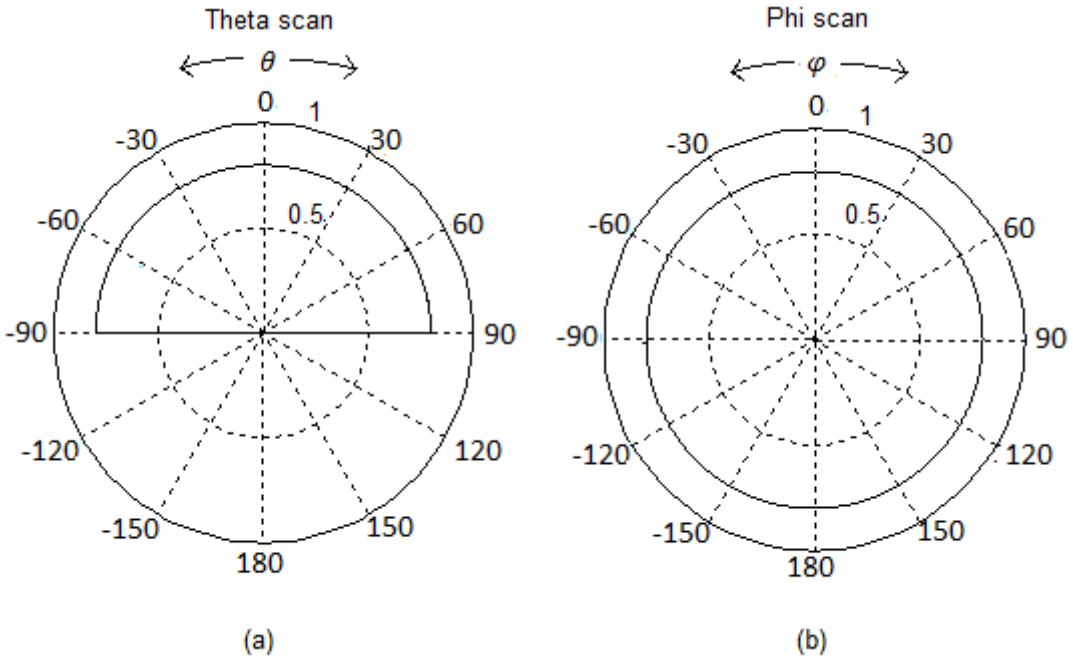

Figure 25: Optimal single element radiation pattern.

The radiation pattern of the antenna element is shown in Figure 26. Comparing this radiation pattern to the optimal pattern in Figure 25(a) it is clearly seen that this radiation pattern is far from optimal. It has a large backwards radiation and the gain decreases rapidly away from broadside. This would lead to a large scan loss. This element pattern would severely degrade the scanning performance of the array, making a scan range of $-70°$ to $70°$ unwanted in a practical application.

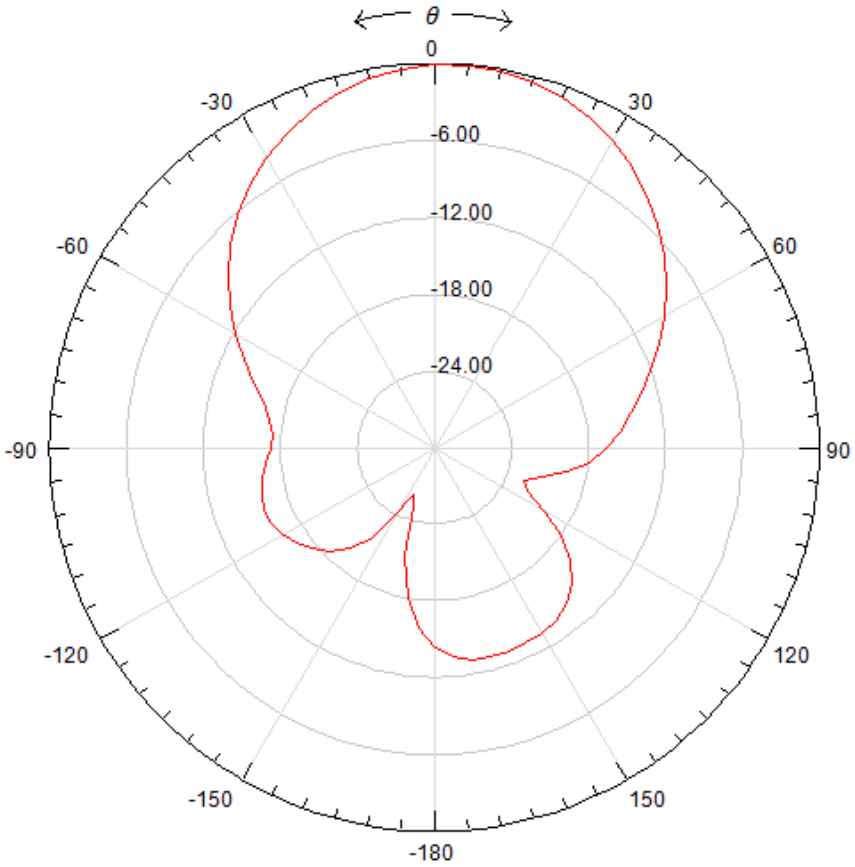

Figure 26: Normalized gain in dB for an antenna element, E-plane (φ=0°).

The pattern had to be improved and a search for possible solutions was conducted. It was discovered that placing the antenna element in an array environment would improve its radiation pattern. This can be seen in Figure 27, where the radiation pattern of an antenna element placed in an infinite array is plotted. The reason for this improvement is the mutual coupling between the elements. It is clear that this element radiation pattern is a better approximation of the optimal radiation pattern. It has a more constant gain, at $\pm 70°$ the gain has only decreased by approximately 6 dB. The element radiation pattern is also more symmetric, which is caused by the infinite array environment. This element radiation pattern was a large upgrade and would give a much better scan performance.

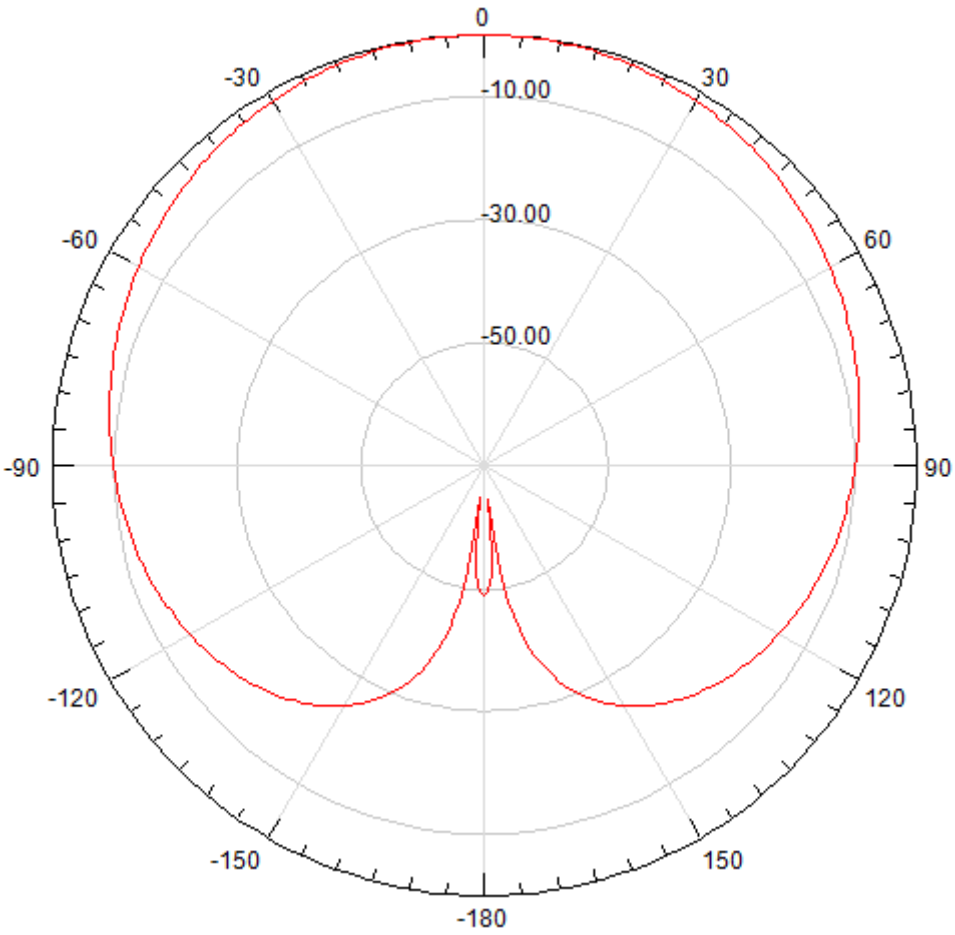

Figure 27: Normalized gain in dB for an antenna element placed in an infinite array, E-plane ($\varphi = 0°$).

As mentioned this element radiation pattern is valid for elements placed in an infinite array. Obviously an 8x8 array is not infinite. The infinite array assumption was expected to be a good approximation for elements placed in the middle of the array. However, for elements on the edges the radiation pattern will differ, due to diffraction on the edges and an uneven effect from the mutual coupling. Simulations have been conducted to determine the edge element radiation pattern and the results can be seen in chapter 5.

4.2.4 Increasing the scan range

A scan range of $-70°$ to $70°$ for both the horizontal and vertical plane was the goal. Early in the process it was realized that the goal was set very high. The reflection coefficient increased rapidly for increasing scan angles, and scan ranges of only $-30°$ to $30°$ was achieved in the beginning. This of course was too low and additional methods to increase the scan range was therefore investigated, such as; DGS, EBG, and adaptive matching networks. None of these techniques ended up being used for reasons explained in later sections.

Wide scan ranges have been achieved in [10], [11], [12] and [13] using a similar antenna element. None of these designs used any methods for reducing surface waves, nor were other techniques presented that would increase the scan range. The only reason observed for the large scan range was the large bandwidths. It was therefore suspected that a relationship between a large bandwidth and a wide scan range existed. Because of this suspicion the antenna element was redesigned to increase its bandwidth.

The original antenna element used an aperture coupled stacked patch configuration (ACSP) to achieve a bandwidth of 13%. To increase the bandwidth of the antenna element the aperture stacked patch (ASP) configuration was used. This meant that the length of the slot was increased to a point where it became resonant. This would form an extra loop in the Smith chart (see Figure 55(c) in Appendix A.1), and therefore increase the bandwidth. The length of the slot was initially set to $\lambda_g/2$, where $\lambda_g$is the wavelength in the substrate. $\lambda_g/2$ should be the length where the slot becomes resonant. HFSS was then used to optimize the length.

Using the ASP configuration increased the bandwidth significantly and the scan range increased immediately. One drawback using the ASP configuration is the increase in backwards radiation since the slot now is a radiating element. Due to the ground shield and the via cage no significant increase in backwards radiation was observed.

4.2.5 Tuning

As stated several times earlier the mutual coupling between elements will affect the input impedance of the antenna elements. It was therefore necessary to re-tune the antenna element to achieve an acceptable reflection coefficient. The input impedance is also dependent on the scan angle, and this effect was accounted for when the array was tuned.

To tune the antenna element HFSS was used. Three methods for simulating arrays are presented in chapter 2; the Finite array method, the Finite array DDM, and the unit-cell with Floquet port. The last option was used during the tuning because of its low simulation times. This method places the antenna element in an infinite array environment. It accounts for mutual coupling and scan blindness, but not edge effects because of the infinite array assumption. For larger arrays the infinite array assumption will give accurate simulation results, especially for the input impedance and element pattern of the central elements. This is confirmed by [9] which used the unit-cell method to design an 8x8 array, and good compliance between simulated and measured results was achieved.

The antenna element was tuned using guidelines from [7]. The length of the patches was adjusted to find the right resonance frequency and control the level of coupling between the patches. The thickness of the antenna substrates was adjusted to find the right level of coupling between the two patches and the slot. The level of coupling between the slot and the lower patch, and the lower and upper patch should be balanced to achieve a large bandwidth. The two different coupling levels determines the size of each loop in the Smith chart, if one coupling level is much larger than the other it will dominate and one loop will be eliminated,

thus decreasing the bandwidth. The thickness of the antenna substrates are therefore very important and the input impedance of the antenna is very sensitive for changes in the substrate thicknesses.

Some problems achieving a balanced level of coupling was encountered. The reason for this was later discovered to be the use of the H-shaped slot. This slot shape made the coupling level between the slot and the first patch so big that it dominated the coupling between the lower and upper patch. To achieve a balanced coupling level the thickness of antenna substrate 1 was increased significantly. This lead to an increase in the mutual coupling between elements since more surface wave modes was excited (see equation (2.52)). An easy solution to this problem would be to use a rectangular slot. This would decrease the level of coupling between the slot and the lower patch approximately by a factor of three and therefore a thinner antenna substrate 1 could have been used. Unfortunately this was not considered at this stage and the rectangular slot was therefore not used in this design.

The tuning was done in several iterations. When an acceptable scan range was achieved a simulation using Finite array DDM simulation setup was conducted to verify the design.

4.2.6 Production

The array consists of 64 antenna elements placed in a quadratic lattice structure. Expanding the antenna element into an array does not add significant complexity to the manufacturing process since the antenna elements are patch antennas. Etching 64 identical geometries in a periodic pattern on a substrate does not increase the complexity significantly.

The complete stack up of the antenna element can be seen in Figure 24. It is built up of five substrate layers. It has two types of blind vias; ground shield to ground plane, and ground shield to feed layer. Eliminating the buried vias used in the original antenna element simplifies the manufacturing process. Only two curing cycles are needed to bond the three lower layers.

The original antenna element was produced in three parts and plastic screws were used to connect them. The reason for this was that no bonding material with low enough cure temperature and pressure was found. The foam layer cannot handle high temperature and pressure without being deformed. Using plastic screws to hold the array together is not a good solution. The antenna input impedance is very sensitive to deviations in thickness of the different layers. Using screws will most likely introduce an error in the distance between the patches and therefore alter the input impedance.

It was decided to use two bonding materials to achieve a good bond between the three lower layers and the foam layer could be attached without using high temperature. For the bottom three substrate layers a bonding material from Taconic (FR-26-0025-60) should be used. This material was used in the original antenna element and a good bond was achieved. Advantages are the low loss tangent, a thin pressed thickness, and it can handle multiple bonding cycles. For the two upper layers Tencate BF548 should be used. It has a low curing temperature of

82° and it works for foam structures. The properties of the two bonding materials are listed in Table 4.

Table 4: Bonding materials

Type	Dielectric constant	Loss tangent	Pressed thickness
FR-26-0025-60	2.60	0.0014	< 2.8 (mil)
Tencate BF548	3	0.017	-

The minimum size of the array was set when the element spacing was determined. An element spacing of 16.5 mm gives a minimum array size of 132x132 mm^2. To decrease the effect of diffraction the array was made bigger, as can be seen in Figure 28. The array size was chosen to be 400x400 mm^2. This means that it is 134 mm from the edge element to the edge of the antenna. This should reduce the diffraction and therefore reduce the backwards radiation. The edge element radiation pattern should also be less affected.

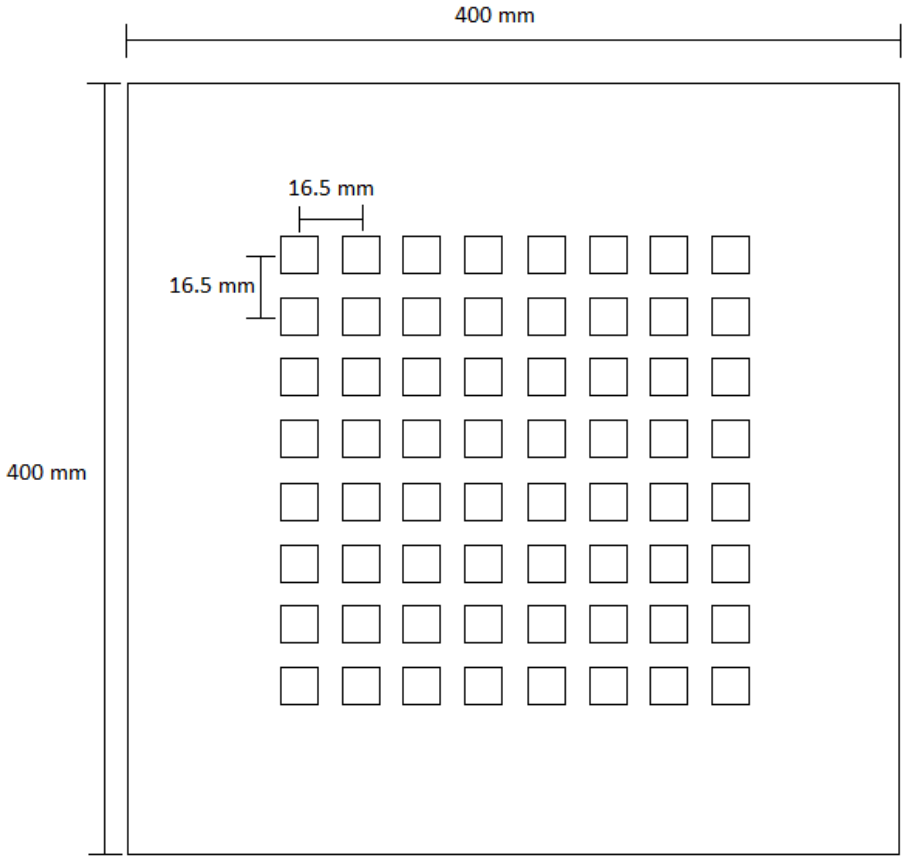

Figure 28: Front view of the antenna array.

The full schematic of the antenna can be found in Appendix D

4.3 Mutual coupling

Since mutual coupling affects the arrays properties it was necessary to get a deeper understanding of the mutual coupling in the array. Especially interesting was it to see how large portion of the mutual coupling was due to surface waves, also the element spacing effect on the mutual coupling levels was investigated.

A 2x2 quadratic array was modeled in HFSS using the same antenna elements as the main array and the same element spacing. To determine the effect of surface waves on the mutual coupling two versions of the array were simulated. One regular array, and one where the antenna elements were separated by perfect electric conductor (PEC) walls. This effectively stopped all waves traveling through the substrates. One could therefore compare the level of coupling between elements with and without the waves traveling through the substrate. For this antenna there are two types of waves traveling through the substrate; the surface waves, and the parallel plate modes that is excited in the substrate between the two ground planes. It was expected that the surface waves were the largest contributors since the via cage is shown to effectively attenuate the parallel plate modes [1]. To confirm this a simulation was conducted where PEC walls were used only for the two lower substrate layers. The results showed no significant reduction in mutual coupling level compared to the array without PEC walls. This meant that the parallel plate modes do not contribute much to the mutual coupling level.

Simulations with different element spacing were also conducted. The results of the simulations are presented in chapter 5.

4.4 DGS and EBG

Surface waves are a big problem when trying to increase the scan range, this have been suggested by earlier work [9] and antenna literature [3, p. 866]. Therefore some work was done to find methods which reduces surface waves. Two such methods were investigated and are presented here. The first method is the use of electromagnetic bandgap materials (EBG), and the second is use of defected ground structures (DGS).

4.4.1 EBG

Electromagnetic bandgap materials can be used in many applications. Of special interest here is the use of EBG materials to attenuate surface waves. The EBG structure is a periodic structure which works much like a band stop filter for surface waves [14]. By surrounding the antenna element with EBG material the surface waves excited by the antenna element will be severely attenuated. The EBG material is frequency dependent and should therefore be designed for the center frequency of the antenna. EBG material consists of photonic crystals which are made by cutting out defects in the substrate. It is a complicated process and difficult to manufacture. For this reason the EBG was not an alternative for this design.

4.4.2 DGS

Defected ground structures is a method used to reduce surface waves. It works as a filter that attenuates the surface waves at certain frequencies. DGS is a simple structure that consists of an etched out shape (the defect) in the ground plane. This defect will alter the current distribution on the ground plane and if the right shape and dimensions are used it will attenuate the surface waves very effectively [15]. Several methods of reducing surface waves are compared in [15], among them DGS and EBG. The presented results shows that DGS is more effective in reducing surface waves than EBG. Due to the simple structure of the DGS no additional steps to the manufacturing are needed. This makes DSG easier to realize and will therefore save money. For these reasons DGS was chosen as the preferred option.

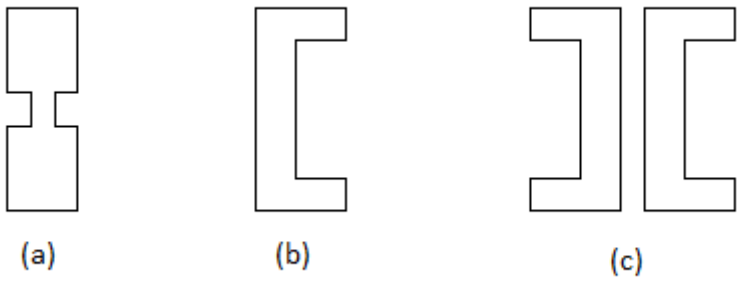

Figure 29: Three different ground defect structures. (a) Dumbbell (b) U-shape (c) back-to-back U-shape

In [16] three different shapes for the ground defect are compared; dumbbell, U-shape and back-to-back U-shape. It is shown that back-to-back U-shape has twice the rejection bandwidth as the other shapes. The reason for the increase in rejection bandwidth is that the back-to-back U-shape is a cascade of U-shape defects. Cascading circuit elements leads to broader rejection bands [16]. The back-to-back U-shape structure was therefore chosen since it has the largest rejection bandwidth and therefore the best chance of covering the required bandwidth of 8-8.5 GHz.

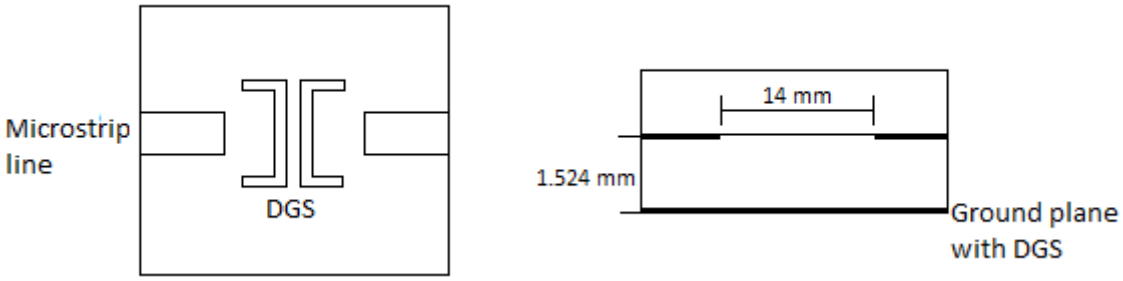

Figure 30: DGS test bench

A test bench was made with HFSS to tune the DGS. It consisted of two microstrip line stubs placed between two layers of substrate, as can be seen in Figure 30. These stubs will excite surface waves in the substrate. The distance between the two stubs was made large, so that the coupling due to the surface waves was dominant. The test bench can be seen as a two port network where S21 represents the coupling between the two stubs. The structure was tuned to have a notch at 8.25 GHz. For comparison, an equal model was built only without the DGS. The results are plotted in Figure 31.

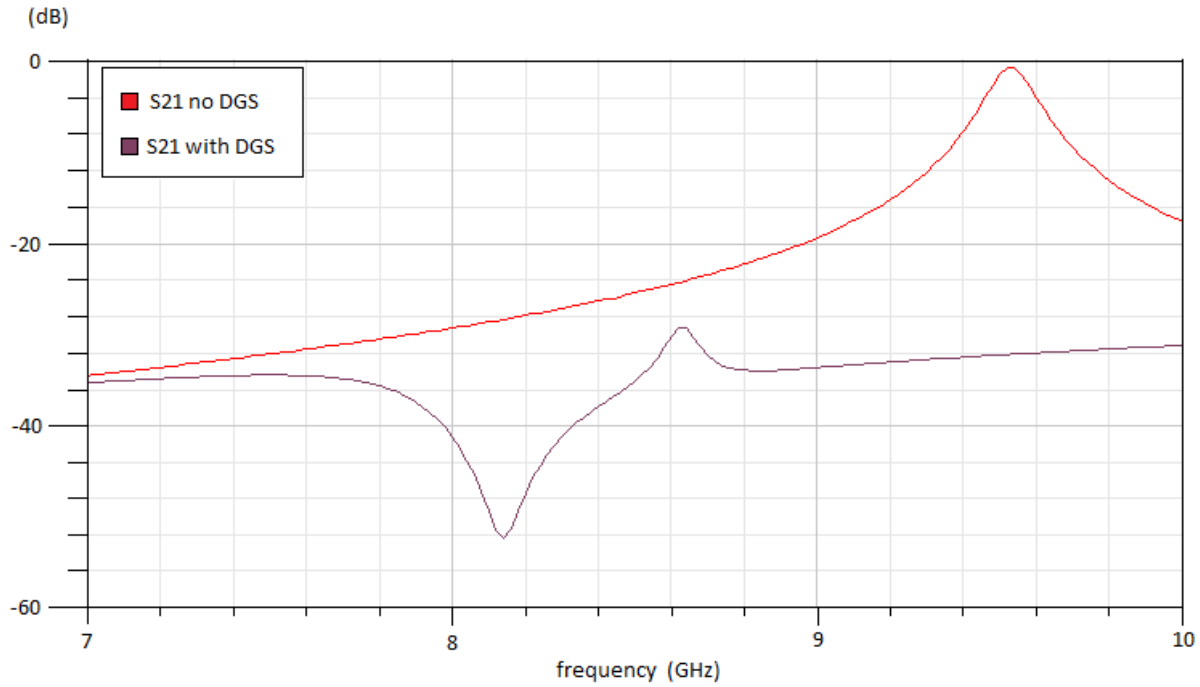

Figure 31: S21 with DGS and without DGS.

Comparing the two plots it is clear that the DGS effectively reduces the coupling. The center frequency is 8.19 GHz instead of 8.25 GHz. An attenuation of 24 dB is achieved at the center frequency and the 3 dB rejection band covers the required frequency band of 8-8.5 GHz.

The tuned DGS was then used in the array. No improvement on the arrays scan range was observed. It was suspected that the ground shield that is placed behind the first ground plane to reduce backwards radiation affected the DGS. The test bench was modified with a second ground plane and simulations showed that the ground shield removed the effect of the DGS. Removing the ground shield was not an alternative since it is very important to minimize the backwards radiation. The DGS was therefore abandoned.

4.5 Adaptive impedance matching

During the design of the array severe problems with increasing the scan range were encountered. This led to an extensive search for techniques that could be used to increase the scan range. One possible solution was found in [17]. Here an array of probe fed patch antennas was loaded with varactor diodes to increase the scan range. Each patch is connected to an varactor diode which is connected to ground. By changing the bias voltage over the varactor diode the input impedance of the antenna is changed. This means that the antenna can be matched for several different scan angles only by adjusting the bias voltage. Connecting a varactor diode to every patch in the array would be highly impractical, because of the added complexity to the manufacturing. For this reason the method was disregarded, but it was a starting point for a possible solution to the scan range problem.

If the varactor diode is moved from the patch to the input terminal of the antenna element, and a circuit being able to sense the reflected power and control the bias voltage over the varactor is added one would have a system that could automatically match the antenna. Figure 32 shows a block diagram of such a system.

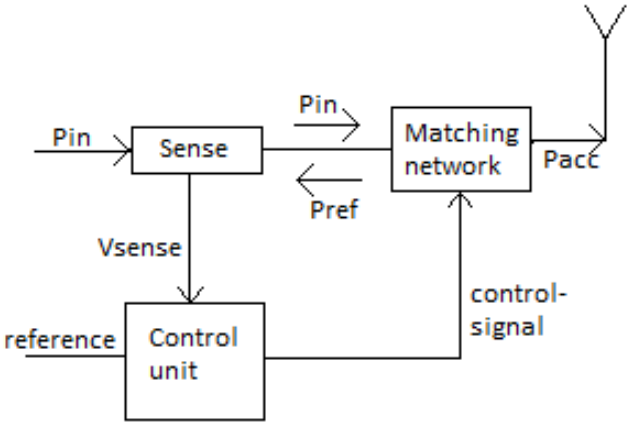

Figure 32: Block diagram of general adaptive impedance matching system

The matching network could be any topology that fits the matching requirements, the only demand is that it consists of some type of variable circuit element. The sense block represents a circuit that senses the reflected power and turns it into a signal the control unit can interpret. This is often a voltage level. The control unit compares the output of the sense circuit with a reference and decides what kind of control signal it should give the matching network. This is a basic adaptive matching circuit.

If an adaptive matching circuit is to be used to increase the scan range of the array several criteria has to be met. First it should be a space efficient and simple circuit since 64 circuits

has to be placed directly behind the array. The matching network should have a frequency band broad enough to cover the required frequency band. This is important so that the system only has to retune the matching for different scan angles. The control unit should be made without using microcontrollers, FPGAs or memory, this requirement is given to keep the complexity of the circuit down. Because of the large amount of power applied to each element the sense circuit should ideally transmit all of the input power through to the antenna.

It already exist many adaptive matching circuits with varying complexity and performance Three different systems are presented in [18], [19] and [20].

The sense circuit is often realized using a directional coupler as shown in Figure 33. The input power is applied on port 1, most of the power goes to port 2 continuing on to the matching network. Some power will be coupled to port 3. Port 4 is isolated. Some of the power will be reflected at the input terminal of the matching network. The reflected power will hit port 2 of the directional coupler and be coupled to port 4. Port 4 is connected to a circuit that converts the reflected power to a signal the control unit can interpret.

Figure 33: Directional coupler.

The level of coupling should be low so that only a small portion of the input power is lost. The low coupling level should not be a problem since a amplifier can be connected to port 4. Some of the input power will be lost due the coupling between port 1 and 3, this could be seen as a major drawback but [19] uses the coupled input power to its advantage. By comparing the phase difference between the reflected power and the input power (the phase of the reflection coefficient) the nature of the mismatch can be determined. For a positive phase difference the mismatch is inductive and for a negative phase difference the mismatch is capacitive [19]. Knowing the type of mismatch is a large advantage and leads to a simpler control unit. If the mismatch is inductive more capacitance is added to the matching network, and opposite if the mismatch is capacitive.

The matching network can be realized using any type of matching topology. A pi network is used in [20], a triple stub tuner is investigated in [18], and a simple LC circuit is used in [19]. These circuits uses variable capacitors to control the match. The variable capacitors can be

either varactors or switched capacitor arrays. Due to the large input power and high frequency it is not certain that elements for this application can be found.

As stated earlier the control unit should be made without complex digital circuitry. This could limit the performance of the adaptive matching circuit since the control algorithm has to be relatively simple.

Developing an adaptive matching circuit was found to be too time consuming and complex for this project. A simpler solution (increasing the bandwidth) was therefore chosen. However, further work on this subject would be of interest since a good adaptive matching circuit could improve the array performance. It will also make the array less affected by production errors and inaccuracies in the simulator since the matching circuit would tune out these error sources.

5 Results

This chapter presents results from the design. First simulation results and calculated results for the array are presented. Then measured results of the modified antenna element are presented.

5.1 Array

Since time did not allow for production of the array, only simulation results will be presented. The simulation results obtained using HFSS will be compared to computed results obtained using equations presented in the theory chapter.

5.1.1 Input impedance and scan range

Using the unit-cell Floquet port setup, the array input impedance has been simulated. Figure 34 shows the reflection coefficient for an antenna element placed in an infinite array environment.

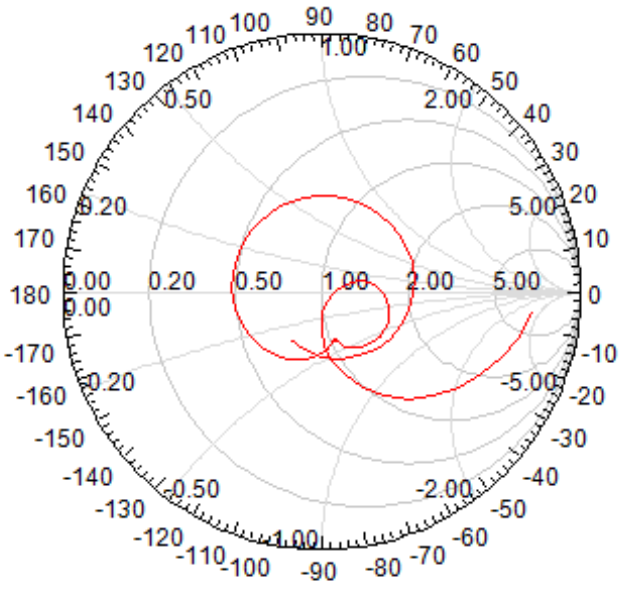

(a)

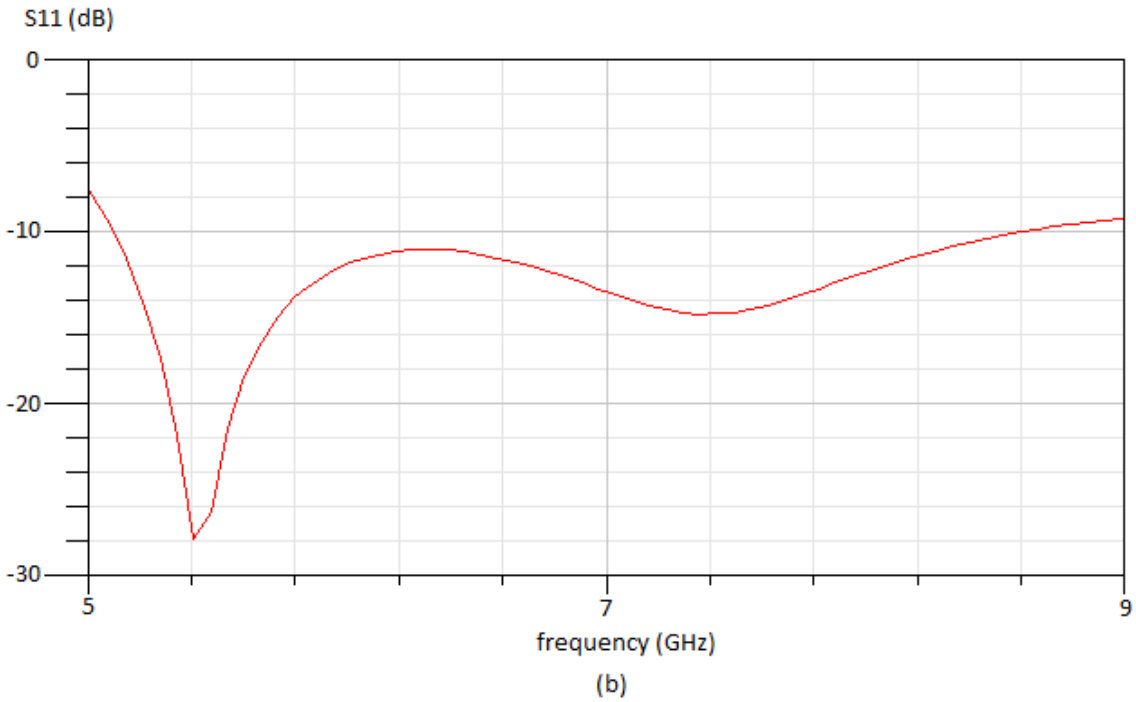

Figure 34: S11 plotted in (a) a Smith chart (b) in dB as a function of frequency. $\theta_S = 0°$.

For an array the input impedance will change as a function of scan angle. Figure 35 plots the reflection coefficient over a scan range of 0°-70°.

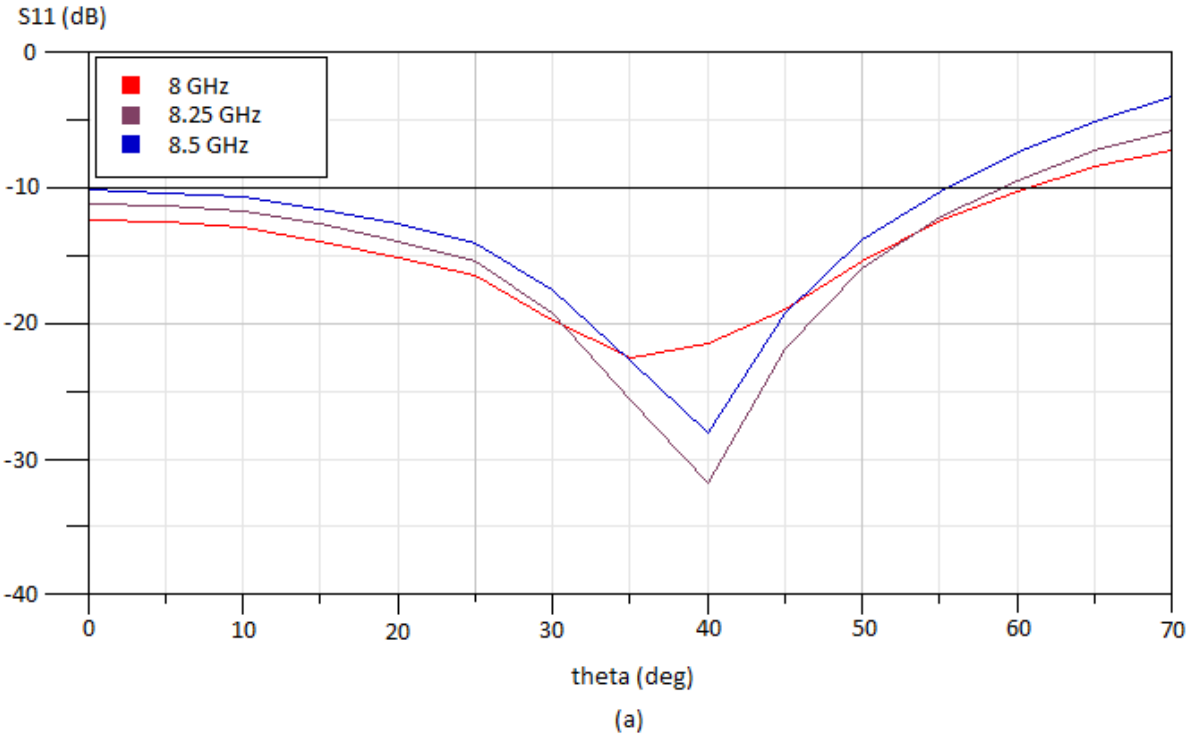

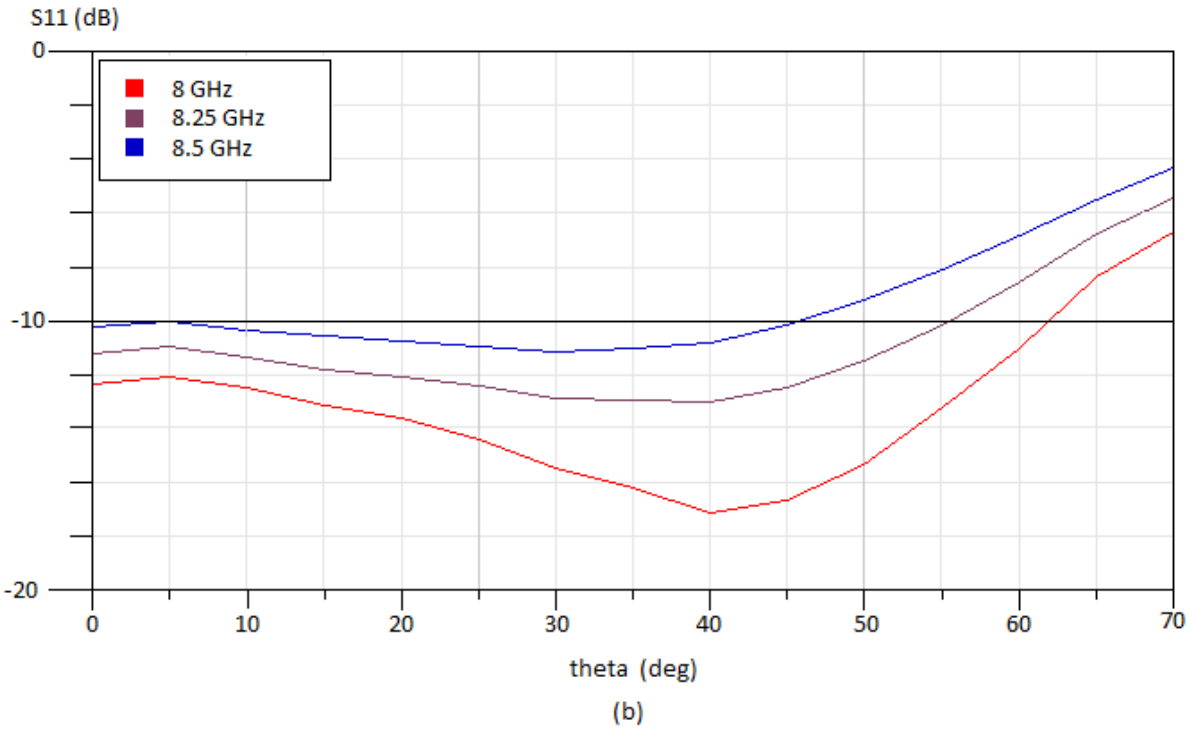

Figure 35: Reflection coefficient at different scan angels (a) E-plane scan ($\varphi = 0°$) (b) H-plane scan ($\varphi = 90°$).

To verify the accuracy of the unit-cell Floquet port simulation setup the array was simulated using the Finite array DDM method. The reflection coefficient of a few different elements are plotted in Figure 36

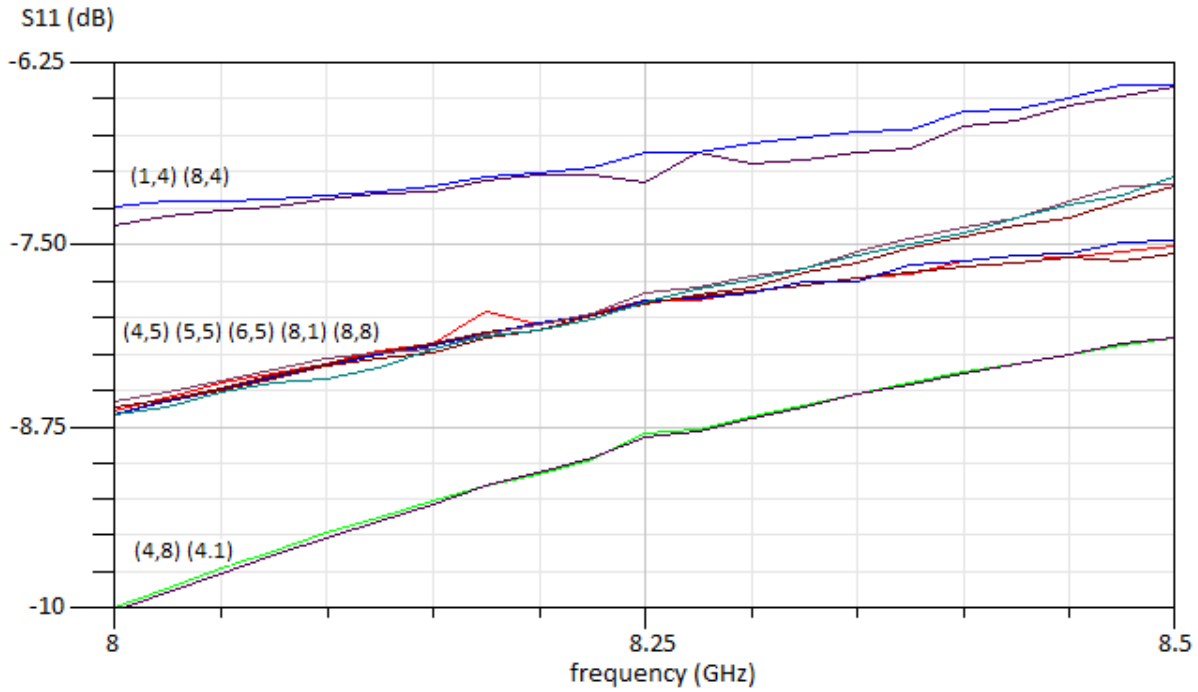

Figure 36: Reflection coefficient of different antenna elements for the array in broadside.

The notation (x, y) represents the placement of the element in the array. It is seen comparing Figure 36 to Figure 34(b) that large deviations between the two simulation setups exist. Also the reflection coefficient is above -10 dB in the entire frequency band, meaning that the antenna is not matched.

Some important antenna properties are listed in Table 5

Table 5: Simulation results for array

Parameter	Value	Unit
-10 dB reflection coefficient bandwidth at broadside	48	%
Scan range E-plane	-55° to 55°	deg
Scan range H-plane	-45° to 45°	deg
Radiation efficiency	>0.96	

5.1.2 Floquet analysis

Figure 37 shows the results of the Floquet analysis. Two different Floquet modes are plotted together with the reflection coefficient for three different frequencies. These plots show how much of the input power is transmitted to each Floquet mode. Mode 1 is the first propagating Floquet mode and represents the major lobe and Mode 2 is the second propagating Floquet mode and represents the first grating lobe.

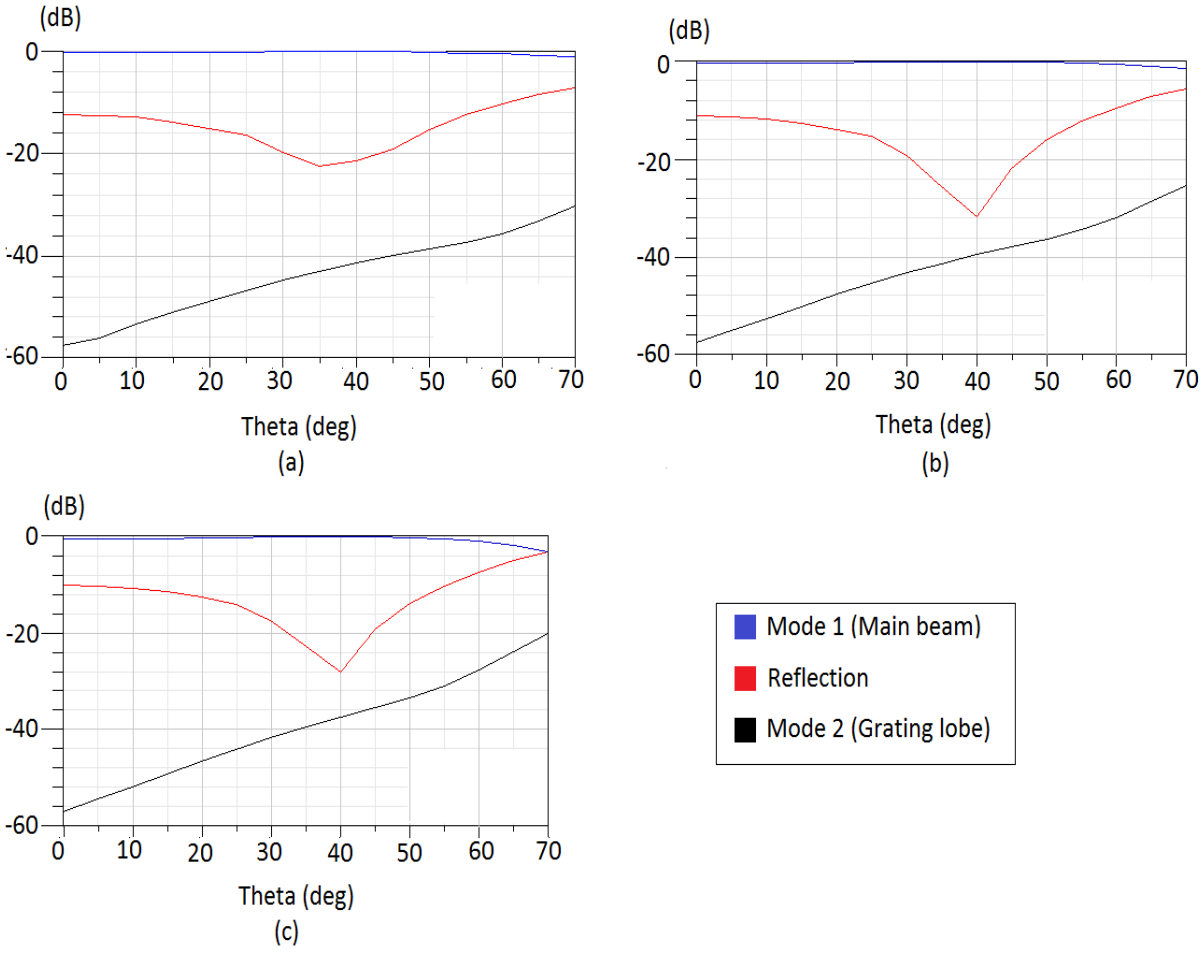

Figure 37: Plot of Floquet modes for (a) 8 GHz, (b) 8.25 GHz, (c) 8.50 GHz.

5.1.3 Radiation

HFSS uses pattern multiplication to determine the radiation pattern of the array. As stated in chapter 2 pattern multiplication does not include the effect of mutual coupling. However, HFSS uses the element radiation pattern of an antenna element placed in an infinite array environment, so the effect of mutual coupling on the element radiation pattern is included.

Figure 38 shows the normalized gain of the array scanned in four different directions.

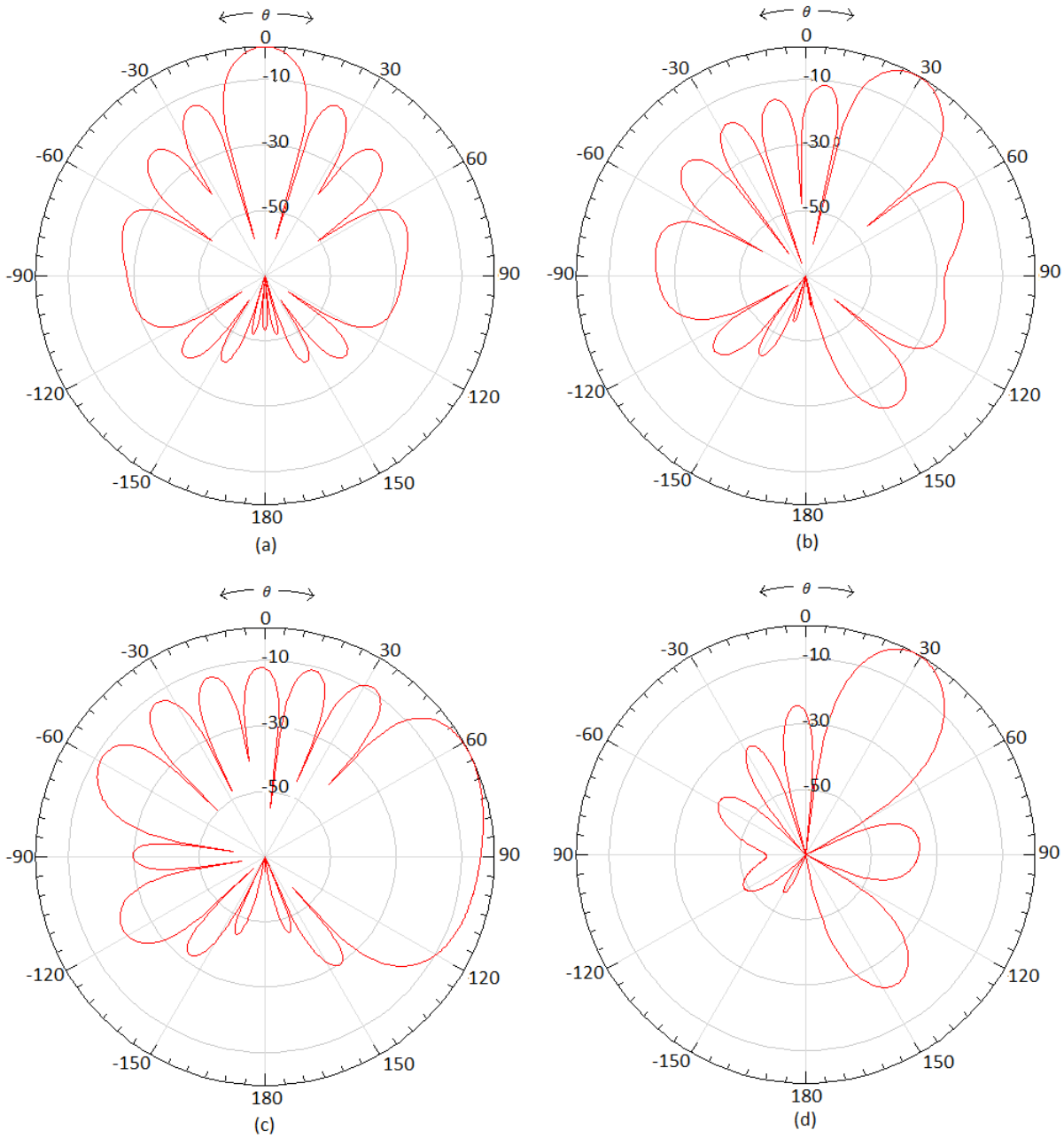

Figure 38: Polar plot of the normalized antenna gain in dB at 8.25 GHz for (a) the array in broadside, φ=0°, (b) the array scanned in $\theta_S = 30°$, $\varphi = 0°$, (c) the array scanned in $\theta_S = 70°$, $\varphi = 0°$, (d) the array scanned in $\theta_S = 30°$ and $\varphi_S = 45°$, $\varphi = 45°$.

The element radiation pattern of an antenna element placed in an infinite array environment is shown in Figure 39(a). To verify this result an 8x8 array is simulated using the Finite array DDM method. The radiation pattern for a central element is plotted in Figure 39(b), and the radiation pattern for an edge element is plotted in Figure 39(c).

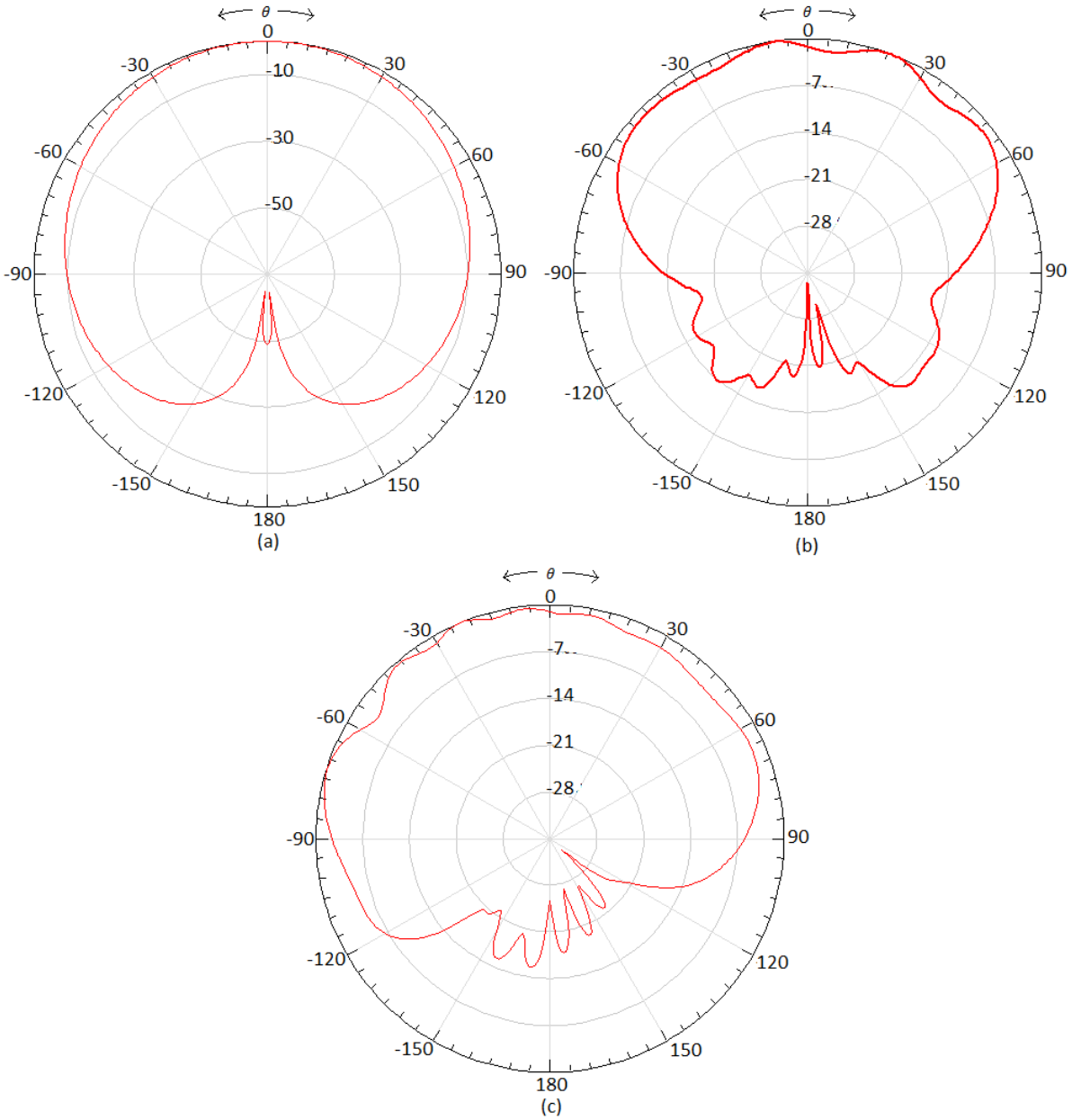

Figure 39: (a) Normalized gain for an antenna element placed in an infinite array, φ=0°, (b) normalized gain for a central antenna element, φ=0°, (c) normalized gain for an edge antenna element, φ=0°.

For more radiation patterns see Appendix C

Some important radiation properties are listed in Table 6

Table 6: Simulated radiation pattern properties

Scan angle	Max Gain (dB)	Directivity (dB)	Side lobe level (dB)	HPBW	Real scan angle
$\boldsymbol{\theta_S = 0°}$, $\boldsymbol{\varphi_S = 0°}$	22.1	22.2	-13.6	14°	$\theta_S = 0°$
$\boldsymbol{\theta_S = 30°}$, $\boldsymbol{\varphi_S = 0°}$	20.8	20.9	-11.5	15°	$\theta_S = 29°$
$\boldsymbol{\theta_S = 70°}$, $\boldsymbol{\varphi_S = 0°}$	16.4	16.5	-8.7	31.4°	$\theta_S = 63°$
$\boldsymbol{\theta_S = 30°}$, $\boldsymbol{\varphi_S = 45°}$	20.8	20.9	-24.3	16°	$\theta_S = 29°$

The side lobe level is calculated by comparing the largest side lobe level to the main beam. A side lobe level of - 13.6 dB means that the largest side lobe is 13.6 dB below the main beam. The real scan angle is the angle where the main beam has maximum gain.

To see the effect of the element pattern on the total radiation pattern, the array factor for all four cases presented above are plotted in Figure 40. These plots are obtained using a Matlab script provided by [3]. The Matlab script uses equation (2.25), which is the array factor for a rectangular array

Radiation pattern properties of the array factor are listed in Table 7.

Table 7: Radiation properties for array factor

Scan angle	Side lobe level (dB)	Directivity (dB)	HPBW	Real scan angle
$\boldsymbol{\theta_S = 0°}$, $\boldsymbol{\varphi_S = 0°}$	-13	22	13.8°	$\theta_S = 0°$
$\boldsymbol{\theta_S = 30°}$, $\boldsymbol{\varphi_S = 0°}$	-13	21.2	16°	$\theta_S = 30.2°$
$\boldsymbol{\theta_S = 70°}$, $\boldsymbol{\varphi_S = 0°}$	-13.5	18.5	70.1°	$\theta_S = 70.2°$
$\boldsymbol{\theta_S = 30°}$, $\boldsymbol{\varphi_S = 45°}$	-25	21.6	16.3°	$\theta_S = 30.2°$

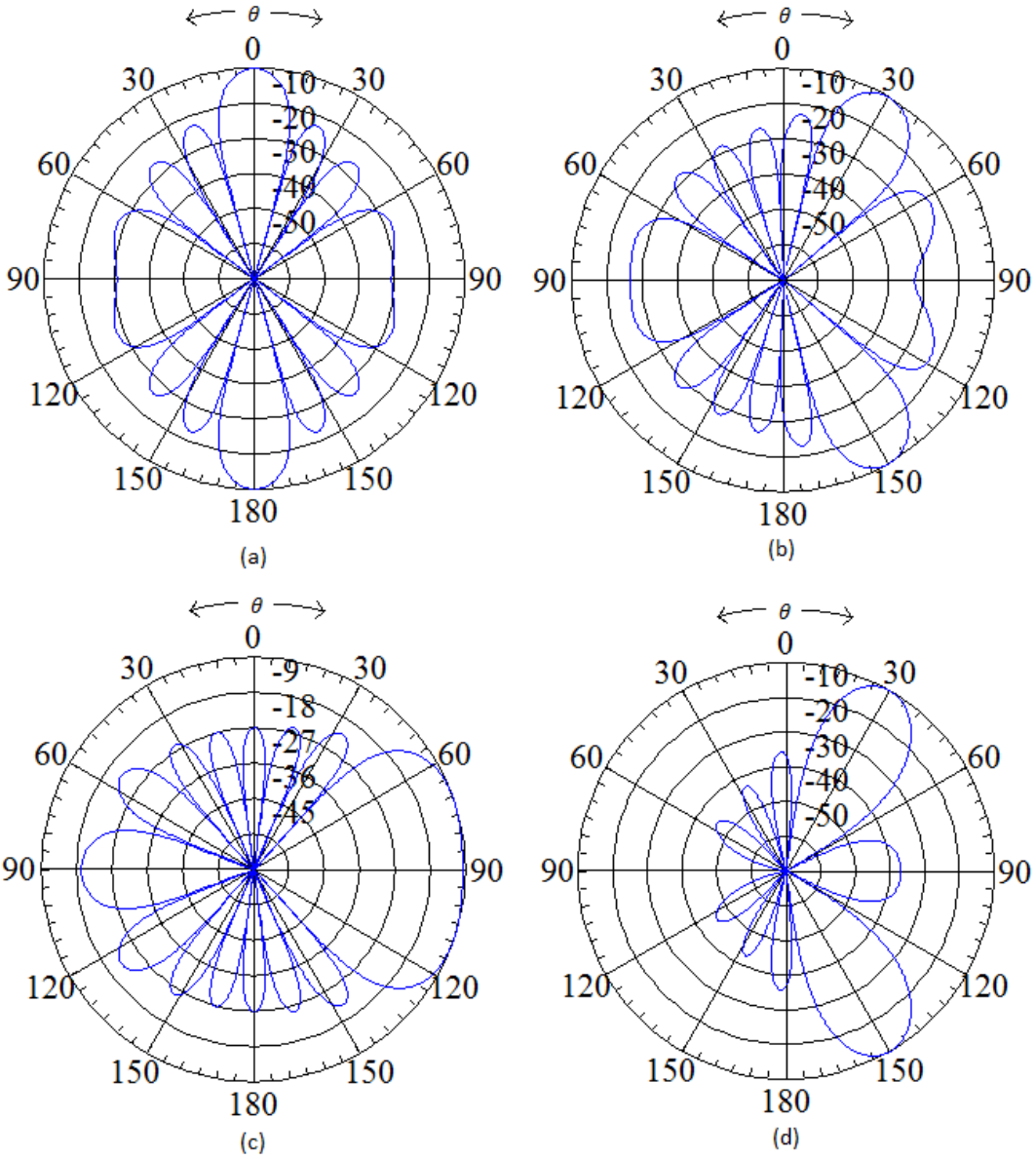

Figure 40: Normalized array factor of the array for scan angles (a) broadside, (b) $\theta_S = 30°$ and $\varphi_S = 0°$ (c), $\theta_S = 70°$ and $\varphi_S = 0°$, (d) $\theta_S = 30°$ and $\varphi_S = 45°$

In the theory chapter equations for calculating HPBW and directivity are presented. It is interesting to compare simulated and calculated results. The HPBW is calculated using (2.21) and (2.33) and the directivity is calculated using (2.17) and (2.20). The results obtained using theory are listed in Table 8.

Table 8. Calculated results

Scan angle	Directivity (dB)	HPBW
$\boldsymbol{\theta_S = 0°}$, $\boldsymbol{\varphi_S = 0°}$	8.7	13.6°
$\boldsymbol{\theta_S = 30°}$, $\boldsymbol{\varphi_S = 0°}$	8.1	15.7°
$\boldsymbol{\theta_S = 70°}$, $\boldsymbol{\varphi_S = 0°}$	4.1	39.8°
$\boldsymbol{\theta_S = 30°}$, $\boldsymbol{\varphi_S = 45°}$	-	15.7°

Comparing the results it is seen that the calculated directivity deviates from the simulated results. The reason for this deviation is equation (2.17), which do not model the directivity in broadside accurately. A large array is assumed used when deriving (2.17) and an 8x8 array is probably not large enough for this assumption to be correct.

Equation (2.20) (repeated here for convenience) was derived to describe how beam broadening affects the directivity.

$$D = D_0 \cos\theta_S \tag{5.1}$$

To verify this equation a better value for D_0 than (2.17) provided was used, $D_0 = 22.2\ dB$. The simulated and calculated directivity are plotted in Figure 41.

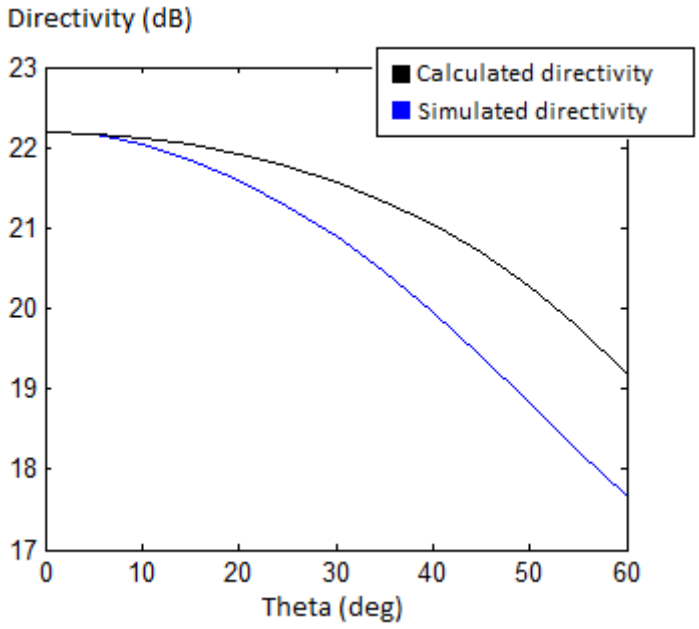

Figure 41: Simulated directivity compared to calculated directivity

5.1.4 Mutual coupling

An investigation on mutual coupling in the array was conducted using HFSS and the results are presented below.

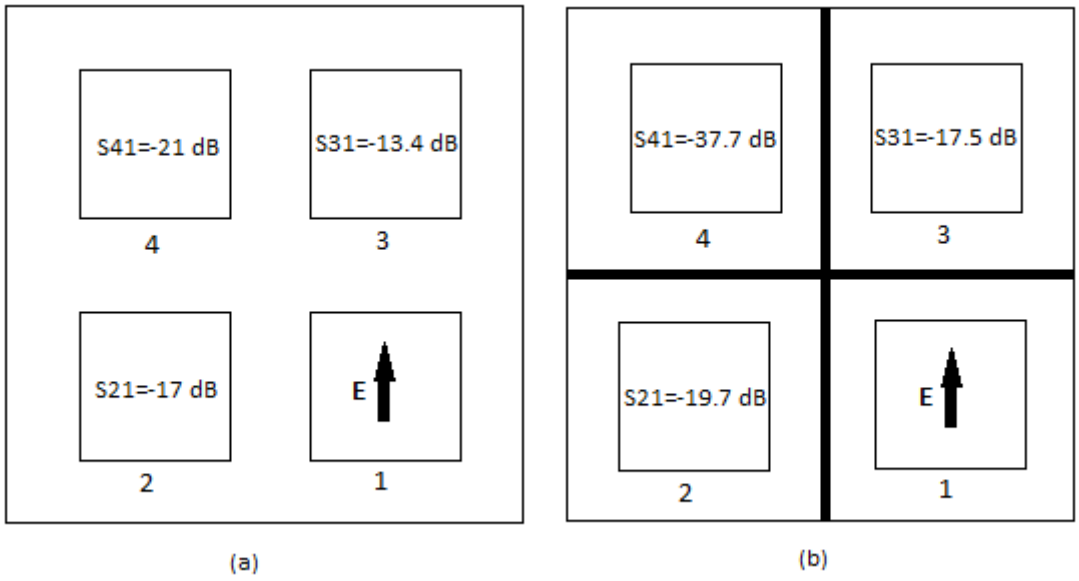

Figure 42: Results from simulations of mutual coupling using element 1 as reference. (a) Standard array (b) With PEC walls. An element distance of 16.5 mm is used.

Figure 42(a) shows the level of coupling between the elements of an 2x2 array, while Figure 42(b) shows the level of coupling in the same array, when the elements are separated by walls of a perfect electric conductor (PEC). It is seen that the coupling level has been reduced in Figure 42(b).

Figure 43 shows the level of mutual coupling between element 1 and 2, and element 1 and 3 for different element spacing.

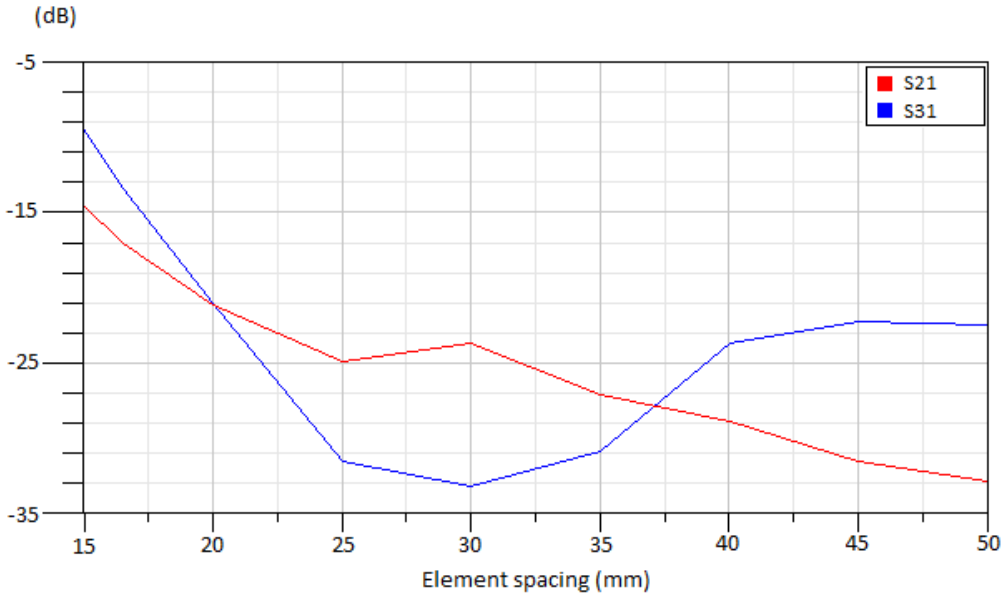

Figure 43: Mutual coupling levels in a 2x2 array for different element spacing.

Measurements of the mutual coupling between two of the original antenna elements was conducted with an element spacing of 50 mm. The results are plotted in Figure 44.

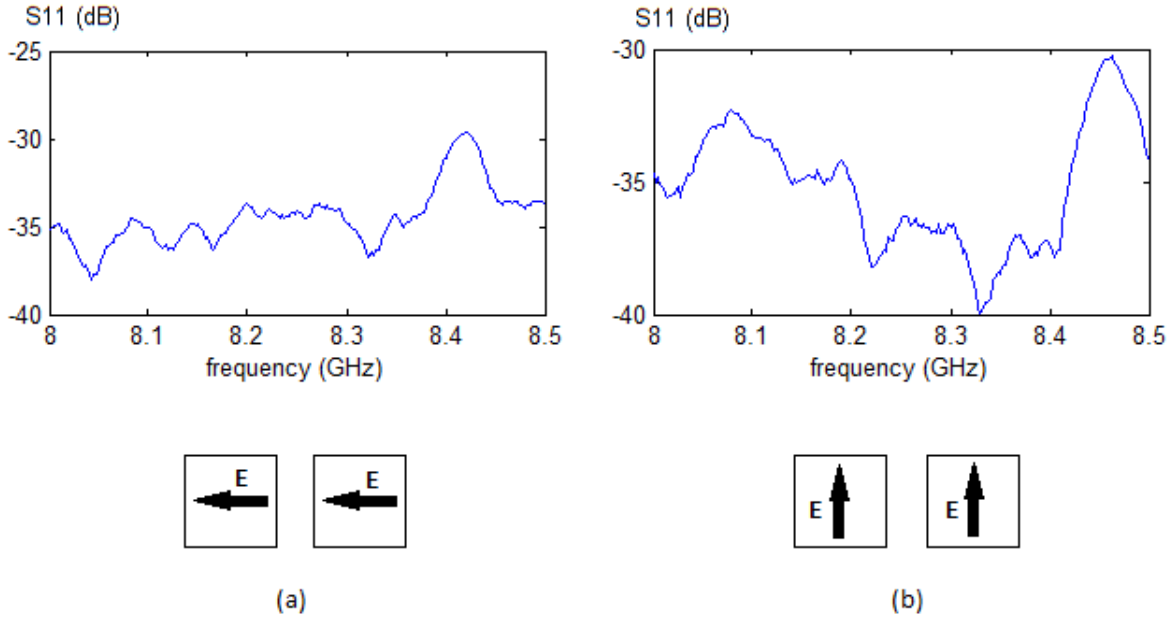

Figure 44: Mutual coupling between original antenna elements. (a) E-plane, (b) H-plane. Element spacing of 50 mm.

There is no physical contact between the two elements so it is assumed that no surface waves contribute to the mutual coupling.

5.2 The antenna element

Simulated and measured results of the modified antenna element as presented in chapter 3 are presented in this section.

5.2.1 Simulation results

The most important results are listed in Table 9.

Table 9: Simulation results for the modified antenna element

Parameter	Value	Unit
-10 dB reflection coefficient bandwidth	16	%
-20 dB reflection coefficient frequency band	8-8.45	GHz
Realized center frequency	8.29	GHz
Maximum gain	8.4	dB
Radiation efficiency	>0.96	

Figure 45 shows S11 or the reflection coefficient plotted in a Smith chart and in dB as a function of frequency.

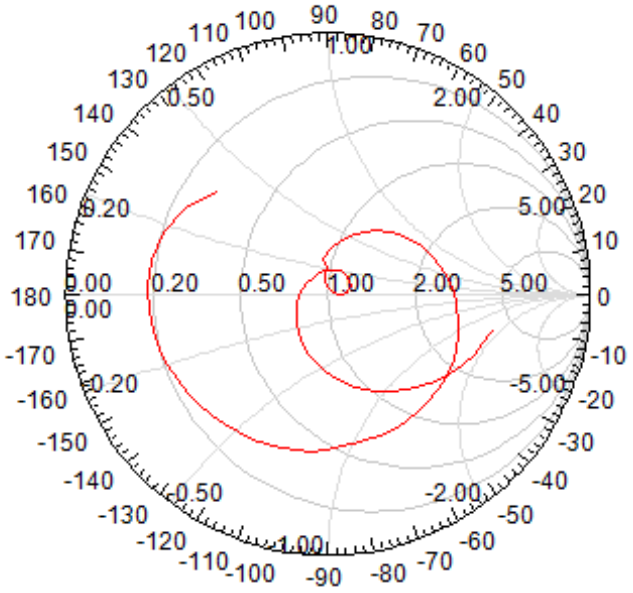

(a)

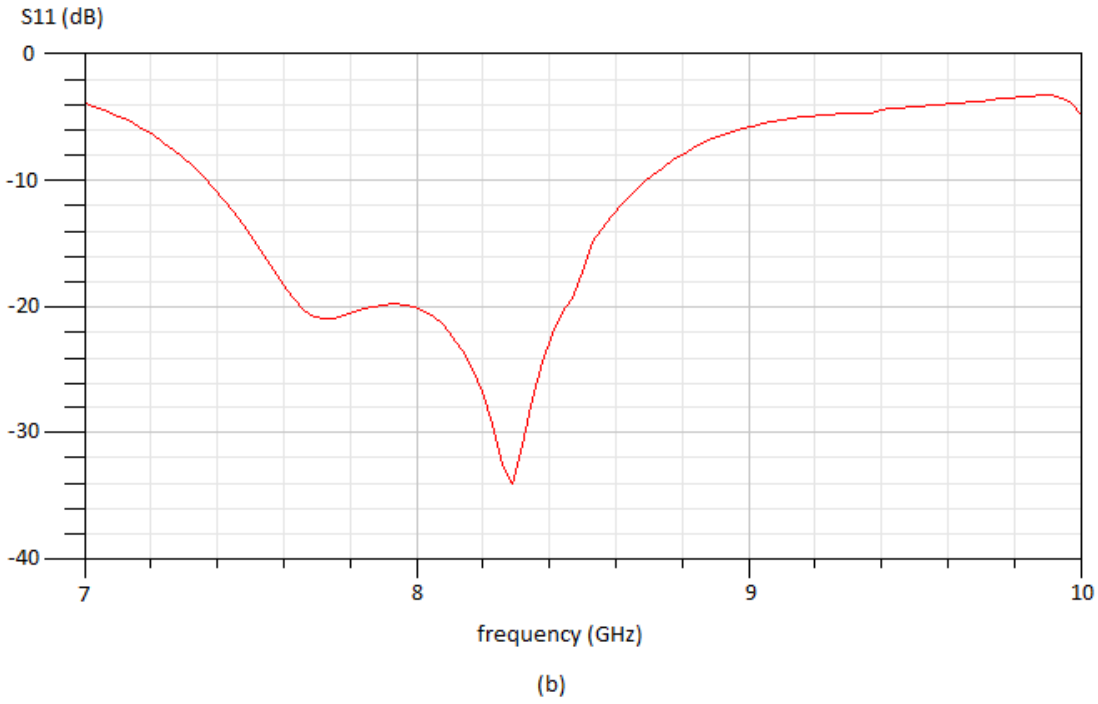

Figure 45: S11 plotted in (a) a Smith chart (b) in dB as a function of frequency

Figure 46 and Figure 47 shows the normalized gain of the antenna at 8.25 GHz.

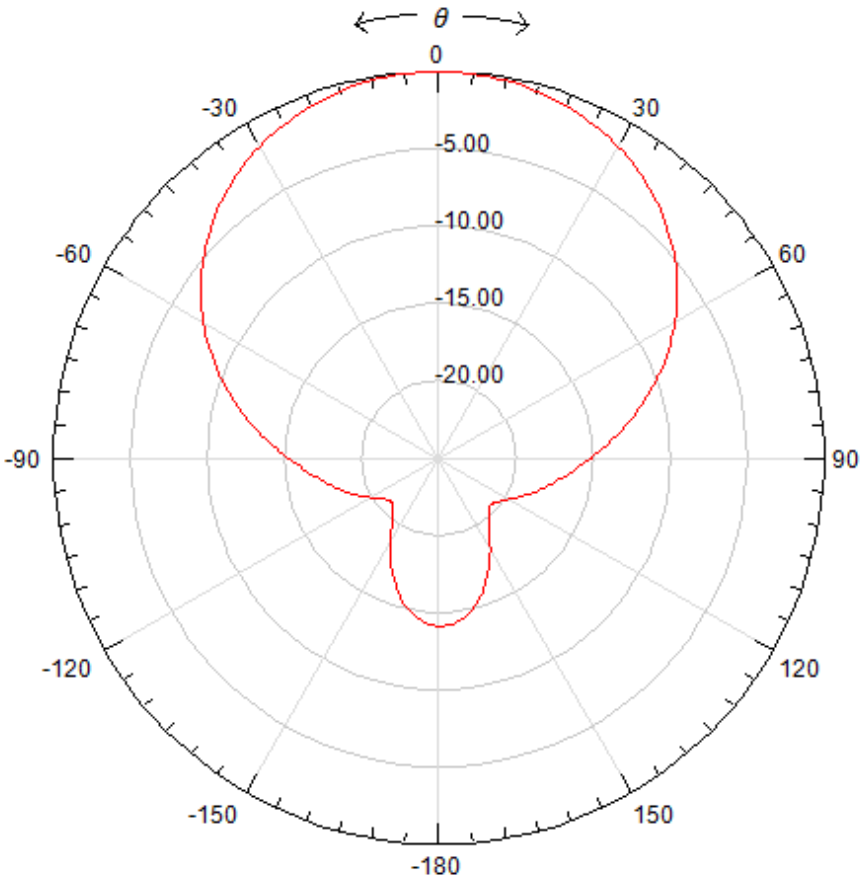

Figure 46: A polar plot of the normalized antenna gain in dB (8.25 GHz), H-plane (ϕ=90°).

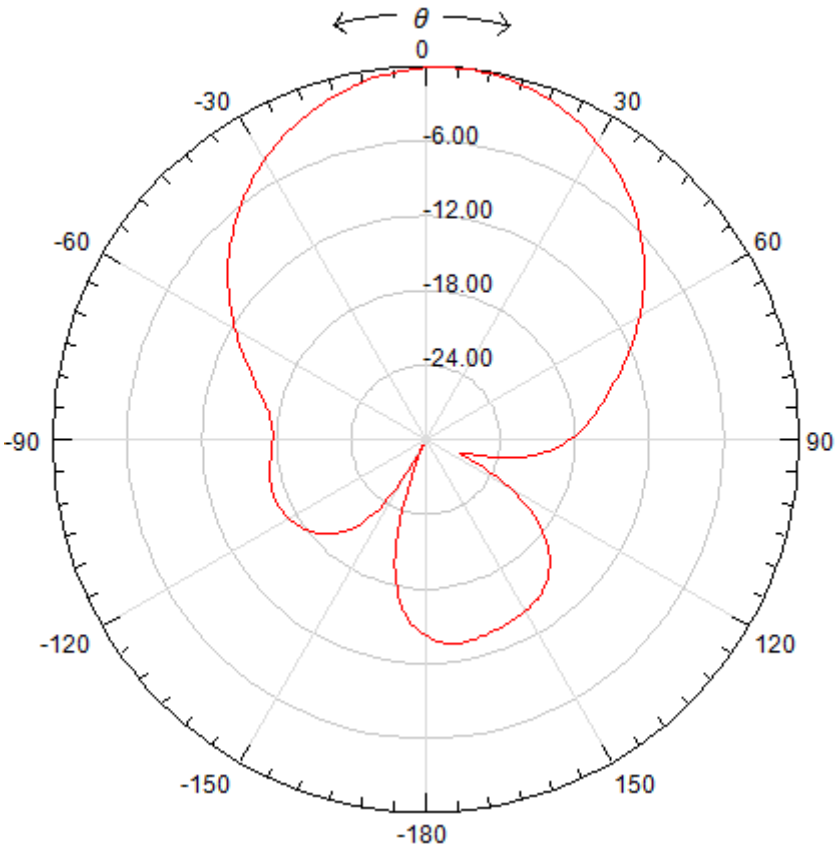

Figure 47: A polar plot of the normalized antenna gain in dB (8.25 GHz), E-plane (ϕ=0°).

The HPBW of the antenna element is determined from Figure 46 and Figure 47. It is approximately 78° in the H-plane, and in 58° in the E-plane.

5.2.2 Measured results

5.2.2.1 Input impedance

The input impedance of the antenna element was obtained using a network analyzer. The result is plotted in Figure 48. A frequency band of 7.4-8.4 GHz with a center frequency of 7.9 GHz is achieved.

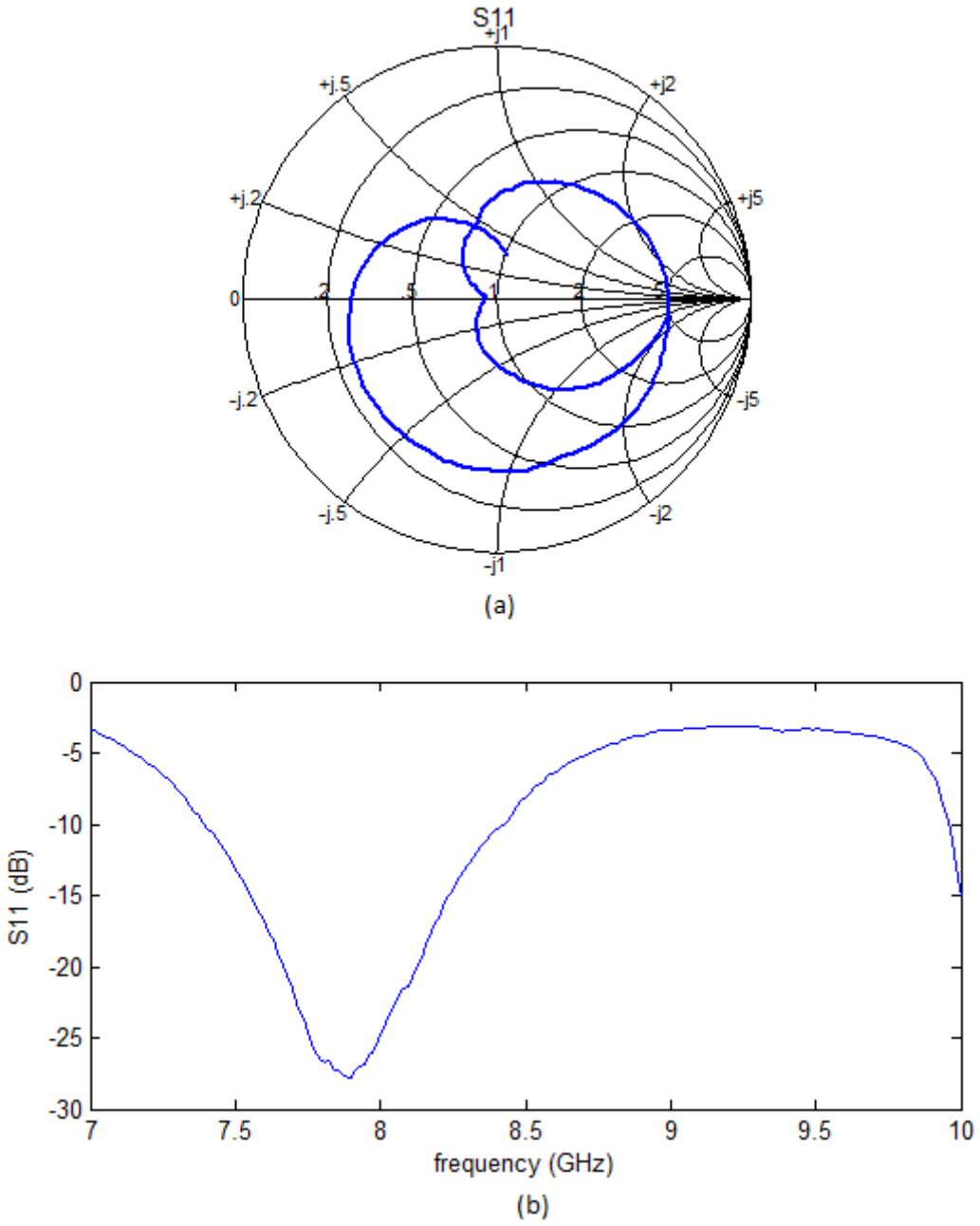

Figure 48: The measured reflection coefficient (S11) of the modified antenna element plotted in a Smith chart (a) and in dB as a function of frequency (b).

The antenna reflection coefficient has been measured for varying the distance between the two patches. The results are plotted in Figure 49 and Figure 50.

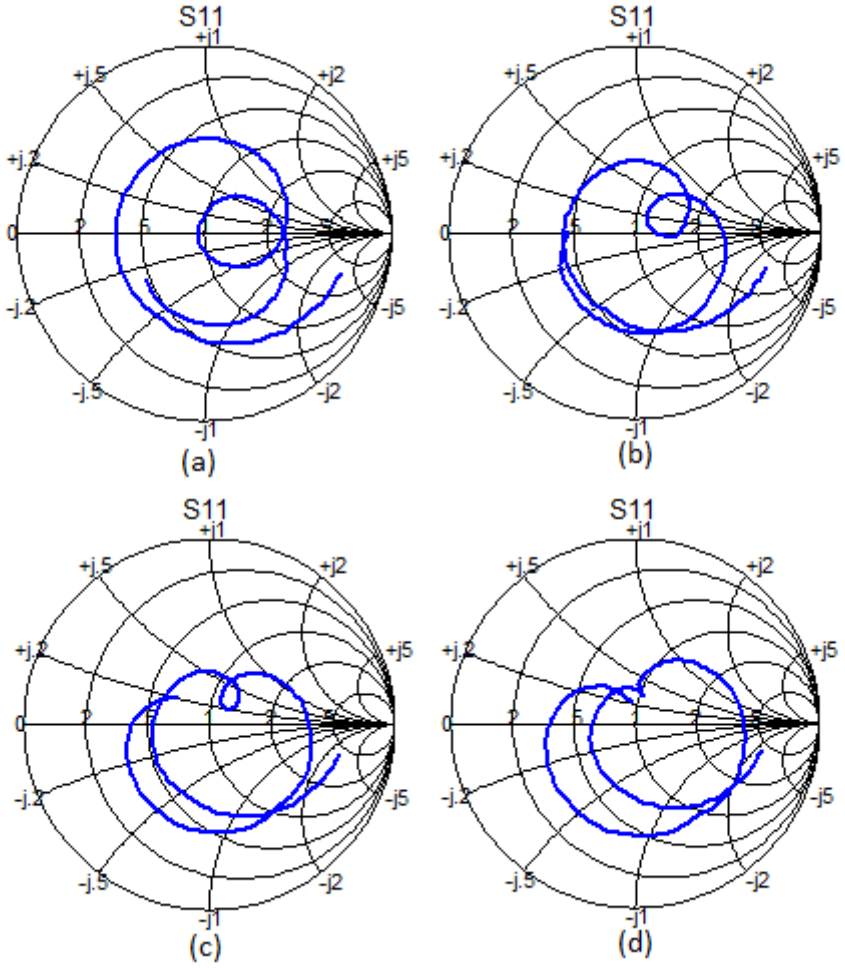

Figure 49: Reflection coefficient of the antenna element plotted in a Smith chart for different distances between the patches. (a) 1.32 mm (b) 1.65 mm (c) 2.02 mm (d) 2.2 mm

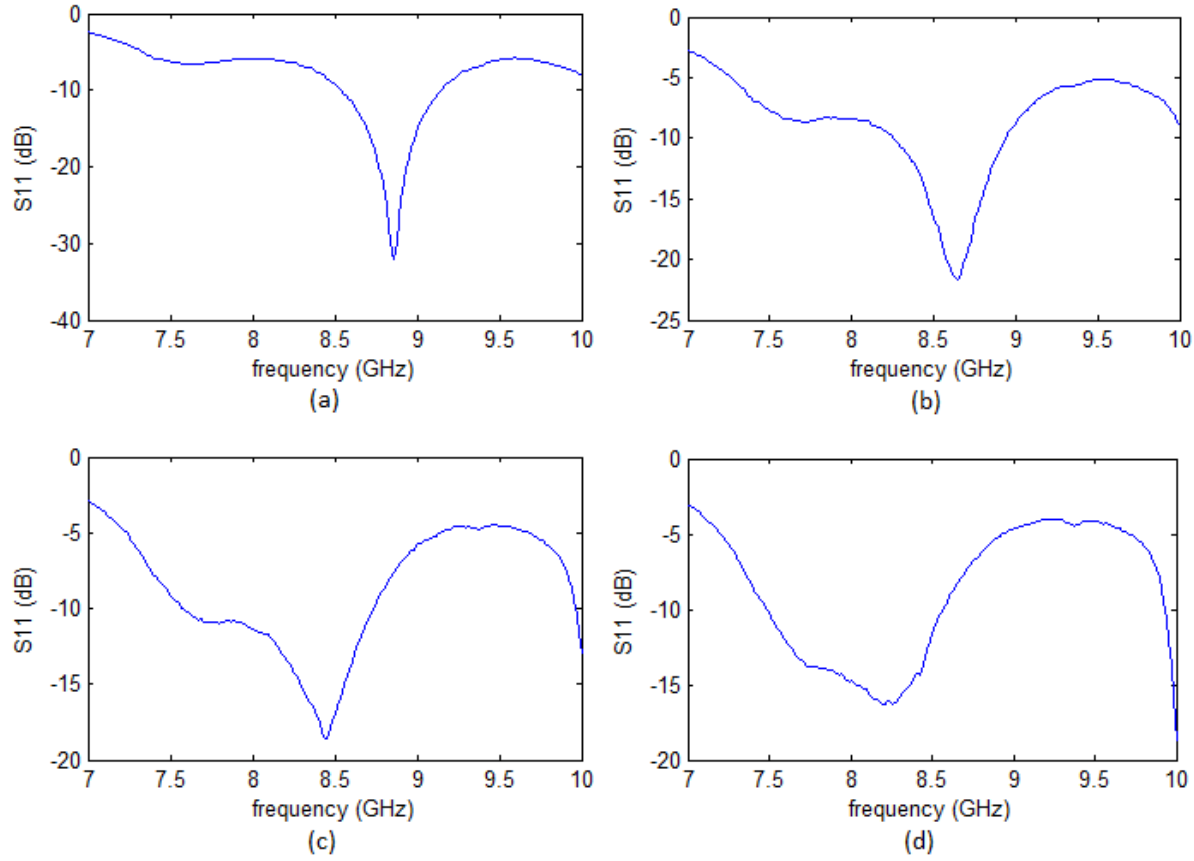

Figure 50: Reflection coefficient of the antenna element plotted in dB as a function of frequency for different distances between the patches. (a) 1.32 mm (b) 1.65 mm (c) 2.02 mm (d) 2.2 mm

Figure 49 shows that decreasing the distance between the patches makes the loop bigger, owing to a larger coupling level between the patches. This leads to the center frequency being moved up in frequency as seen in Figure 50.

5.2.2.2 Radiation pattern

Measurement of the antenna element radiation pattern was conducted at the antenna hall at NTNU. Both E-plane and H-plane patterns were measured. Additional measurements were conducted to determine the cross-polarization. The results are plotted in Figure 51 and Figure 52.

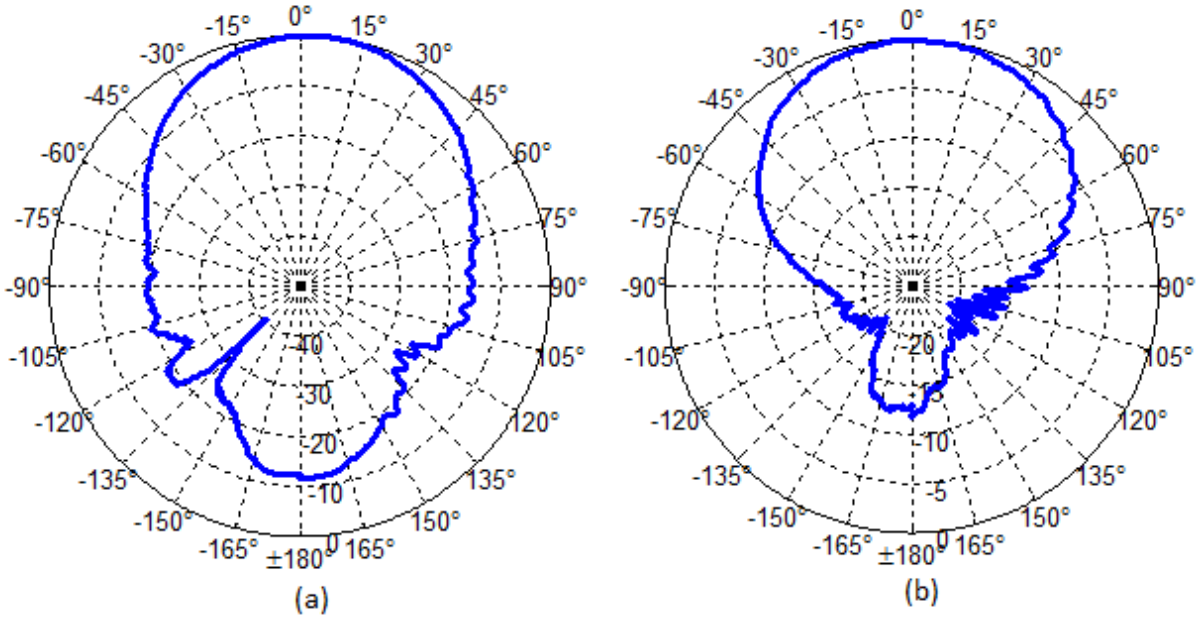

Figure 51: Radiation pattern for the modified antenna element at 8.25 GHz in normalized dB, (a) E-plane, (b) H-plane

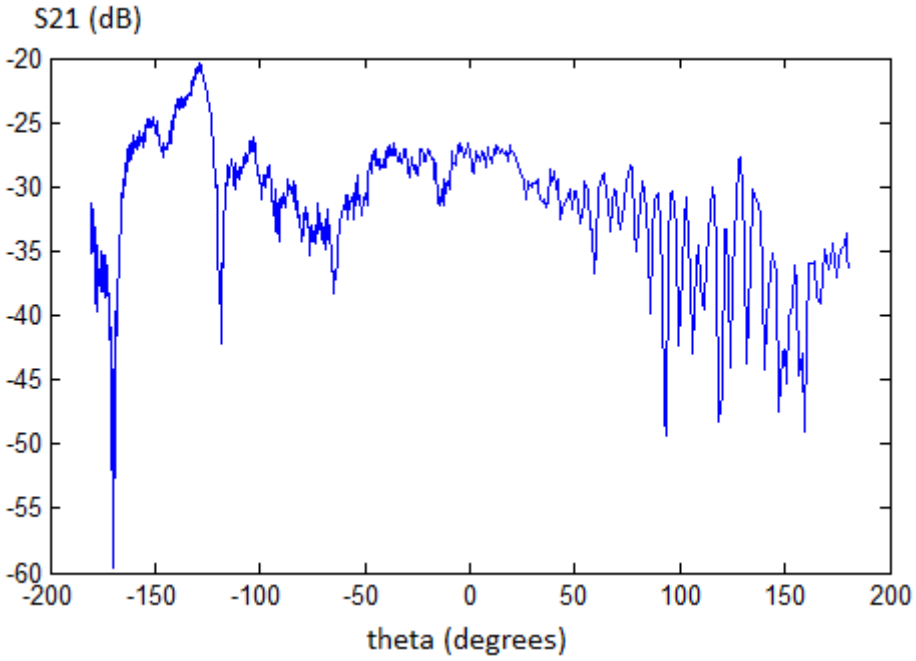

Figure 52: Cross polarization level of the modified antenna element

The measured HPBW is 55° and 84° in E-plane and H-plane, respectively. For more measured results see Appendix B.

6 Discussion

6.1 Array performance

In this project emphasis was put on achieving a large scan range. A scan range of -55° to 55° in the E-plane ($\varphi = 0°$) and -45° to 45° in the H-plane ($\varphi = 90°$) plane has been achieved. The goal was a scan range of -70° to 70° in both planes. This goal was not reached within the time limits for this thesis and more work is therefore needed. It is possible to achieve a scan range close to the goal, this is confirmed by [10]- [13]. Here scan ranges close to -70° to 70° have been achieved using similar antenna elements. Increasing the scan range is a difficult task since the input impedance is highly dependent on the scan angle due to the mutual coupling between elements.

Figure 35 shows the reflection coefficient plotted as a function of scan angle. It is seen that the reflection coefficient is close to -10 dB over a large portion of the scan range in both planes. A reflection coefficient of -10 dB is considered a match, but it will lead to large amounts of power being reflected. For an input power of 50 W, 5 W will be reflected back into the TX/RX circuits. This amount of reflected power can in worst case damage the system, and it certainly makes the system less effective. The reflection coefficient should therefore be decreased. If the reflection coefficient is decreased to -20 dB, only 0.5 watt will be reflected.

The scan range is greater in the E-plane than in the H-plane. This is a normal property for these types of arrays, as seen in [10]- [13]. A reason for this is that the level of coupling between elements differs from one plane to the other. This can be seen in Figure 42, which shows that the coupling level in the E-plane is 3.6 dB larger than in the H-plane. This means that the largest scan range is achieved in the plane which has the largest mutual coupling level. This is an unexpected result since it was expected that the plane with the lowest mutual coupling would have the largest scan range.

A correlation between large bandwidth and large scan range was suspected since [10], [11], [12] and [13] achieved large scan ranges using only antenna elements with large bandwidths. For this reason the was the bandwidth of the antenna element increased to 48% which is a significant increase compared to the bandwidth of the original antenna element. After increasing the bandwidth an increase in scan range was observed. This supported the suspicion of a relationship between bandwidth and scan range. Further investigation into this subject could be of interest to uncover if there truly is a relationship between bandwidth and scan range, and if so, how strong the relationship is.

Figure 37 shows the results using the Floquet analysis. The two propagating modes are plotted together with the reflection coefficient. The first mode represents the main beam, it is seen that a large amount of the input power is transmitted in this mode. The second mode represents the first grating lobe. It is observed that for larger scan angles more input power is

transferred to this mode. This is expected since grating lobes are more prominent at larger scan angles. It is also observed that more power is transmitted in this mode as the frequency increases. This can be understood by looking at equation (2.15). If the element spacing is kept constant and the wavelength is decreased grating lobes will occur for lower scan angles.

For arrays of patch antennas a typical problem is scan blindness. Figure 35 and Figure 37 shows that no scan blindness will occur inside the scan range.

The unit-cell Floquet port simulation setup was used to tune the antenna. To verify the results obtained with the simulation setup the Finite array DDM method was used. This method should be more accurate since an actual 8x8 array is simulated. The results of the simulation are shown in Figure 36. Large deviations between the two methods are observed. Some deviations were expected because of the infinite array assumption, especially for the edge elements. However, large deviations occur for both central and edge elements. Two possible reasons for the deviations are considered likely. The first alternative is that an 8x8 array is not large enough to be modeled accurately by an infinite array. The second alternative is the possible wrong use of one of the simulation setups. If the first alternative is the reason it means that the unit-cell Floquet port setup cannot be used to tune the antenna. This will make the design process a lot more demanding since the Finite array DDM method needs approximately three days to simulate the array. It is therefore not an effective method for array tuning. Further investigation is needed to determine if the infinite array assumption is the reason for the deviations.

A radiation efficiency of 0.96 was achieved. This is a good result, and was expected since the antenna element designed in [1] had a similar radiation efficiency. The high radiation efficiency is due to the low loss tangents in the materials used in the antenna. A high radiation efficiency is important in this application since large amounts of power will be delivered to the antenna. Assuming a 50 W input signal for each antenna element. The antenna will accept 45 W with a reflection coefficient of -10 dB. 43.2 W will then be radiated since the radiation efficiency is 0.96. This means that 115.2 W will be dissipated as heat in the antenna. This is a large amount of power gathered on a relatively small area (400x400 mm^2), so methods for transporting heat are important. This analysis has not taken into consideration the fact the radar uses pulses. This means that the average power applied to the array will be lower.

In patch antennas the main limitation on scan range is surface waves [3, p. 866]. This has been shown in [9] where decreasing the surface waves led to an increase in scan range. In [9] electromagnetic band gap (EBG) material was used to decrease the surface waves. EBG material was found to be too complex to manufacture and was therefore not used in this design. Instead a defected ground structure (DGS) was tested. Good results were achieved in the test bench. The DGS structure attenuated the surface waves by as much as 24 dB. However, implementing it in the array did not increase the scan range. Further testing showed that the ground shield severely reduced the DGS ability to suppress surface waves. It could therefore not be used in this application.

The use of an adaptive matching circuit was investigated to improve the scan range and reflection coefficient. It was concluded that an adaptive matching circuit would be too time

consuming and complex to develop. However, it is expected that it would have significantly improved both the scan range and the reflection coefficient. Another advantage is that the required accuracy on both the simulator and manufacturer would be less since the circuit will tune out errors. A big disadvantage is the added complexity caused by the circuit and the extra space it will use. However, use of an adaptive matching circuit could be necessary to reach the scan range and reflection coefficient specifications.

To summarize, the scan range is too low in both planes and the reflection coefficient should be lower to reduce the amount of reflected power. The main reason for the low scan range is the strong mutual coupling between the elements in the array, caused mostly by surface waves. To increase the scan range the bandwidth can be further extended, techniques to reduce the surface waves can be used, or an adaptive matching circuit can be developed.

6.2 Radiation

The array has a half-power beamwidth (HPBW) of 14° when scanned in broadside direction. For an uniform quadratic array the HPBW is mostly dependent on the number of elements and the element spacing. Since an 8x8 array was specified in the project description a limit on the minimum achievable HPBW was already set. The HPBW of the array factor was calculated using equation (2.33). This resulted in a HPBW of 13.6°, which is a good prediction of the simulation result. The small difference is probably caused by the effect the element pattern has on the total radiation pattern.

When scanning the main beam away from broadside the HPBW increases, as seen in Figure 38. This is due to the beam broadening of the array factor and is modeled by (2.20), (2,21) and (2.33). Beam broadening occurs since the effective length of the array decreases when the scan angle increase. The HPBW is inversely dependent on the dimension of the radiating element and it will therefore increase when the effective length is decreased. The simulated HPBW increased from 14° to 31.4° when the array was scanned from broadside to 70°, giving a large decrease in the angular resolution of the radar.

A beam broadening factor of $\cos\theta_S$ was derived in the theory chapter. It can be applied on both directivity and HPBW. The directivity decreases by a factor of $\cos\theta_S$ and the HPBW increases by a factor of $1/\cos\theta_S$ when the main beam is scanned away from broadside. This is a simple model which roughly estimates the beam broadening effect. Figure 41 shows the calculated directivity and simulated directivity as a function of scan angle. It is seen that the calculated directivity is very accurate up to about 10°, after that the differences are noticeable. At 30° the difference is about 0.7 dB, which corresponds to an error of 17%. This is an acceptable error for a simple model like this. It is concluded that the model can be used as an estimate for scan angles near broadside.

A side lobe level of -13.6 dB is achieved when the array is scanned in broadside direction. This side lobe level is high for radar applications [21, p. 544] and can lead to false detections. The side lobe level is mostly dependent on the number of elements used, so to achieve a lower

side lobe level a larger array must be used. Another solution is the use of non-uniform amplitude distributions such as a Binomial distribution or a Dolph-Tschebyscheff distribution [3, p. 325].

It is observed that when scanning the array away from broadside the side lobe level increases. This can be explained by using pattern multiplication. The side lobe level of the array factor is relatively constant for different scan angles, as seen in Table 7, but the gain of the element pattern is not constant over the entire scan range as seen in Figure 27 and Figure 39. The element pattern has largest gain at broadside. The gain then decreases to the sides, and is approximately 6 dB lower at 70°. When the main beam is scanned away from broadside it will experience more scan loss, while the side lobes will experience less scan loss since they now are located nearer broadside. This will the cause the side lobe level to increase.

Another problem experienced when scanning the array far away from broadside is that the real scan angle will deviate from the wanted scan angle. This can be seen in Figure 38 where the array is scanned to 70° but the real scan angle is only 63°. The reason for this is a combination of beam broadening and scan loss. At 70° the array factor has a calculated HPBW of 39.8°. This means that the difference in gain at 70 ° and 60° is small. So when the array factor is combined with the element factor that has a higher scan loss at 70° than at 60°, the maximum will be moved closer to 60°. How much it moves depends mostly on the difference in gain between 60° and 70°.

As shown in Figure 40 the array factor is symmetric around the x-y-plane. This means that the array factor radiates the same amount of power in the backwards direction as in the forward direction. Therefore, to achieve a low backwards radiation it is important that the element pattern cancel out as much of the radiation below the x-y-plane as possible. Low backwards radiation is achieved, especially for the broadside scan where the largest level of backwards radiation is -27 dB. For other scan angles the backwards radiation is always lower than -20 dB.

To increase the bandwidth the ASP configuration was used. This meant that the slot length was increased until the slot became resonant. Since the slot became a radiating element an increase in backwards radiation was expected. No such increase in backwards radiation was observed. This means that the ground shield and via cage successfully reduced the backwards radiation.

Figure 38(c) shows the gain pattern of the array scanned to 70°. It is observed that the grating lobes is 30 dB below the maximum. The element spacing of 16.5 mm should have reduced grating lobe level to the same level as the side lobes as seen in Figure 40(c). The much larger reduction is due to the element pattern which has a high scan loss at 90°.

Figure 39(a) shows the element radiation pattern of an antenna element placed in an infinite array environment. It has a smooth pattern with a maximum scan loss of 6 dB. Figure 39(b) shows the element radiation pattern of a central element in an 8x8 array. It is not as smooth as the first pattern, but has a relatively constant gain over the required scan range, with a maximum scan loss of approximately 6 dB. It has a larger backwards radiation than the

infinite array element because of the diffraction on the edges of the array which is not accounted for in the infinite array. Otherwise the infinite array element is a good approximation. Figure 39(c) shows the element radiation property of an edge element. The effect of the diffraction is clearly seen as the pattern is skewed. One method to reduce the effect of the edge element pattern on the total radiation is to apply amplitude taper. This is a method used to reduce side lobe levels but it will also decrease the effect of the edge element pattern on the total radiation. This is done by applying less power to the edge elements than to the central elements. The edge element pattern will be weaker and it will therefore affect the total radiation pattern less [2, p. 106].

A scan range of -70° to 70° was the goal for the array. After studying the radiation properties of the array it is clear that this goal is set to high. Even if a scan range of -70° to 70° is achieved, the radiation properties at wide scan angles are too poor to be used in a radar application. The main reasons for this is the large HPBW which leads to a very bad angular resolution, and failure to achieve the wanted scan angles. These problems can be solved by increasing the number of elements.

6.3 Mutual coupling

Figure 42(a) shows the mutual coupling levels in a 2x2 array. It is seen that the coupling between element 1 and 3 is 3.6 dB larger than the coupling between element 1 and 2. The reason for this is that surface waves will couple more strongly in the E-plane direction. Since the fundamental surface wave mode is TM and the field for a rectangular patch in E-plane direction is TM, they will couple more strongly [3, p. 858].

It was expected that the surface waves would account for a large portion of the mutual coupling, and this is confirmed by Figure 42(b). It is seen that the coupling between element 1 and 3 is reduced by 4.1 dB and the coupling between element 1 and 2 is reduced by 2.7 dB when perfect electric conductor (PEC) walls surrounds each element. This reduction is a clear indication that surface waves are large contributors to the mutual coupling.

Figure 43 shows the coupling level as a function of element spacing. As expected the mutual coupling is reduced when the element spacing increases. It was also expected that the coupling level between element 1 and 3 should decrease more slowly than the coupling level between element 1 and 2. The reason for this is that surface waves attenuates less than space waves and the coupling level between element 1 and 3 is dominated by surface waves. This expectation was not correct as seen from Figure 43. The coupling level between element 1 and 3 decreases rapidly until it reaches an element spacing of 30 mm, then it increases until it flattens out at approximately -23 dB. A possible reason for this behavior is destructive interference.

The mutual coupling level between two original antenna elements was measured, with the results plotted in Figure 44. Since the two elements are separated by an air gap no surface waves can travel between them. It is observed that the coupling level in both E-plane and H-

plane is almost identical. This confirms that the different coupling levels in the array is caused by surface waves.

6.4 Antenna element

The original antenna element was designed during the specialization project last fall [1]. Chapter 3 summarizes the design and presents measured results of both input impedance and radiation pattern. Large deviations between the measured and simulated results were experienced. The main error source was found and the antenna element was redesigned. Measured and simulated results of this modified antenna element was presented in chapter 5 and will be discussed here.

Comparing Figure 45(a) and Figure 48(a) it is seen that better compliance between measured and simulated results has been achieved. The largest difference is the absence of the loop in the measured results. This indicates that the level of coupling in the antenna is wrong. One reason for this could be that the distance between the patches is high causing a too low coupling level for the loop to be formed. The other reason could be that the distance between the feed line and lower patch is low giving a too strong coupling level, and therefore removing the loop. Thus the error source is probably either the thickness of antenna substrate 1 or 2. The accuracy of the simulator can also be a reason for the deviations.

The consequence of the lacking loop is a that the center frequency is moved approximately 350 MHz down in frequency. This can be seen in Figure 48(b). It is also observed that the -20 dB reflection coefficient frequency band is 7.67-8.13 GHz. So the antenna works very well only at the wrong frequency.

Figure 49 and Figure 50 shows the effect of different thicknesses of antenna substrate 2 on the input impedance of the antenna. It is seen that for smaller distances the loop is formed and its radius increases. The center frequency is moved up in frequency, but the reflection coefficient increases. These results confirm that the reason for the absence of the loop is wrong coupling levels in the antenna due to errors in layer thickness.

A measured HPBW of 55° and 84° is achieved in E-plane and H-plane respectively. Which is in good compliance with the simulated results (58° and 78°). Showing that HFSS can produce accurate results. Studying Figure 51(a) carefully it is seen that the pattern is skewed. The maximum gain occurs at approximately at 8°. The reason for this is the hole in the ground plane where the RF-transition is located.

Figure 52 shows that the cross polarization level is approximately -30 dB. This means that the antenna element has a high quality linear polarization.

6.5 Error sources

A significant error source is production errors. This has already been experienced as described in chapter 3. The complicated structure of the antenna makes it difficult to manufacture and therefore production errors are likely. Because of the high frequency small errors in the dimensions can lead to large deviations in antenna properties. Measurements have shown that the copper structures, such as the patches and transmission lines, are produced with good accuracy, and are therefore not expected to cause large errors. The thickness of the different substrates and bonding layers, however, are difficult to predict accurately. This leads to differences between the manufactured antenna and the antenna model, and therefore deviations between measured and simulated results. The thickness of the different substrates are important parameters since they control the coupling between the slot and the patches. Thus small errors in thickness will lead to a different input impedance. The large deviations between measured and simulated results caused by production errors are a serious problem, which makes it difficult to tune the antenna using HFSS.

Production errors will typically move the center frequency of the antenna, either up or down in frequency. A possible solution is therefore to increase the bandwidth of the antenna. This should make the antenna more robust against production errors since an acceptable reflection coefficient would be achieved even if the center frequency is moved. Another solution is an adaptive matching circuit. This will significantly relax the matching requirements since a circuit automatically will match the antenna. The circuit will therefore adjust for production errors.

Another error source is the infinite array assumption used when the array was tuned. It was expected that an 8x8 array could be modeled as an infinite array with only small losses in accuracy. The simulations however, indicated that this might not be the case.

6.6 Future work

The ultimate goal is to produce and perform measurements on the produced array. However, first the array needs to be completely finalized. The scan range of the antenna needs to be improved, and it is important that the reflection coefficient is decreased over the entire scan range. A -20 dB reflection coefficient should be the goal. This will reduce the power reflected back at the power amplifier to an acceptable level.

Before the array can be produced the deviations between the measured and simulated results of the antenna element have to be reduced. This is important to achieve expected properties of the produced array.

A large amount of power is planned to be applied to the array. Some of this power will be dissipated as heat and therefore an increase in the antennas temperature is expected. It is important to determine how high the temperature increases will be and what effects it will have on the antenna. A rise in temperature will expand the antenna materials. This will lead to

deviations in the thickness of the layers, which again leads to deviations in the input impedance. It could be necessary to tune the antenna at the expected work temperature.

Another consequence of high input power is the possibility of electric breakdown inside the antenna. Because of short distances between the conductor and ground it is a possibility that the large electric fields can lead to electric breakdown. This means that current will travel from the conductor to the ground plane through the substrate. This is a detrimental effect that has to be investigated further.

A short section on adaptive matching can be found in chapter four. This is an interesting topic that deserves further work. An adaptive matching circuit would increase the scan range, lower the reflection coefficient of the array, and make the design more robust against production errors.

One of the reasons that low backwards radiation is important is the effect it can have on the electronic components placed behind the array. The backwards radiation is lower than -20 dB. More work is needed to ensure that this is low enough for the electronic components to avoid damage.

7 Conclusion

An 8x8 array antenna has been designed using resonant aperture stacked patch (APS) antennas as elements. It covers the required frequency band of 8-8.5 GHz, a linear polarization is achieved and the backwards radiation level is below -20 dB.

HFSS was used to design and simulate the array. Both classical array theory and Floquet analysis was used in the analysis of the array. Even though the two methods have completely different approaches identical expressions for the maximum element spacing was derived.

A scan range of -55° to 55° in the E-plane and -45° to 45° in the H-plane was achieved. The goal of a scan range of -70° to 70° in both planes was therefore not met. The main reason for this is the large mutual coupling in the array mostly owing to surface waves. Methods to increase the scan range, such as electromagnetic bandgap (EBG) materials, defected ground structures (DGS), and adaptive matching circuits were investigated. Both EBG materials and DGS increase the scan range by suppressing surface waves. EBG was too complicated to manufacture and was discarded. DGS showed promising test results, but failed to suppress the surface waves when implemented in the array. This was due to the ground shield. The development of an adaptive matching circuit was deemed too time consuming and complicated for this project. However, an adaptive matching circuit will significantly improve the array performance. If the circuit is made simple and small enough it is a possible solution to achieve a reflection coefficient lower than -20 dB over the entire scan range.

A reflection coefficient just below -10 dB have been achieved over the scan range. This result should be lower considering that the power amplifier can deliver 50 W to the input terminal of the antenna element. Almost 5 W will then be reflected back into the circuit. This could possibly damage the system. A reflection coefficient of -20 dB or lower over the entire scan range will lead to only 0.5 W being reflected back.

The array has a half power beam width (HPBW) of 14° at broadside. The HPBW increases as the main beam is scanned away from broadside. This is a fundamental effect called beam broadening and can be explained by the fact that the effective length of the array seen from the observation point decreases when the main beam is scanned away from broadside. The HPBW at a scan angle of 70° is 31.4°. This severely reduces the angular resolution of the array. Other unwanted effects occurring when scanning the main beam are an increase in side lobe level and wrong realized scan angles. The side lobe level increases from -13.6 dB at broadside to -8.7 dB at a scan angle of 70°. Considering these effects it can be concluded that a scan range of -70° to 70° is too large for this array due to the poor radiation performance at large scan angles. One solution for reducing these effects is to increase the number of elements. Individual weighting of the antenna channels will also reduce the side lobe level.

A radiation efficiency of 0.96 is achieved. This is a good result and is caused by the low loss tangent in the substrates being used. A high radiation efficiency is important due to the large

amount of power delivered to the antenna. Assuming a reflection coefficient of -10 dB and 50 W being delivered to each antenna element, 115.2 W will then be dissipated as heat. This will lead to a high antenna temperature. More work need to be done to determine the antenna behavior at high temperatures.

Most of the simulation results presented in this report were obtained using an unit-cell Floquet port simulation setup in HFSS. The unit-cell Floquet port simulation setup produces results for an infinite array. It was expected that an 8x8 array is a close enough approximation of an infinite array. Simulations done at the end of the project indicated that this assumption does not hold and that results obtained using the unit-cell Floquet port simulation setup can be wrong. Further investigation is necessary before a conclusion can be made.

An antenna element was produced and measured. Deviations between measured and simulated input impedance were found. The reason is inaccuracies in the simulations and production errors. The measured frequency band is 7.4-8.4 GHz where the center frequency is at 7.9 GHz. This means that the center frequency is moved approximately 350 MHz down in frequency. These deviations causes severe problems and the array cannot be produced until the deviations are made smaller.

Good compliance between simulated and measured results of the radiation pattern was achieved. The measured HPBW of the antenna element is 55° and 84° in the E-plane and H-plane respectively, which is very similar to the simulated result.

To summarize, the array is still not ready for production. First the scan range and reflection coefficient need to be improved. Then the deviations in simulated and measured results need to be reduced, and topics such as the thermal properties of the array need to be investigated.

8 Bibliography

[1] F. Gulbrandsen, "Design and analysis of antenna element for a phased-steered X-band radar antenna," Trondheim, 2012.

[2] A. K. Bhattacharyya, Phased Array Antennas, Wiley, 2006.

[3] C. A. Balanis, Antenna Theory, third edition, Wiley, 2005.

[4] D. K. Cheng, Field and Wave Electromagnetics, second edition, Addison Wesley, 1989.

[5] D. M. Pozar, Microwave Engineering, fourth edition, Wiley, 2012.

[6] R. B. Waterhouse, "Stacked Patches Using High and Low Dielectric Constant Material Combinations," *IEEE Transactions on Antennas and Propagation,* vol. 47, no. 12, pp. 1767-1771, December 1999.

[7] R. B. Waterhouse, D. M. Pozar and S. D. Targonski, "Design of Wide-Band Aperture-Stacked Patch Microstrip Antennas," *IEEE Transactions on Antennas and Propagation,* vol. 46, no. 9, pp. 1245-1251, 1998.

[8] D. M. Pozar, "A Review of Aperture Coupled Microstrip Antennas: History, Operation, Development and Applications," 1996.

[9] C. Fulton and W. Chapell, "Low-Cost, Panelized Digital Array Radar Antennas," in *COMCAS. IEEE*, 2008.

[10] L. Infante, S. Mosca and M. Teglia, "Low-Profile Wide-Band Wide-Angle-Scan Antenna Array Element," in *6th European Conference on Antennas and Propagation*, 2011.

[11] R. Erickson, R. Gunnarsson, T. Martin, L. G. Huss, L. Petterson, P. Andersson and Ouacha, "Wideband and Wide Scan Phased Array Microstrip Patch Antennas for Small Platforms".

[12] L. G. Huss, R. Gunnarsson, P. Anderson and R. Erickson, "A Wideband, Wide Angle Scan, Microstrip Array Antenna Element".

[13] D. Tallini, A. Galli, M. Ciattaglia, L. Infante, A. De Luca and M. Cicolani, "A New Low-Profile Wide-Scan Phased Array for UWB Applications".

[14] Fu, Y. Yunqi and Naichang, "Elimination of Scan Blindness in Phased Array of Microstrip Patches Using Electromagnetic Bandgap Materials," *IEEE Antennas and Wireless Propagation Letters ,* vol. 3, pp. 63-65, 2004.

[15] M. Salehi and A. Tavakoli, "A novel low mutual coupling microstrip antenna array design using defected ground structure," *International Journal of Electronics and Communications*, pp. 718-723, 2006.

[16] S. Xiao, M. C. Tang, Y. Y. Bai, S. Gao and B. Wang, "Mutual coupling suppression in microstrip array using defected ground structure," *IET Microwaves, Antennas & Propagation*, vol. 5, no. 12, pp. 1488-1494, 2012.

[17] R. B. Waterhouse, "A Novel Technique for Increasing the Scanning Range of Infinite Arrays of Microstrip Patches," *IEEE Microwave and Guided Wave Letters*, vol. 3, no. 12, pp. 450-452, 1993.

[18] Smith, C. Natanael J, V. Chi-Chih and J. L, "An Improved Topology for Adaptive Agile Impedance Tuners," *IEEE Antennas and Wireless Propagation Letters*, vol. 12, pp. 92-95, 2013.

[19] Meng, v. B. Fanfan, M. Andre and Reza, "A Mismatch Detector for Adaptive Antenna Impedance Matching," in *Proceedings of the 36th European Microwave Conference*, Manchester, 2006.

[20] Ida, T. Ichirou, T. Jun-ichi and O. Y. Takeshi, "An Adaptive Impedance Matching System and its Application to Mobile Antennas," IEEE, 2004.

[21] M. I. Skolnik, Introduction to Radar Systems third edition, McGraw-Hill, 2001.

[22] V. Rathi, G. Kumar and K. P. Ray, "Improved Coupling for Aperture Coupled Microstrip Antennas," *IEEE Transactions on Antennas and Propagation*, vol. 44, no. 8, pp. 1196-1198, 1996.

[23] D. M. Pozar and S. D. Targonski, "Improved Coupling for Aperture Coupled Microstrip Antennas," *Electronics Letters*, vol. 27, no. 13, pp. 1129-1131, 1991.

[24] I. J. Bahl and K. C. Gupta, "Average power-handling capability of microstrip lines," *Microwave, Optics and Acoustics*, vol. 3, no. 1, pp. 1-4, 1979.

Appendix A: Additional theory

A.1 Patch antennas

A general patch antenna is shown in Figure 53. It consists of a layer of dielectric substrate where a copper patch is etched on the top, and a ground plane is etched at the bottom. The patch is the radiating element and can have any shape. The size of the patch, thickness and dielectric constant of the substrate and feed type are parameters that determine the properties of the antenna.

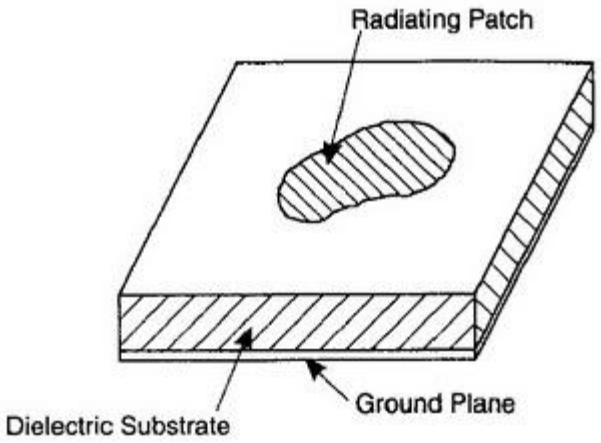

Figure 53: Patch antenna

Feeding methods

[3, pp. 813-815]

There are several different ways to feed a patch antenna; microstrip line feed, probe feed, proximity feed and aperture coupled feed. A short presentation of each is given below.

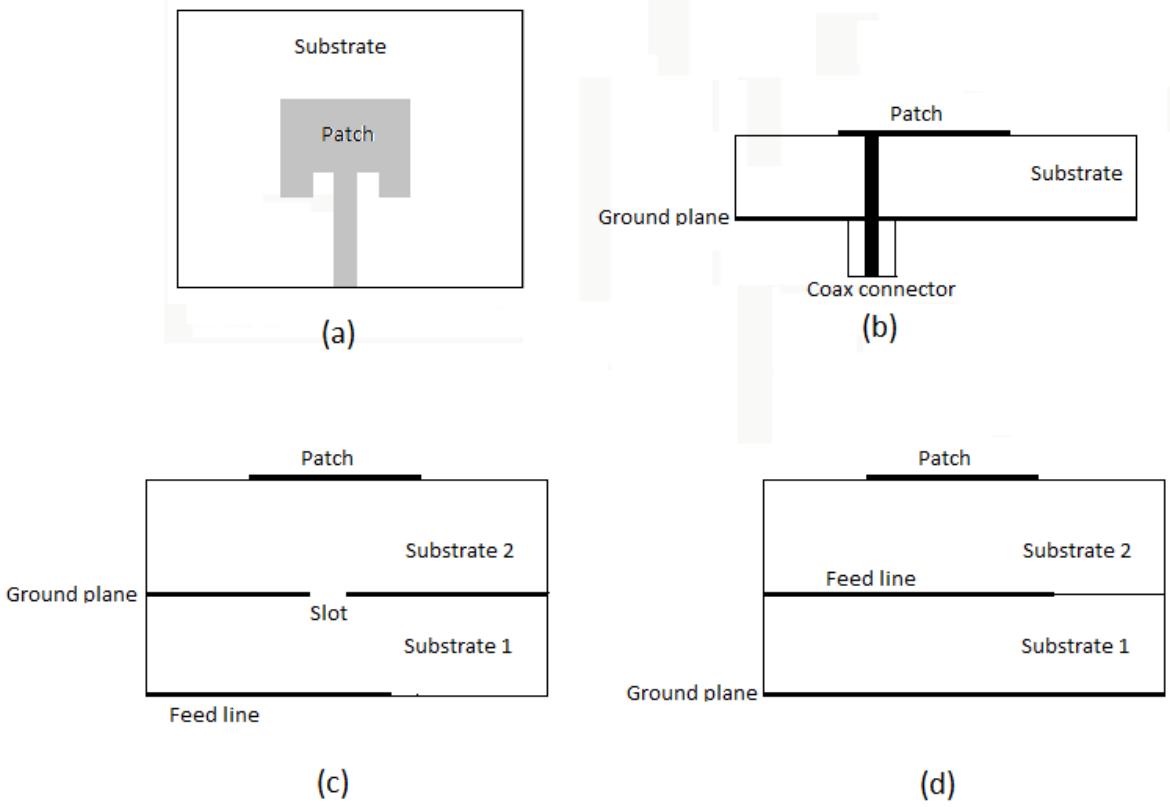

Figure 54: (a) Microstrip line feed (b) Probe feed (c) Aperture-coupled feed (d) Proximity feed

Microstrip line feed: The microstrip line feed is shown in Figure 54 (a). The patch is fed by a microstrip line connected to one of its sides. Matching is done by moving the contact point in to the patch. It is easy to model and easy to produce. The feed line will radiate and disturb the radiation pattern of the patch, this is called spurious feed radiation. Because of asymmetric structure, high levels of cross polarizing will occur. The bandwidth is rather limited, typically 2-5%.

Probe feed: The probe feed is shown in Figure 54 (b). The inner conductor of a coaxial cable is brought up through a hole in the ground plane and is connected to the patch, the outer connector is connected to the ground plane. Good matching is achieved by moving the point of contact to a place that gives the wanted input impedance. Since most of the feed is behind the ground plane and the probe is behind the patch, the spurious feed radiation is significantly reduced compared to the microstrip line feed. The probe feed suffers from low bandwidth and the asymmetric structure that will lead to cross polarization.

Aperture-coupled feed: The aperture-coupled feed is shown in Figure 54 (c). The patch and feed line are separated by a ground plane, so there is no physical contact between the feed line and the patch. The fields are coupled from the feed line through a slot in the ground plane to the patch. Since the feed is placed behind the ground plane the spurious feed radiation is low.

The structure is symmetric, this leads to low cross polarization. It is more complex to produce than microstrip line feed and probe feed, but it has more parameters to tune the radiation characteristics and input impedance. It has a low bandwidth, but several well documented techniques have been developed that increases the bandwidth [7].

Proximity feed: The proximity feed is shown in Figure 54 (d). Similar to aperture-coupled feed the proximity feed has no physical contact between the feed line and the patch. Here, the feed line is placed directly under the patch, so the fields couples straight from the feed to the patch. This configuration has the largest bandwidth of the alternatives presented here. The spurious feed radiation will affect the forward radiation pattern more than the aperture-coupled feed because no ground plane separates the feed from the radiating element. It is a symmetric structure giving low cross polarization.

The feed method is chosen depending on the application. The proximity feed has the largest bandwidth, so for applications where high bandwidth is needed, and no additional bandwidth increasing techniques is used, the proximity feed is the best option. For large arrays the probe feed and the aperture-coupled patch has an advantage since both enables feeding from the back. This will simplify array design and phase-steering of the array. Microstrip line feed is easy to match and the design is less complicated than the other options. This subject is further discussed in the design chapter.

Techniques to increase bandwidth

Patch antennas have a rather low bandwidth so in this section three techniques for increasing the bandwidth of an aperture-coupled patch antenna are presented.

Single patch resonant aperture: This configuration is a standard aperture-coupled patch antenna as shown in Figure 54 (c). The size of the slot is increased to the point where it becomes resonant, this means that the slot becomes a radiating element. The resonance of the slot is coupled to the resonance of the patch, this is called mutual resonance. This will result in a wider bandwidth as seen in Figure 55 (a). Here the reflection coefficient of the antenna is plotted over different frequencies in a Smith chart. The tight loop around the center is the result of the mutual resonance of the slot and patch. This configuration has been shown to obtain a 1.5:1 voltage standing wave ratio (VSWR) bandwidth of over 20% [7]. A 1.5:1 VSWR is equivalent to a -14 dB reflection coefficient. The resonant aperture is an effective radiating element and will increase the backwards radiation of the antenna.

Aperture coupled stacked patch (ACSP): In this configuration the slot is sized so that it is not resonant, instead a second patch is placed at a height directly over the first patch, this can be seen in Figure 56. The resonance of the lower patch couples to the resonance of the upper patch. This will lead to the same result as the first alternative as shown in Figure 55 (b). The tight loop in the Smith chart is formed because of the mutual resonances between the lower and upper patch. The 1.5:1 VSWR bandwidth of this antenna can also be over 20% [7].

Resonant aperture stacked patch (ASP): This configuration combines the two methods above to give the antenna a 1.5:1 VSWR bandwidth that can exceed 40% [7]. The resonance

of the slot is coupled to the resonance of the lower patch, then the resonances of the lower and upper patch are also coupled together, resulting in two tight loops in the Smith chart, see Figure 55 (c). As for the first alternative the ASP have a large backwards radiation due to the resonant aperture.

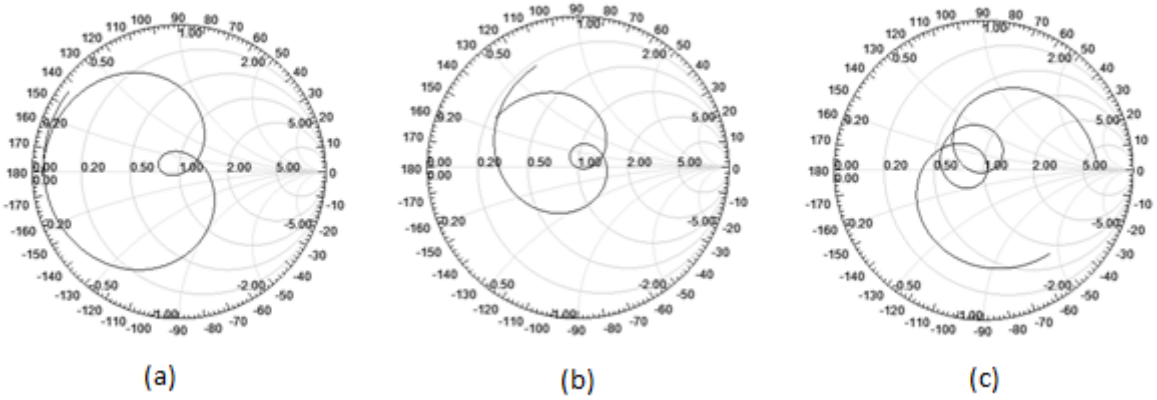

Figure 55: Reflection coefficient plotted in a Smith chart for (a) Resonant aperture (b) The ACSP (c) the ASP

To achieve a high bandwidth the reflection coefficient of the antenna, as plotted in Figure 55, needs to be as close as possible to the center of the Smith chart over as many frequencies as possible. Because of the tight loops formed as a consequence of the mutual resonances, the reflection coefficient is closer to the center of the Smith chart over a lager range of frequencies, and thus increases the bandwidth.

Aperture-coupled stacked patch (ACSP)

This antenna uses the aperture-coupled feed configuration as the feed mechanism and stacked patches to increase the bandwidth. The ACSP is a complicated structure and no mathematical model that can be used in the design has been found. However, some guidelines have been developed [7] [8]. A brief summary of these guidelines and other aspects of the ACSP are presented in this section.

Figure 56 shows the ACSP antenna. It consists of a feed substrate with a microstrip line etched on the bottom and ground plane on the top. A rectangular slot in the ground plane is placed directly over the feed line. The stub, which is the part of the feed line that is under the slot, is used to match the antenna [7]. Two antenna substrates are placed on top of each other over the feed substrate, with a rectangular patch etched on top of each substrate.

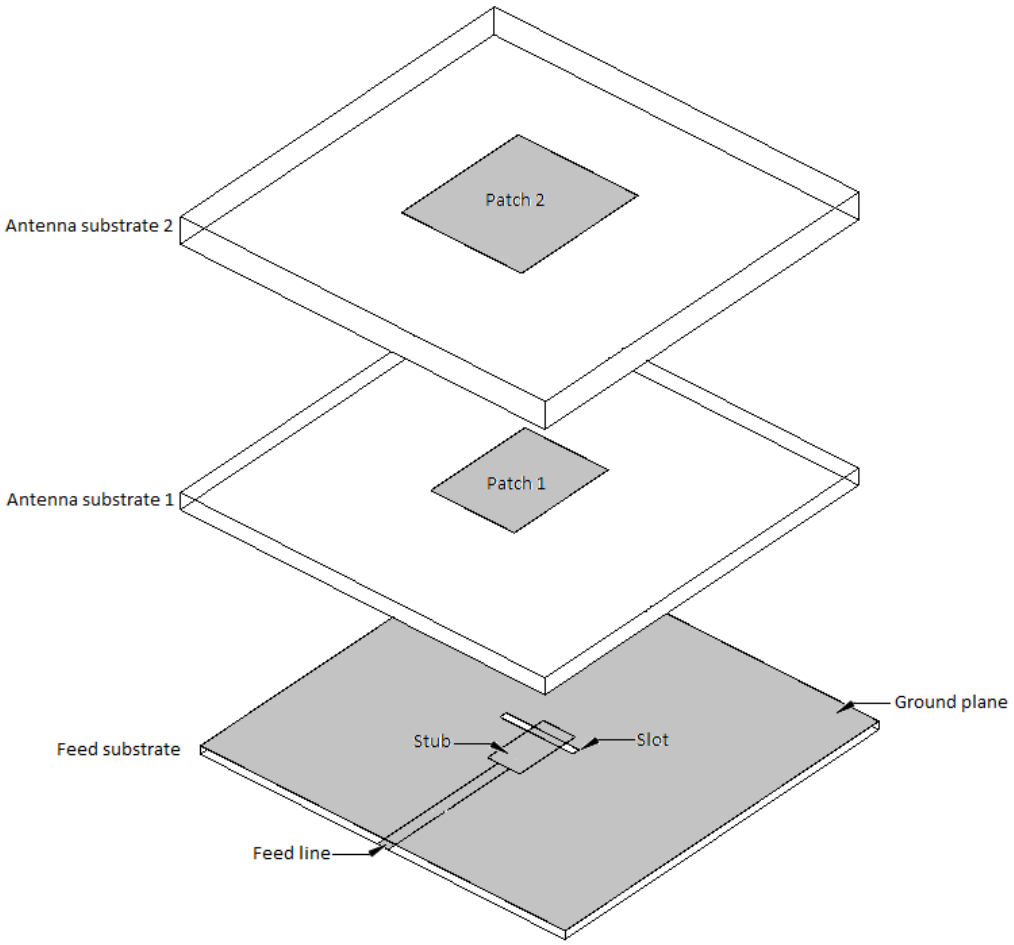

Figure 56: The Aperture Coupled Stacked Patch (ACSP)

When a signal is put on the feed the fields will couple from the feed line through the slot and to the first patch. This is a strong coupling and is the reason for the large loop in the Smith chart in Figure 57. Then a weaker coupling between the two patches resonances occur. This results in the small loop in the Smith chart in Figure 57.

This antenna has been shown to have a 1.5:1 VSWR bandwidth of over 20 % [7] and achieve a gain of 8-9 dB over a frequency band of 3.1-3.5 GHz [9].

One advantage of the ACSP is that multiple parameters can be used to tune the antenna. It makes the design complicated but it allows for good control over the input impedance and radiation characteristics. A description of these parameters and effects are found in [7]- [9] and are summarized below.

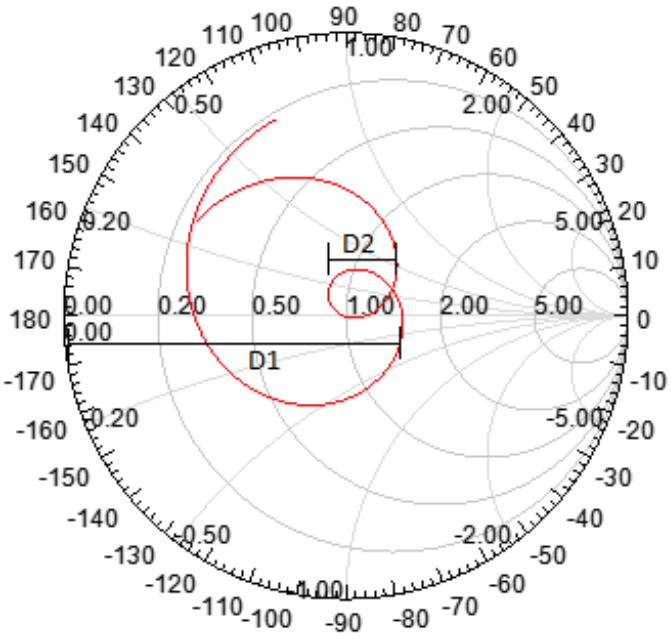

Figure 57: Reflection coefficient of the ACSP plotted in a Smith chart

Patch length

The patch length controls the resonance frequency of the patch. For stacked antennas the length also controls the level of coupling between patches and will therefore affect the diameter of the little loop (D2) .

Patch width

The patch width affects the resonant resistance of the antenna, where a wider patch gives lower resistance.

Slot length

The slot length controls the level of coupling between the feed and the lower patch. A longer slot means higher coupling, which increases the radius of the large loop (D1). If made too big relative to the wavelength the slot becomes resonant and will radiate. This can be used to increase the bandwidth, as in the ASP antenna, but it will degrade the front-to-back ratio, due to backward radiation.

Slot width

The sloth width affects the coupling level in a lesser extent than the slot length, and is therefore held at 1/10 of the slot length.

Feed line width

The width determines the characteristic impedance of the feed line. Additionally, it controls to a certain degree the coupling between the feed and patch. Thinner feed gives stronger coupling.

Stub length

The stub length, which is the length of the stub taken from the center of the slot and out controls the reactance of the slot. Thus it is an effective parameter to tune when matching the antenna. A longer stub moves the impedance locus in the inductive direction in the Smith chart and a shorter stub in the capacitive direction. It is usually around $\lambda_g/4$, where λ_g is the wavelength in the substrate and is given as [5, p. 20]

$$\lambda_g = \frac{2\pi}{k} = \frac{2\pi}{\omega\sqrt{\mu\epsilon}} = \frac{\lambda_0}{\sqrt{\mu_r\epsilon_r}} \tag{A.1}$$

where λ_0 is the free space wavelength, μ and ϵ is the magnetic permeability and electric permittivity respectively, and ω is the angular frequency. The last step can be made since $c = 1/\sqrt{\mu_0\epsilon_0}$ [4, p. 355].

Stub width

The stub width is used to match the impedance of the antenna since the width of the stub controls the coupling level. A wider stub decreases the coupling level.

Feed substrate thickness

The thickness of the substrate will together with the feed line width and the dielectric constant determine the characteristic impedance of the feed line. Thicker substrate gives a wider feed line. Thin feed substrate gives less spurious feed radiation but greater loss.

Feed substrate dielectric constant

The dielectric constant is chosen so that the wanted feed line characteristics are obtained.

Antenna substrate thickness

The thickness is primarily used to control the coupling level between the different elements in the antenna. The thicker the substrate, the more loosely coupled will the elements be. The thickness of antenna substrate 1 from Figure 56 affects D1 and the thickness of antenna substrate 2 affects D2. A thicker substrate will increase the bandwidth but also increase surface wave loss.

Antenna substrate dielectric constant

The dielectric constant affects bandwidth and efficiency. A low dielectric constant gives less surface waves and increases the bandwidth.

Slot

For an aperture coupled patch antenna the size and shape of the slot have a large effect on the antenna properties. As mentioned earlier, the size of the slot controls the level of coupling and it can also be used to increase the bandwidth if the slot is made resonant [7]. The shape of the

slot will also affect the coupling, since different shapes have different levels of coupling for a given area.

When matching an aperture coupled patch antenna it is normal to adjust the size of the slot. If the slot length approaches $\lambda_g/2$ during the matching process, the slot becomes resonant. The slot is then a radiating element and this will increase the backward radiation of the antenna. This may be unwanted in many applications. Several different shapes have therefore been investigated to find more effective apertures with regard to larger coupling than the rectangular slot. Two such works are [22] and [23]. In [22] three different shapes; bowtie, H-shape and hourglass are compared to the rectangular slot. All have superior levels of coupling compared to the rectangular slot.

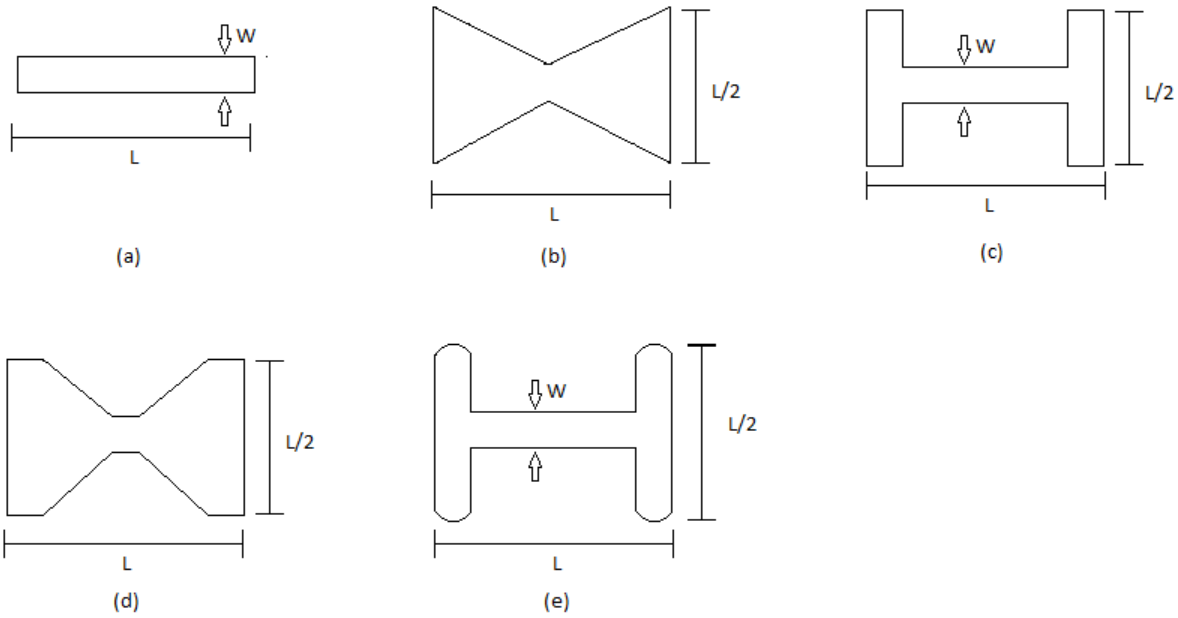

Figure 58: (a) Rectangular slot. (b) Bowtie slot. (C) H-shape slot. (d) Hourglass slot. (e) Dogbone slot

In [23] the dogbone slot, as shown in Figure 58(e), is presented. It is concluded that the dogbone achieves over three times the level of coupling compared to a rectangular slot of the same size. Since the H-shape and dogbone are very similar, it is reasonable to assume they achieve approximately the same level of coupling.

The fields of the rectangular slot decrease rapidly when moving away from the center and have to be zero at the ends. The fields for the other slots is also zero at the ends but because of the different shapes a less rapid decrease in field strength occurs when moving away from the center [23]. This leads to a more uniform field and an increased level of coupling.

Hi-Lo dielectric constant configuration

When designing a stacked patch antenna, different combinations of materials can be used to give the antenna different properties. One such combination is the Hi-Lo dielectric constant configuration presented in [6]. Here, the lower patch is etched on a substrate with a high dielectric constant and the upper patch is etched on a substrate with lower dielectric constant. The Hi-Lo configuration is shown to increase the bandwidth and surface wave efficiency, it also reduces cross polarization [6]. Since a thick substrate, specifically the upper layer, increases the bandwidth it is necessary that the upper layer have a low dielectric constant to minimize surface waves.

A.2 Antenna parameters

This section presents a brief description of important antenna parameters used in the project. First the input impedance and bandwidth are described, then the antenna efficiency and at last the definition of antenna gain is presented.

Input impedance

[3, pp. 80-85]

The input impedance of an antenna is the impedance seen looking into the input terminals of the antenna. It is computed as the ratio of the voltage to the current at the input terminal. From Figure 59, which shows an equivalent circuit of the antenna. the impedance can be written as

$$Z_A = R_A + jX_A \tag{A.2}$$

where

$$R_A = R_L + R_{rad} \tag{A.3}$$

R_L models the loss in the antenna and R_{rad} is the radiation resistance of the antenna. R_{rad} indicates how much power is radiated.

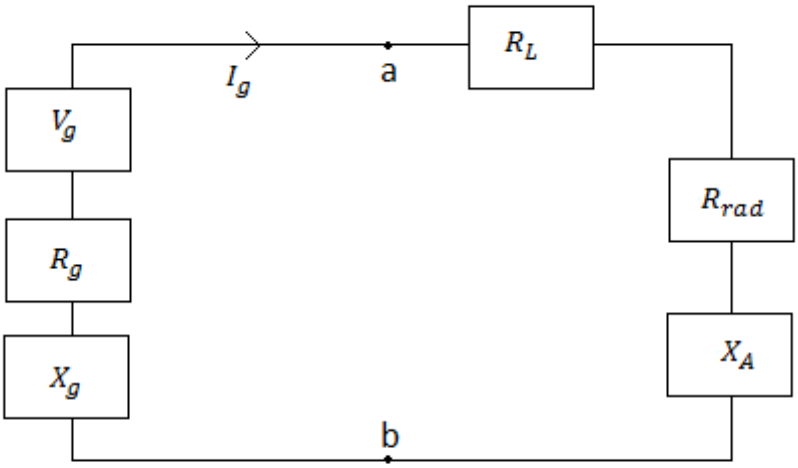

Figure 59: Equivalent circuit of an antenna

V_g is the generator connected to the terminals, and R_g and X_g represents the internal impedance of the generator, where R_g is the resistance and X_g is the reactance. For a patch antenna R_{rad} and R_L are dependent on the geometry, i.e. shape and size of the patch, and the

electrical properties of the material. The input impedance is dependent on frequency, and X_A models the dependency. An antenna is resonant when $X_A = 0$.

Bandwidth

[3, p. 70]

The bandwidth of an antenna is the frequency range where one specified antenna property is achieved. A common bandwidth specification, specifically for patch antennas, is the -10 dB reflection coefficient bandwidth. It gives the width of the frequency band where the reflection coefficient is lower than -10 dB. Other parameters can be used to specify the bandwidth, for example gain, radiation pattern and radiation efficiency. If not anything else is specified the -10 dB reflection coefficient bandwidth is implied in this report.

The bandwidth can be given as a ratio of the lowest and the highest frequency, or as a percentage of the center frequency. The latter is used in this report.

Antenna efficiency

[3, pp. 64-65]

The total antenna efficiency e_0 can be divided into three efficiencies; conduction efficiency e_c, dielectric efficiency e_d and reflection efficiency e_r. e_r can be written as a function of the reflection coefficient Γ. The total efficiency is then given by

$$e_0 = e_c e_d e_r \; = \; e_{cd}(1 - |\Gamma|^2) \tag{A.4}$$

Since conduction and dielectric efficiency are hard to compute and measure separately they are often combined into one efficiency e_{cd}. This efficiency describes the internal losses in the antenna and is the same as the radiation efficiency which is defined as

$$e_{rad} = \frac{P_{rad}}{P_{acc}} \tag{A.5}$$

where P_{rad} is the radiated power and P_{acc} is the accepted power. The radiation efficiency describes how effective an antenna is at turning the accepted power into radiated power. A low radiation efficiency means that a lot of the power accepted is lost in the antenna and is dissipated as heat.

Gain

[3, pp. 65-68]

The gain is a very useful antenna parameter. It takes into account both the radiation efficiency and the directivity. High gain means that the antenna is efficient and that the antenna directs a lot of power in that direction. Gain is defined as [3, p. 66]

$$G(\theta,\varphi) = 4\pi \frac{U(\theta,\varphi)}{P_{acc}} \tag{A.6}$$

where $U(\theta,\varphi)$ is the radiation intensity and P_{acc} is the accepted power. The radiation intensity in a given direction is given as [3, p. 40]

$$U = r^2 W_{rad} \tag{A.7}$$

where W_{rad} is the radiation density and can be found from the time average Poynting vector.

Combining (A.5) and (A.6) gives

$$G(\theta,\varphi) = 4\pi e_{cd} \frac{U(\theta,\varphi)}{P_{rad}} = e_{cd} D(\theta,\varphi) \tag{A.8}$$

where $D(\theta,\varphi)$ is the directivity of the antenna and is defined as [3, p. 44]

$$D = \frac{U}{U_0} = \frac{4\pi U}{P_{rad}}. \tag{A.9}$$

U_0 is the radiation intensity of an isotropic source. The directivity gives a description of how much power an antenna directs in a certain direction. If an antenna directs a large portion of its radiated power in a certain direction it will have a large directivity in that direction.

Beamwidth

[3, pp. 42-43]

A parameter often used to describe the radiation pattern of an antenna is the beamwidth. It is the angular separation between two identical points on each side of a maximum. There are several standard beamwidth definitions but in this report only one definition is used, and that is the half-power beamwidth (HPBW). The HPBW is defined as the angular separation between two points on each side of a maximum where the points have half the radiation intensity as the maximum.

The beamwidth is an important parameter when designing a radar antenna. The reason for this is that the beamwidth of the antenna determines the angular resolution of a radar. A smaller HPBW gives better angular resolution. The radar will be better able to separate close targets in the angular dimension.

A.3 Microwave theory

In this section some important topics from microwave theory are presented. First a brief description is given of general transmission lines. Then S-parameters and the Smith chart are presented. S-parameters and the Smith chart are useful tools and have been used excessively in the design of the antenna.

Transmission lines

[5, pp. 47-50]

Transmission lines are important components in a RF-system. In general a transmission line transfers energy from one point to another but it can also be used as a component in filters, matching networks, and so on.

When the frequency is so high that the dimension of the circuit becomes a notable fraction of the wavelength, the lumped circuit theory can no longer be used. Lumped circuit theory assumes that the voltage over the length of a line is constant, but when the frequency is high the amplitude and phase of the voltage will not be constant over the line. In this case transmission line theory must be used to take into account the changing amplitude and phase of the voltage along the line. It is this property (changing amplitude and phase as a function of z, where z is the position on the line) that makes it possible to use a transmission line as a circuit component.

The equations that describe the traveling wave along a line are

$$V(z) = V_0^+ e^{-\gamma z} + V_0^- e^{\gamma z} \tag{A.10}$$

$$I(z) = I_0^+ e^{-\gamma z} + I_0^- e^{\gamma z} \tag{A.11}$$

where V_0^+ and V_0^- are the voltage amplitudes in respectively positive and negative z direction, I_0^+ and I_0^- are the current amplitudes, $e^{-\gamma z}$ describes propagation in positive z direction, and $e^{\gamma z}$ describes propagation in negative direction.

$$\gamma = \alpha + j\beta \tag{A.12}$$

is the propagation constant, α is the attenuation constant and models the loss in the transmission line, and β is the phase constant.

Characteristic impedance
[5, p. 50]

The characteristic impedance of a transmission line is defined as the ratio of the voltage amplitude to the current amplitude

$$Z_0 = \frac{V_0^+}{I_0^+} = -\frac{V_0^-}{I_0^-}. \tag{A.13}$$

The characteristic impedance is constant over the entire length of the transmission line as long as the geometry of the line does not change [4, p. 440].

Terminated transmission line
[5, pp. 56-62]

When a transmission line is terminated in a load, as shown in Figure 60 and $Z_0 \neq Z_L$, some portion of the wave will be reflected by the load.

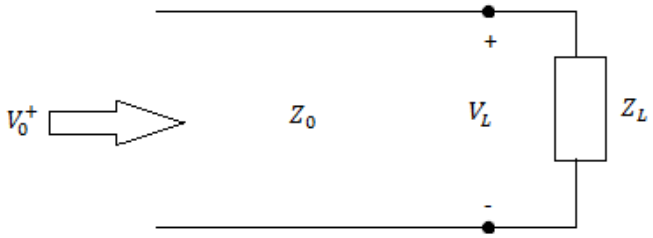

Figure 60: Terminated transmission line

This is because the ratio of the voltage to the current at the terminal is different from the voltage to current ratio on the line since

$$Z_L = \frac{V_L}{I_L} \neq \frac{V_0^+}{I_0^+} = Z_0. \tag{A.14}$$

This means that a part of the incoming wave has to be reflected. A measure of the reflection is the reflection coefficient, defined by

$$\Gamma = \frac{V_0^-}{V_0^+} = \frac{\mathrm{Z_{in}} - \mathrm{Z_0}}{\mathrm{Z_{in}} + \mathrm{Z_0}}. \tag{A.15}$$

When the incident wave and reflected wave combine on the transmission line a standing wave is formed. The voltage standing wave ratio (VSWR) is defined as

$$VSWR = \frac{1 + |\Gamma|}{1 - |\Gamma|} \tag{A.16}$$

and gives the ratio of the maximum voltage amplitude to the minimum voltage amplitude on the transmission line.

S-parameters

[5, pp. 178-179]

S-parameters or the scattering matrix is a standard method for describing microwave networks. It uses voltage waves, both incident, V^+ ,and reflected, V^- to determine the properties of a microwave network. An advantage S-parameters have over other similar methods is that it is easier to measure incident and reflected voltage waves at high frequencies than actual voltages and currents on the terminal.

A two port network is shown in Figure 61.

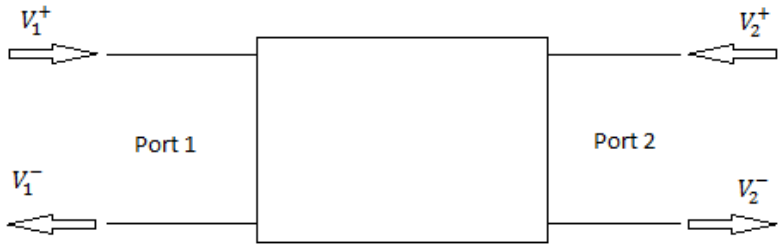

Figure 61: Two port network

This network can be described by the scattering matrix [5, p. 178]

$$\begin{bmatrix} V_1^- \\ V_2^- \end{bmatrix} = \begin{bmatrix} S_{11} & S_{12} \\ S_{21} & S_{22} \end{bmatrix} \begin{bmatrix} V_1^+ \\ V_2^+ \end{bmatrix} \tag{A.17}$$

here V_1^- and V_2^- are the reflected voltage waves from respectively port 1 and port 2, and V_1^+ and V_2^+ are the incident voltage waves on port 1 and port 2. From (A.17) a generalized equation to determine the S-parameters is found

$$S_{ij} = \left. \frac{V_i^-}{V_j^+} \right|_{V_k^+ = 0 \; for \; k \neq j} \tag{A.18}$$

To determine S_{ij} for a N port network one has to excite only port j and then measure at port i, the ports need to be terminated in a match so nothing is reflected back into the network. S_{ij} is the transmission coefficient from port j to port i. S_{ii} is the reflection coefficient at port i. This means that the input impedance at port 1 can be determined from S_{ii} since

$$S_{ii} = \Gamma = \frac{\mathrm{Z_{in}} - \mathrm{Z_0}}{\mathrm{Z_{in}} + \mathrm{Z_0}}. \tag{A.19}$$

The patch antenna in this project is modeled as a one-port network. This means that the only S-parameter is S_{11}. $S_{11}$is an important parameter since it describes the input impedance of the antenna which is the main limiter on the bandwidth.

Smith chart

[5, pp. 63-67]

A very useful tool is the Smith chart, which is a graphical tool showing the reflection coefficient or normalized impedances. It is used for matching of circuits.

The Smith chart is a polar plot of the reflection coefficient $\Gamma=|\Gamma|e^{j\theta}$. The $|\Gamma|$ is the radius plotted from the center of the Smith chart and θ is the phase and is plotted from right to left ($-180° \leq \theta \leq 180°$). Dividing by the characteristic impedance the reflection coefficient can be written as

$$\Gamma = \frac{z_L - 1}{z_L + 1} \tag{A.20}$$

where z_L is the normalized load impedance. z_L can be solved from (A.20)

$$z_L = \frac{1 + |\Gamma|e^{j\theta}}{1 - |\Gamma|e^{j\theta}} \tag{A.21}$$

This means that the Smith chart can be used to convert the voltage reflection coefficient Γ to the normalized load impedance. The resistance part of z_L is plotted along the horizontal circles and the reactance of z_L is plotted on the vertical circles.

The reflection coefficient can be plotted over a range of frequencies in the Smith chart. This gives a good description of the input impedance.

Dielectric Substrates

An important part of the patch antenna is the dielectric substrate. The substrate properties have a large effect on the patch antenna. It is not just a mechanical object that holds the antenna together and makes it practical to produce. Its electrical and thermal properties are important to consider when a desired antenna specification is to be achieved.

Electric properties

Materials can be divided into three different groups according to their electrical properties; conductors, semiconductors and insulators. A dielectric substrate belongs to the latter category. This means that it will not lead any electrical current [4, p. 101]. An insulator can be described by its electric permittivity and magnetic permeability which is defined below for a linear and isotropic insulator;

$$\epsilon = \epsilon_0 \epsilon_r \quad \text{(A.22)}$$

$$\mu = \mu_0 \mu_r \quad \text{(A.23)}$$

$\epsilon_0 \cong 8.854x10^{-12}$ and $\mu_0 = 4\pi x10^{-7}$ is the permittivity and permeability in vacuum. μ_r is the relative permeability and it describes how a material reacts to a magnetic field. For materials considered in this report $\mu_r = 1$. The permeability of the material will therefore not be considered further in this report.

The most common parameter used to describe a dielectric substrate is ϵ_r. It is called the relative permittivity or the dielectric constant. Due to the polarization that occurs inside an insulator when a electric field is applied on the outside of the material, the electric field strength inside the insulator will be weaker than what it would be in vacuum [4, p. 109]. The dielectric constant is related to this effect and therefore describes how the material reacts to an electric field. A high dielectric constant means that strong polarization occurs, which in turn means that the field inside the material is weaker [4, pp. 109-110]. One can say that a material with high dielectric constant stores energy better than a material with low dielectric constant.

Another important parameter used to describe a material is the loss tangent defined as

$$\tan \delta_c \cong \frac{\sigma}{\omega \epsilon} \quad \text{(A.24)}$$

where σ is the conductivity of the material and ω is the frequency [4, p. 342]. The loss tangent describes the power loss in the material. It takes into account both losses due to polarization of the material and ohmic losses [4, p. 342]. It is important to have the loss tangent as low as possible to achieve good antenna efficiency.

Thermal properties

The thermal properties of the substrate are important to consider, specifically when the substrate is used in high power applications. Some of the energy applied to a circuit will be

dissipated as heat. This is due to the loss in the substrate, the finite conductivity of the conductor and electronic components, such as power amplifiers with low efficiencies. One way to decrease the temperature rise is to etch the circuit on a substrate with good thermal properties. Which parameters to consider for good thermal design are presented below.

To minimize the amount of energy dissipated as heat one can reduce the loss in the substrate. This makes the loss tangent a good indicator of the substrates thermal properties. A low loss tangent means that less energy is dissipated as heat due to the losses in the substrate.

Thermal conductivity is another parameter that affects the thermal properties of the substrate. The thermal conductivity describes how good the substrate is to transfer heat. A substrate with high thermal conductivity will cool down quicker than a substrate with low thermal conductivity [24].

Other parameters to consider are the thermal coefficient of the dielectric constant and coefficient of thermal expansion. Atoms in the substrate will behave differently at different temperatures, this can lead to changes in the dielectric constant. The thermal coefficient of the dielectric constant describes how much the dielectric constant will change when the temperature changes. If this is high the antennas properties will vary at different temperatures. The coefficient of thermal expansion describes how much the dimensions of the substrate will change when the temperature changes.

Appendix B: Measurements

B.1 Input impedance

To measure the reflection coefficient a network analyzer was used. Network analyzer was calibrated for a frequency band of 7-10 GHz. Then measurements were conducted. Figure 62 and Figure 63 shows the reflection coefficients of the original antenna element.

Original antenna element

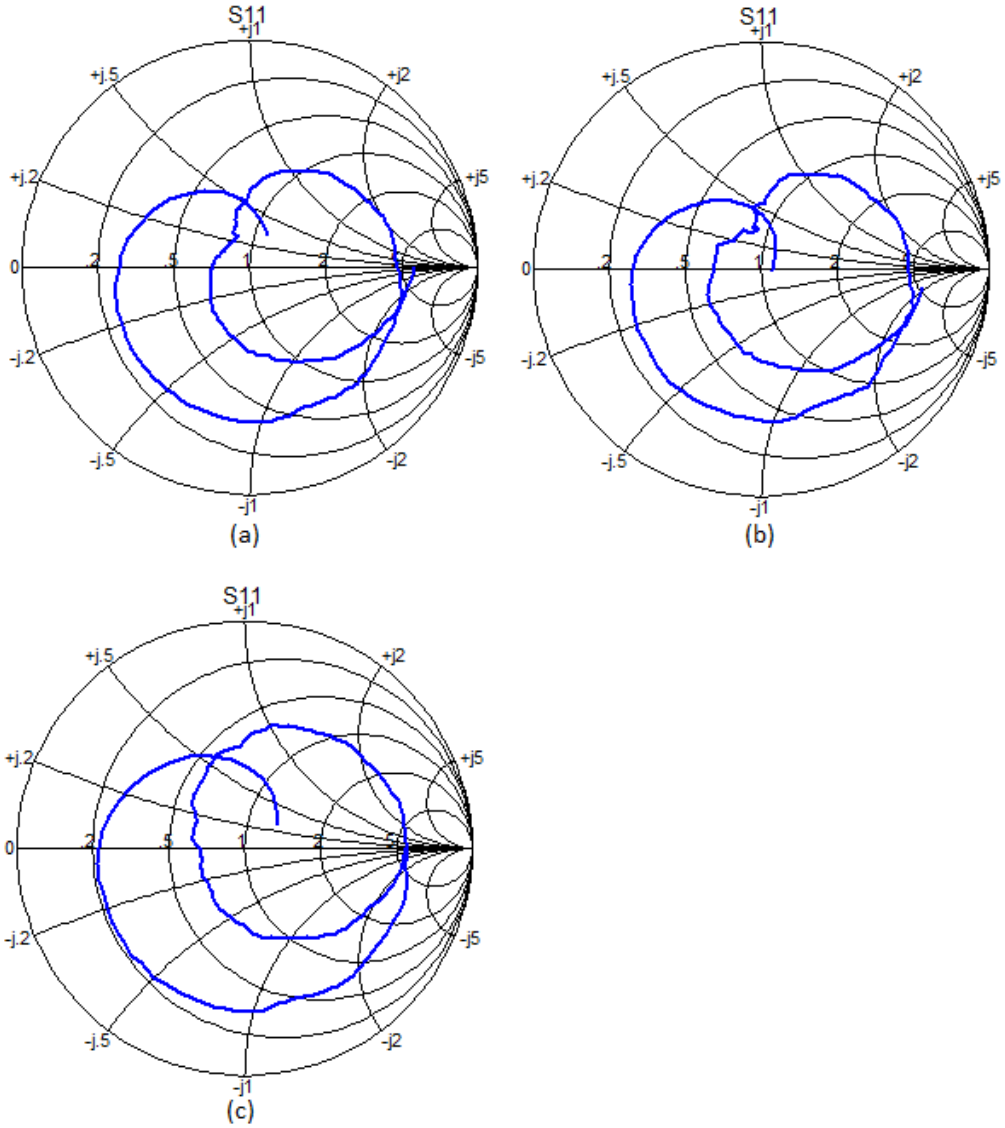

Figure 62: S11 plotted in a Smith chart for a frequency band of 7-10 GHz (a) Antenna 3, (b) Antenna 4, (c) Antenna 5

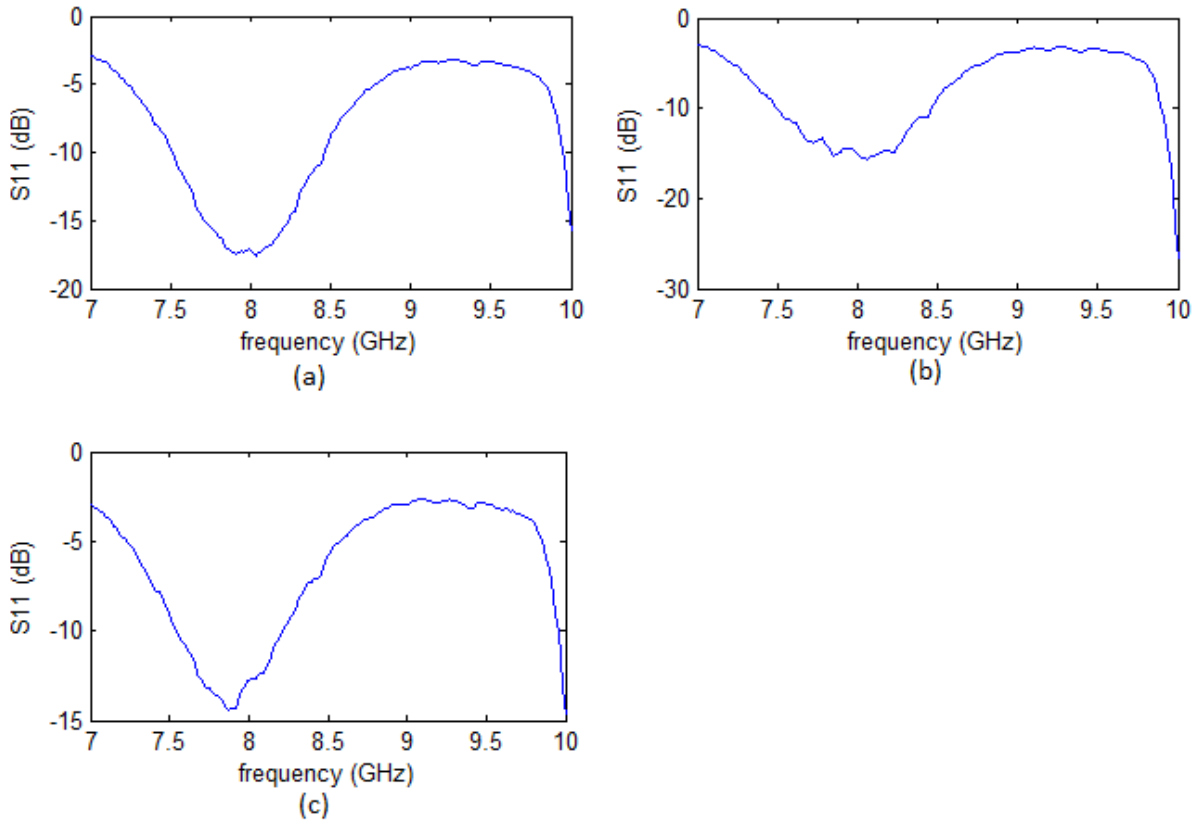

Figure 63: S11 plotted in dB as a function of frequency (a) Antenna 3, (b) Antenna 4, (c) Antenna 5

It is seen in Figure 62 that the loop due to the coupling between the patches is missing. This has led to the center frequency being moved to 8 GHz and the bandwidth is much lower than expected as seen in Figure 63. Comparing the results only small deviations between the antennas are observed. This indicates small process variations.

Modified antenna element

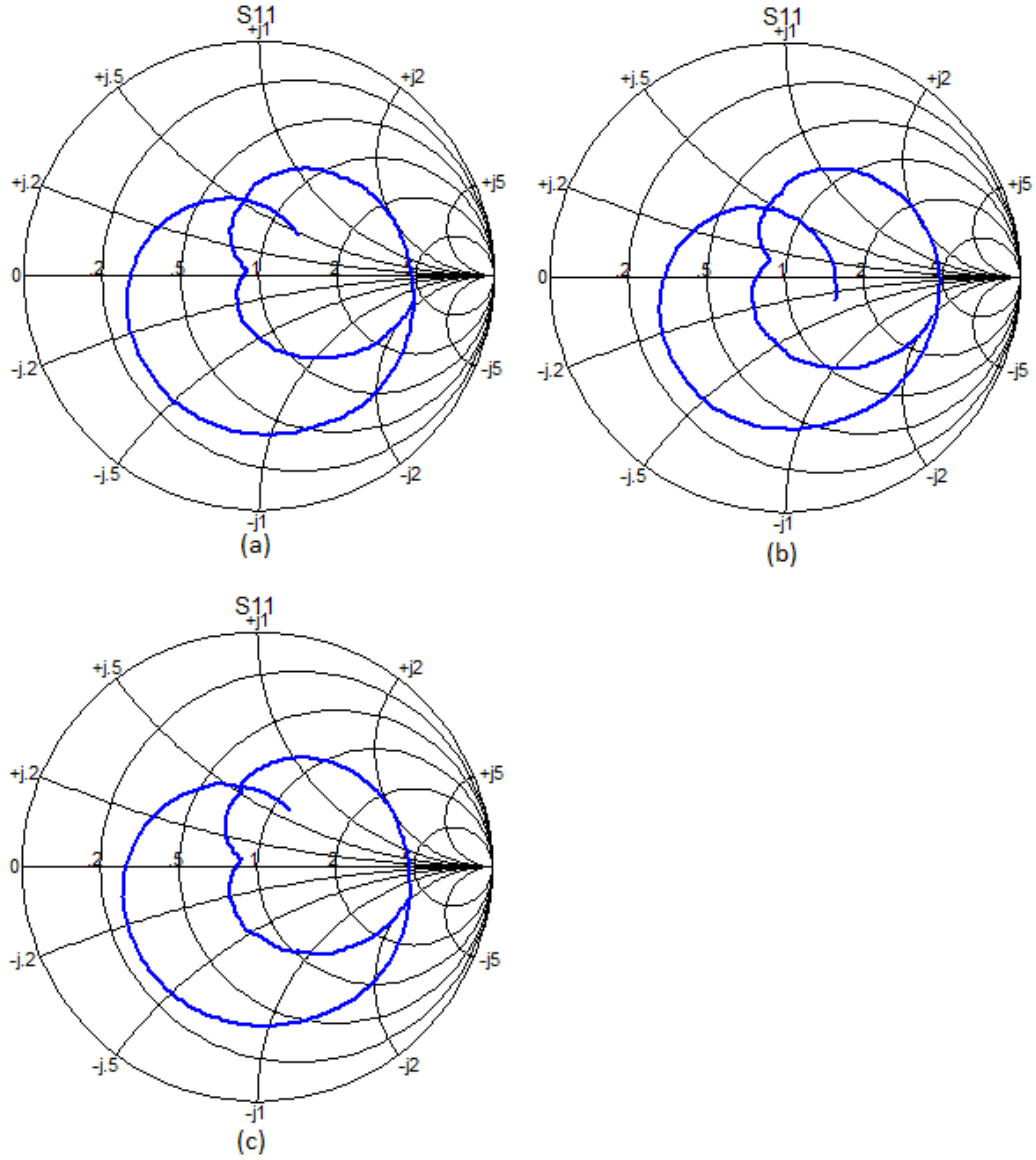

Figure 64: S11of the modified antenna element plotted in a Smith chart for a frequency band of 7-10 GHz (a) Antenna 3, (b) Antenna 4, (c) Antenna 5

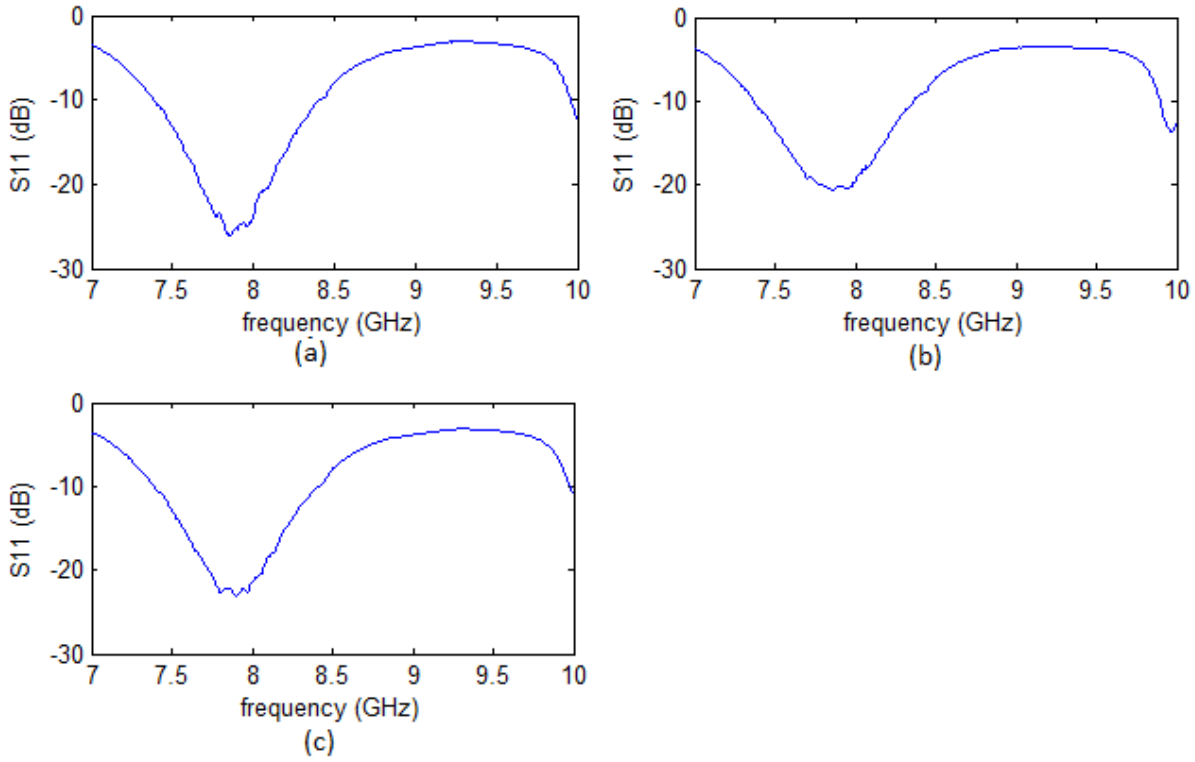

Figure 65: S11 of the modified antenna element plotted in dB as a function of frequency (a) Antenna 3, (b) Antenna 4, (c) Antenna 5

It is seen from Figure 64 that the loop is missing for the modified antenna element. This antenna has a very good match only at the wrong center frequency.

B.2 Radiation patterns

To measure the radiation pattern of the antenna an anechoic chamber was used. The test setup is shown in Figure 66. The antenna under test (AUT) is mounted on a rotating stand across from a reference antenna. This test setup measures the transmission coefficient S21 by exciting the reference antenna and then measuring the power received by the AUT. The AUT is rotated 360°.

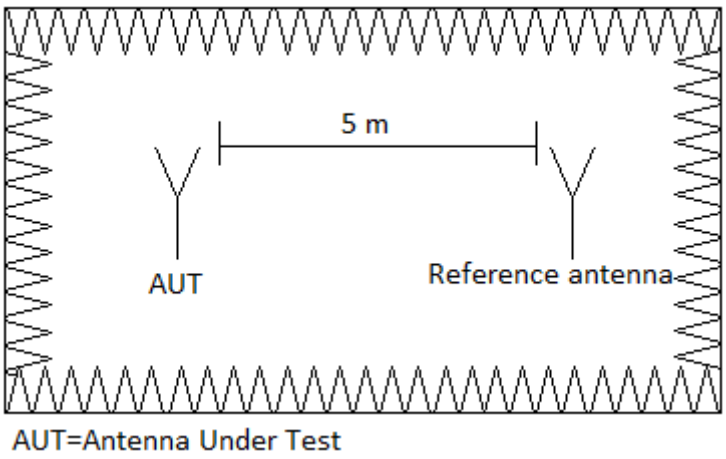

Figure 66: Anechoic chamber

The reference antenna is a broadband horn with linear polarization. This makes it possible to measure both E-plane, H-plane and cross polarization only by turning the reference antenna. measurements was conducted for three frequencies; 8, 8,25 and 8,50 GHz. A sample of the measured results are presented here. The results are plotted in normalized dB.

Original antenna element

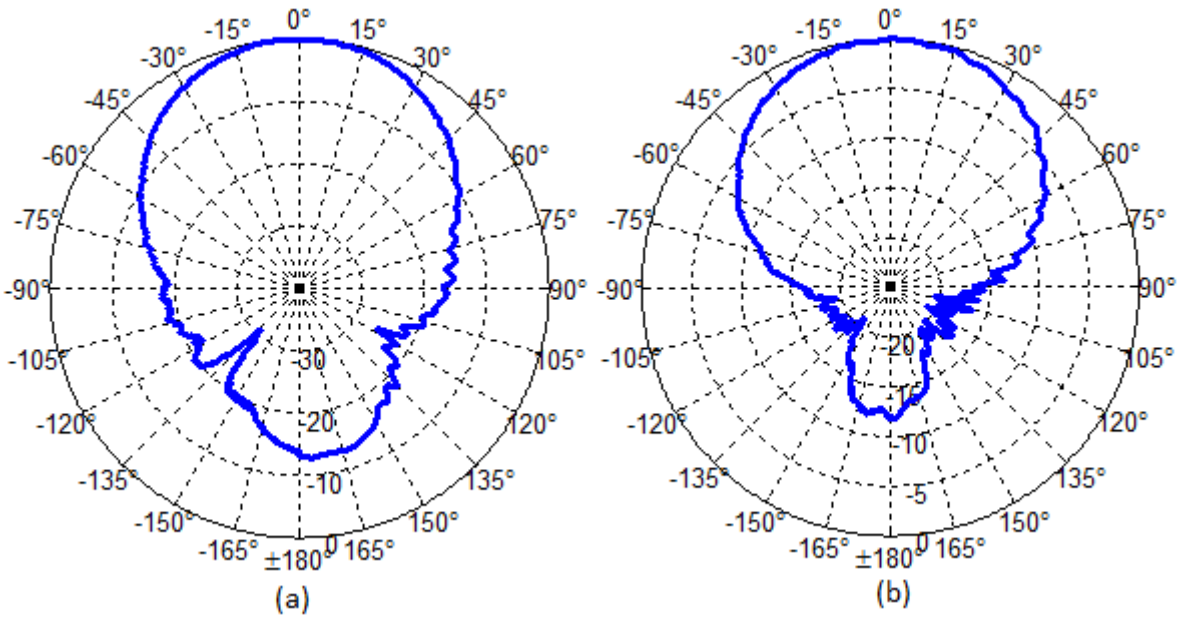

Figure 67: Antenna 4 at 8.25 GHz in normalized dB, (a) E-plane, (b) H-plane

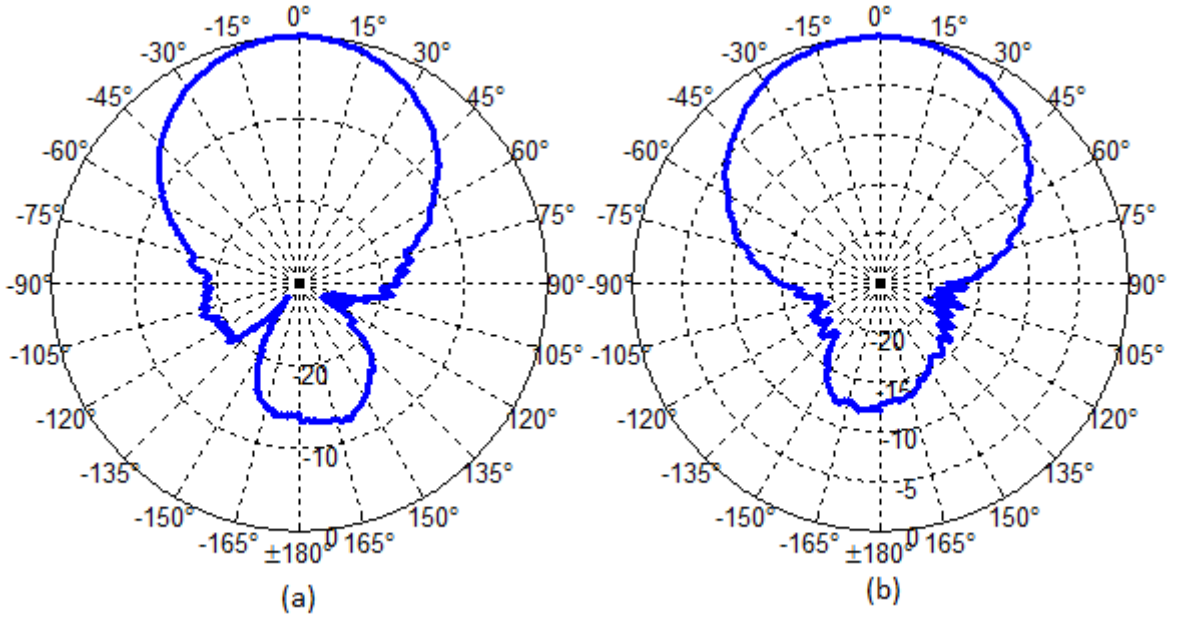

Figure 68: Antenna 3 at 8.5 GHz in normalized dB, (a) E-plane, (b) H-plane

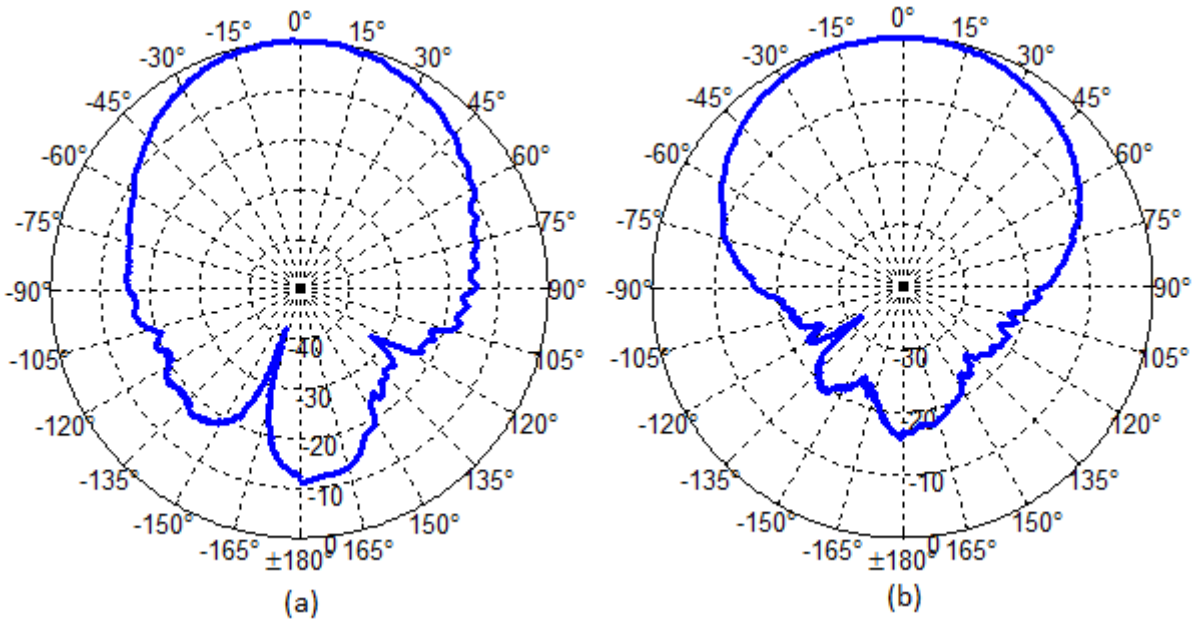

Figure 69: Radiation pattern for the Antenna 3 at 8.5 GHz in normalized dB, (a) E-plane, (b) H-plane

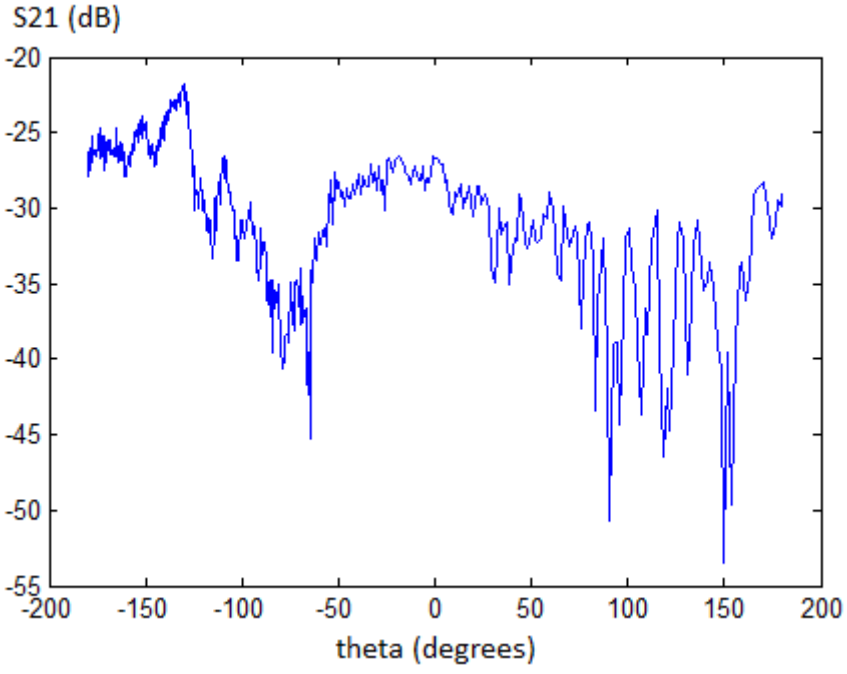

Figure 70: Cross polarization for antenna 4 at 8.25 GHz

Modified antenna element

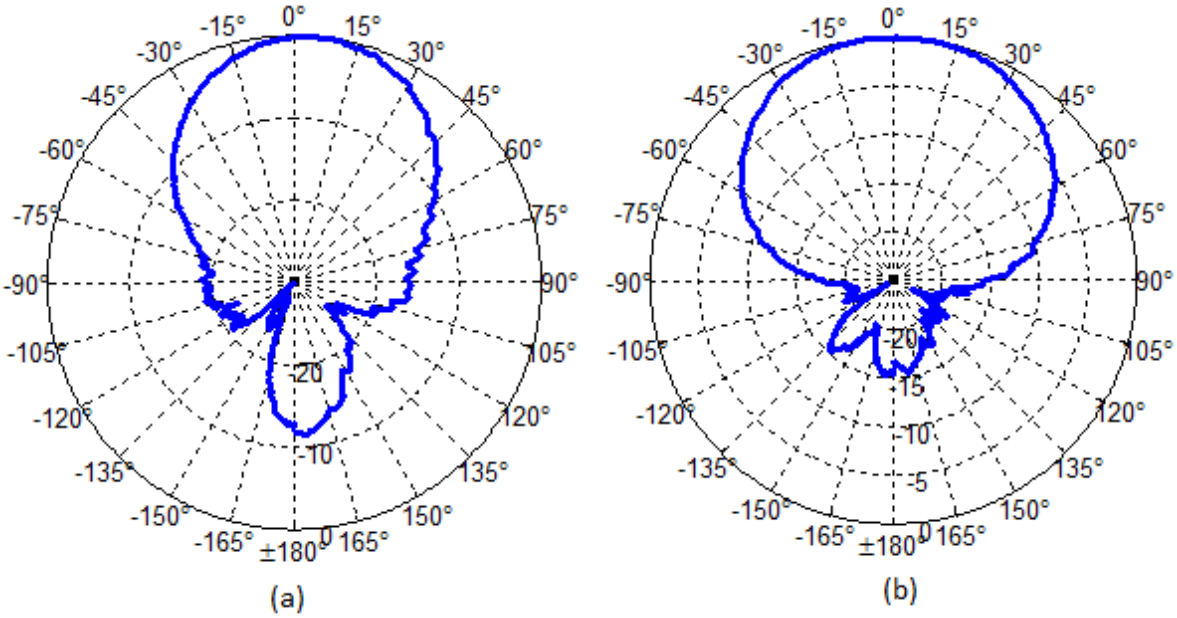

Figure 71: Radiation pattern for antenna 4 at 8.25 GHz in normalized dB, (a) E-plane, (b) H-plane

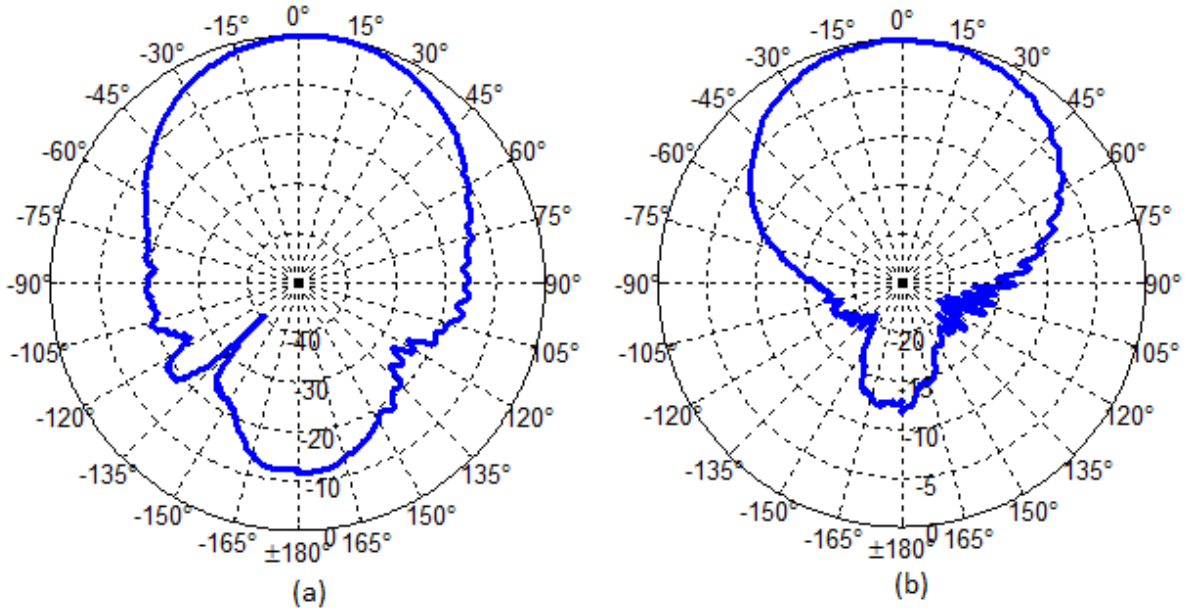

Figure 72: Radiation pattern for antenna 5 at 8.25 GHz in normalized dB, (a) E-plane, (b) H-plane

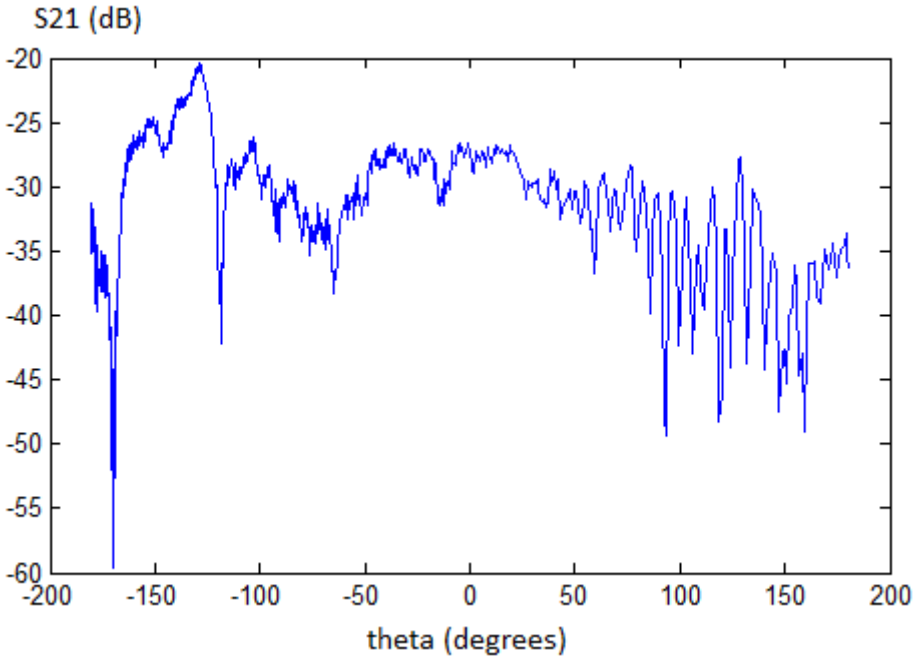

Figure 73: Cross polarization of antenna 5 at 8.25 GHz

Appendix C: Simulation results

C.1 Radiation patterns

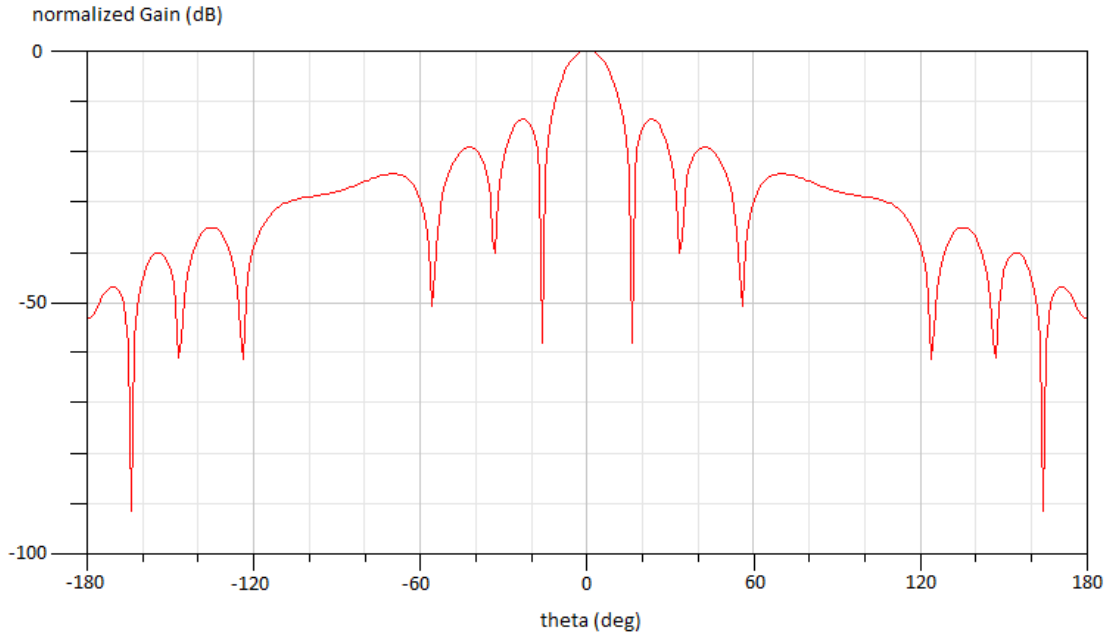

Figure 74: Rectangular plot of the normalized antenna gain in dB for the array scanned in $\theta_S = 0°$ (f= 8.25 GHz). Plotted in $\varphi = 0°$ plane.

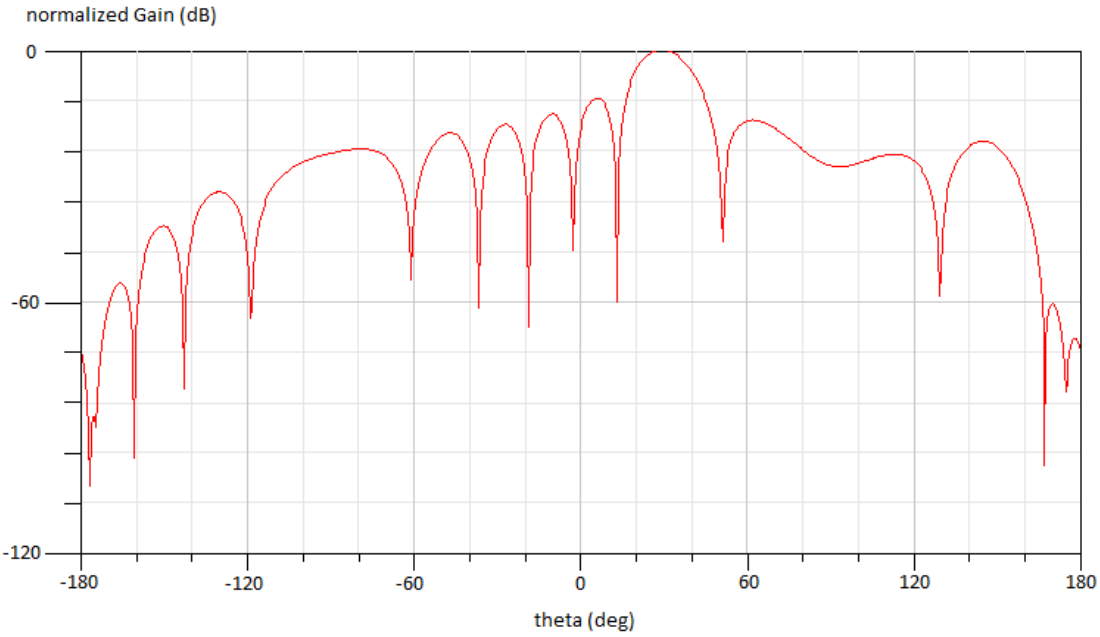

Figure 75: Rectangular plot of the normalized antenna gain in dB for the array scanned in$\theta_S = 30°$ (f= 8.25 GHz). Plotted in φ=0° plane.

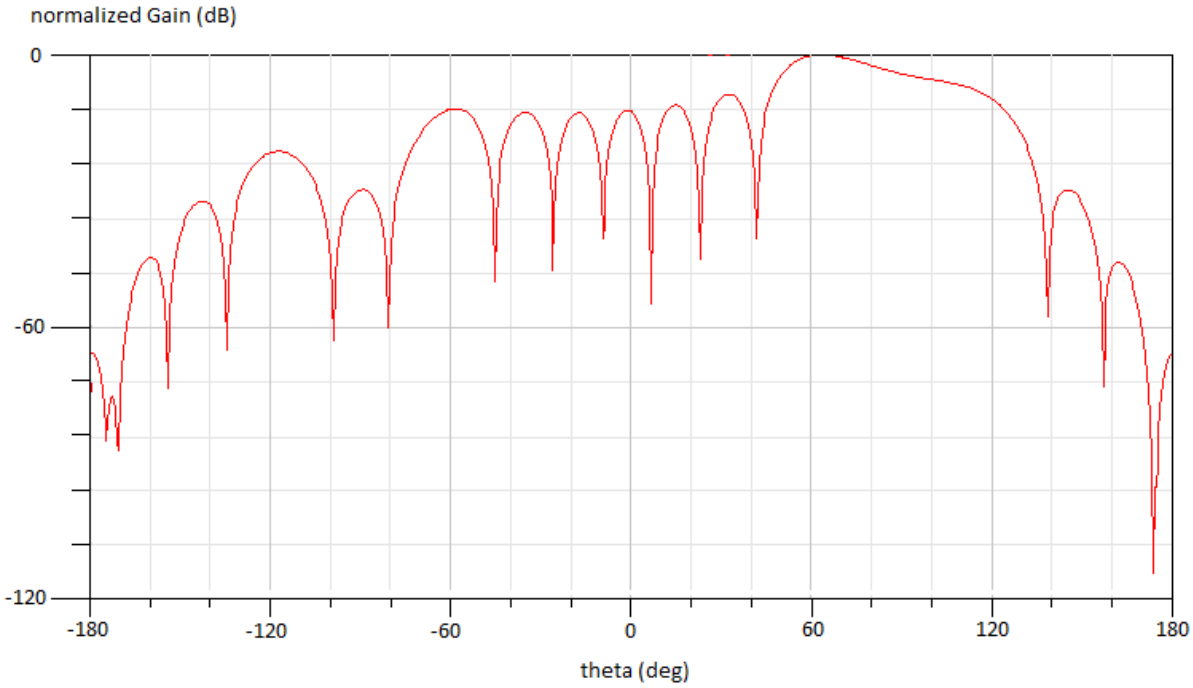

Figure 76: Rectangular plot of the normalized antenna gain in dB for the array scanned in $\theta_S = 70°$ (f= 8.25 GHz). Plotted in φ=0° plane.

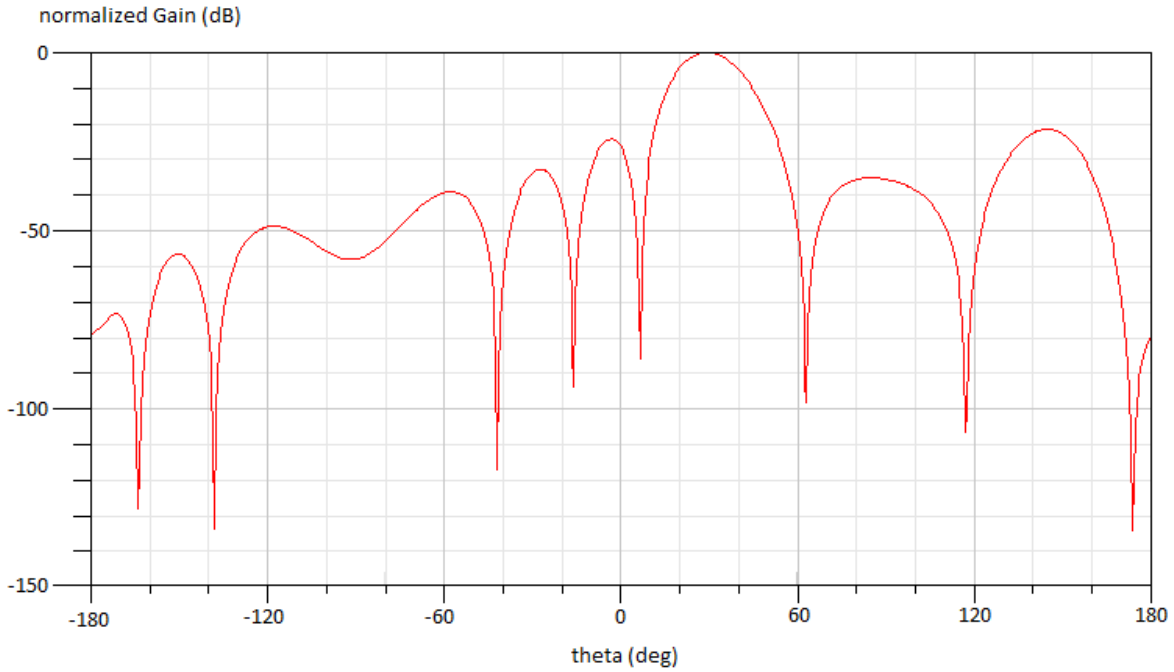

Figure 77: Rectangular plot of the normalized antenna gain in dB for the array scanned in $\theta_S = 30°$ and $\varphi_S = 45°$ (f= 8.25 GHz). Plotted in φ=45° plane.

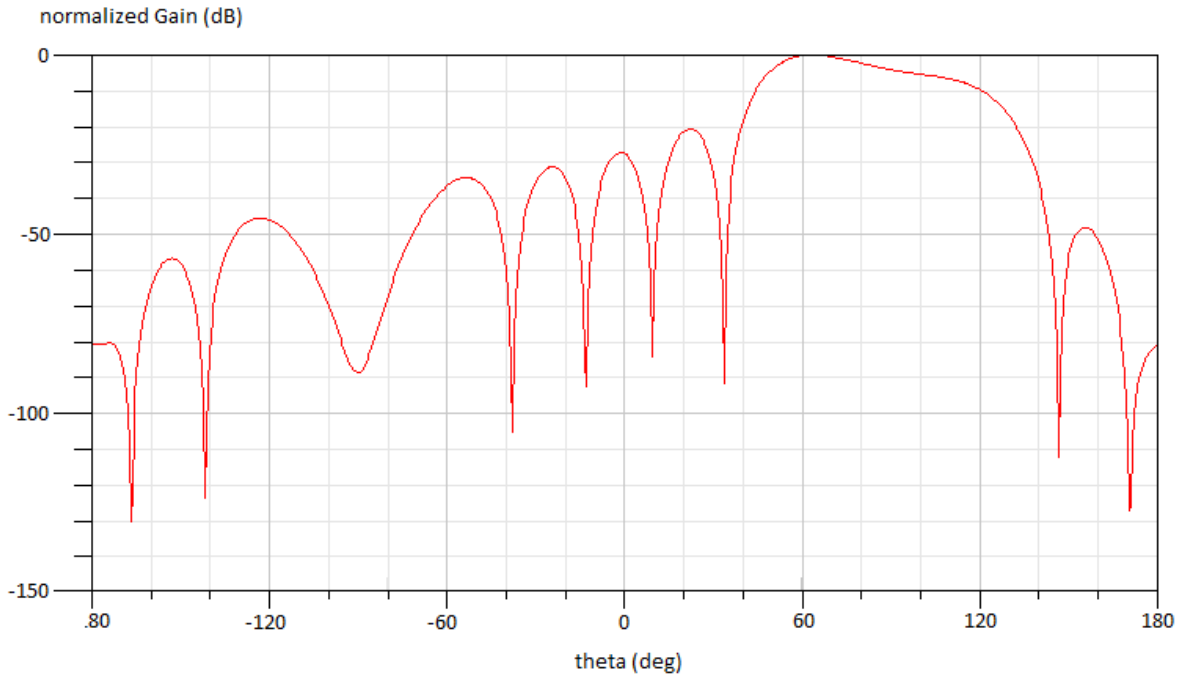

Figure 78: Rectangular plot of the normalized antenna gain in dB for the array scanned in$\theta_S = 70°$ and $\varphi_S = 45°$ (f= 8.25 GHz). Plotted in φ=45° plane.

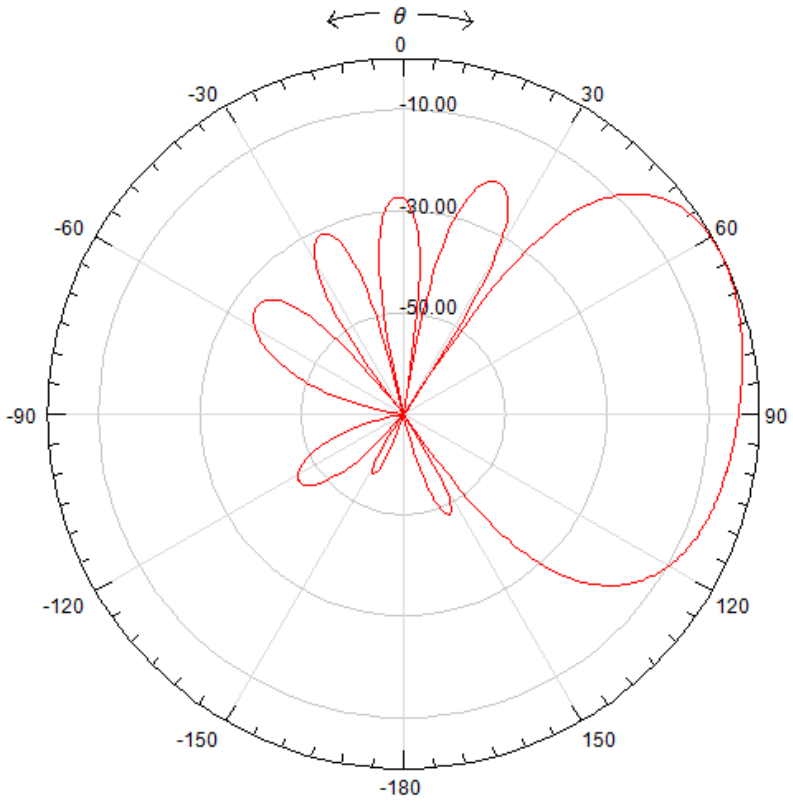

Figure 79: Polar plot of the normalized antenna gain in dB for the array scanned in$\theta_S = 70°$ and $\varphi_S = 45°$ (f= 8.25 GHz). Plotted in φ=45° plane.

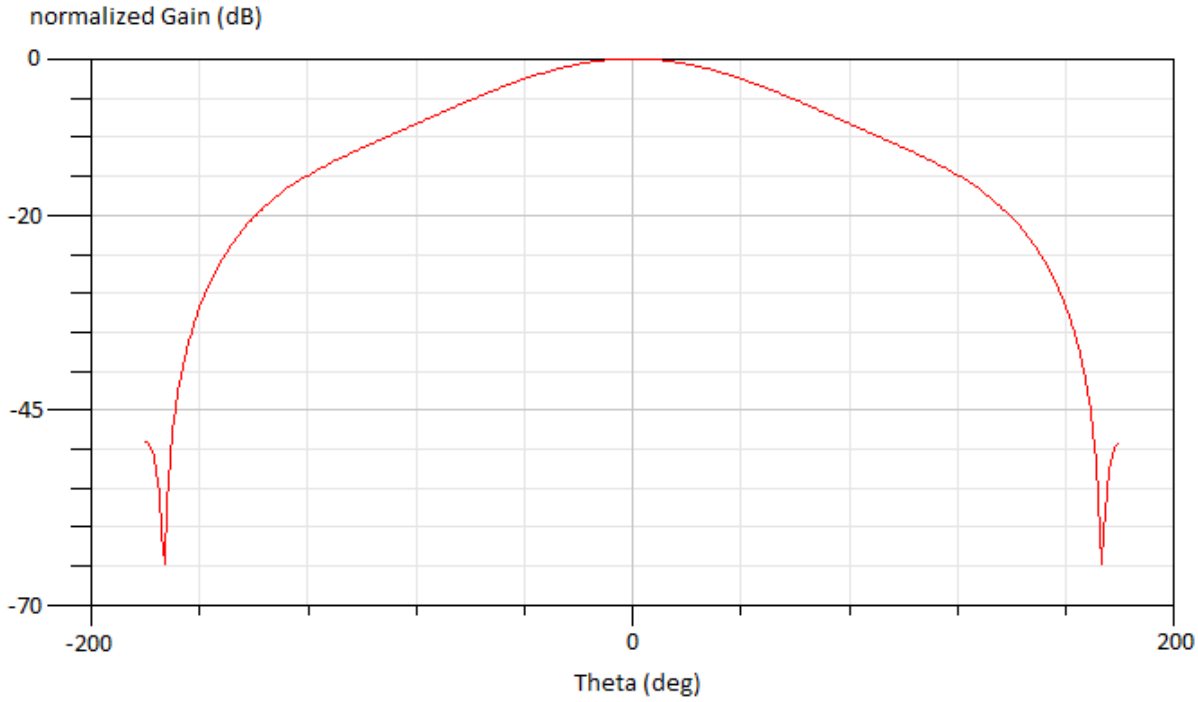

Figure 80: Rectangular plot of the normalized antenna gain in dB for an antenna element in an infinite array environment. φ=0°

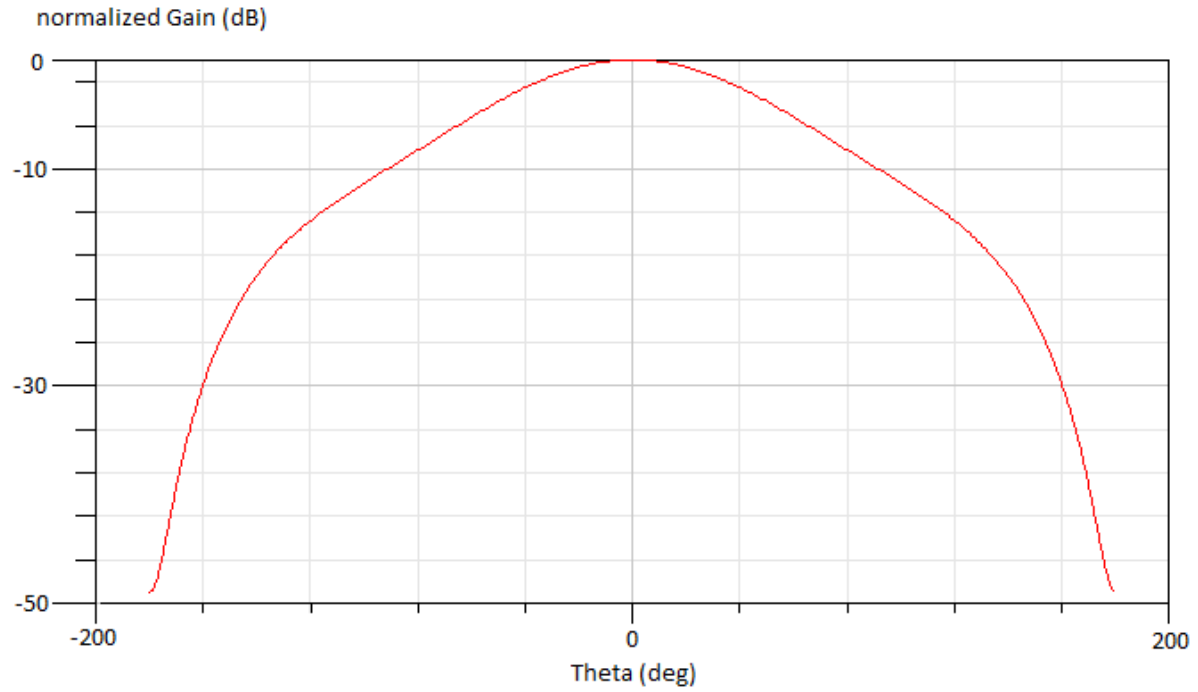

Figure 81: Rectangular plot of the normalized antenna gain in dB for an antenna element in an infinite array environment. φ=90°

Appendix D: Schematic

Table 10: Values for the schematic

Parameter	**Value [mm]**
L	16.5
W	16.5
L1	8
W1	7.5
L2	10.5
W2	8
Ls	9.5
L_st	2.8
W_st	2.8
L_sl	4.5
W_sl	0.5
L_c	6.3
W_c	11
R_t	1.5
R1	0.2
R2	0.3
R3	0.635
d1	1.1
d2	0.7
Copper thickness	$35 * 10^{-3}$

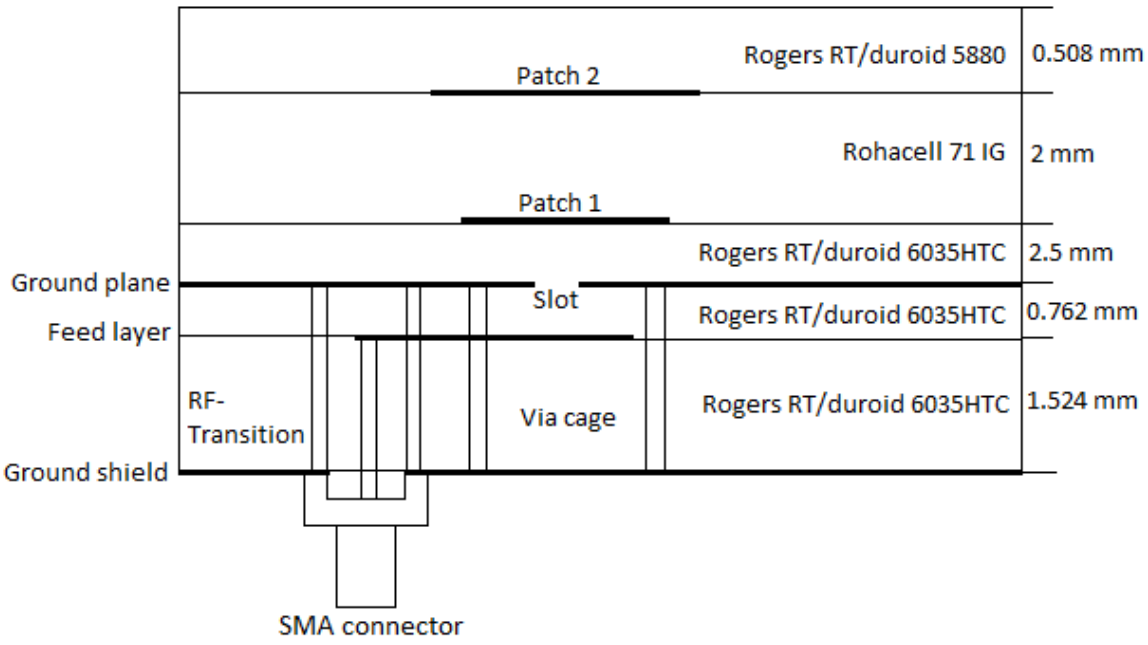

Figure 82: Side view of antenna

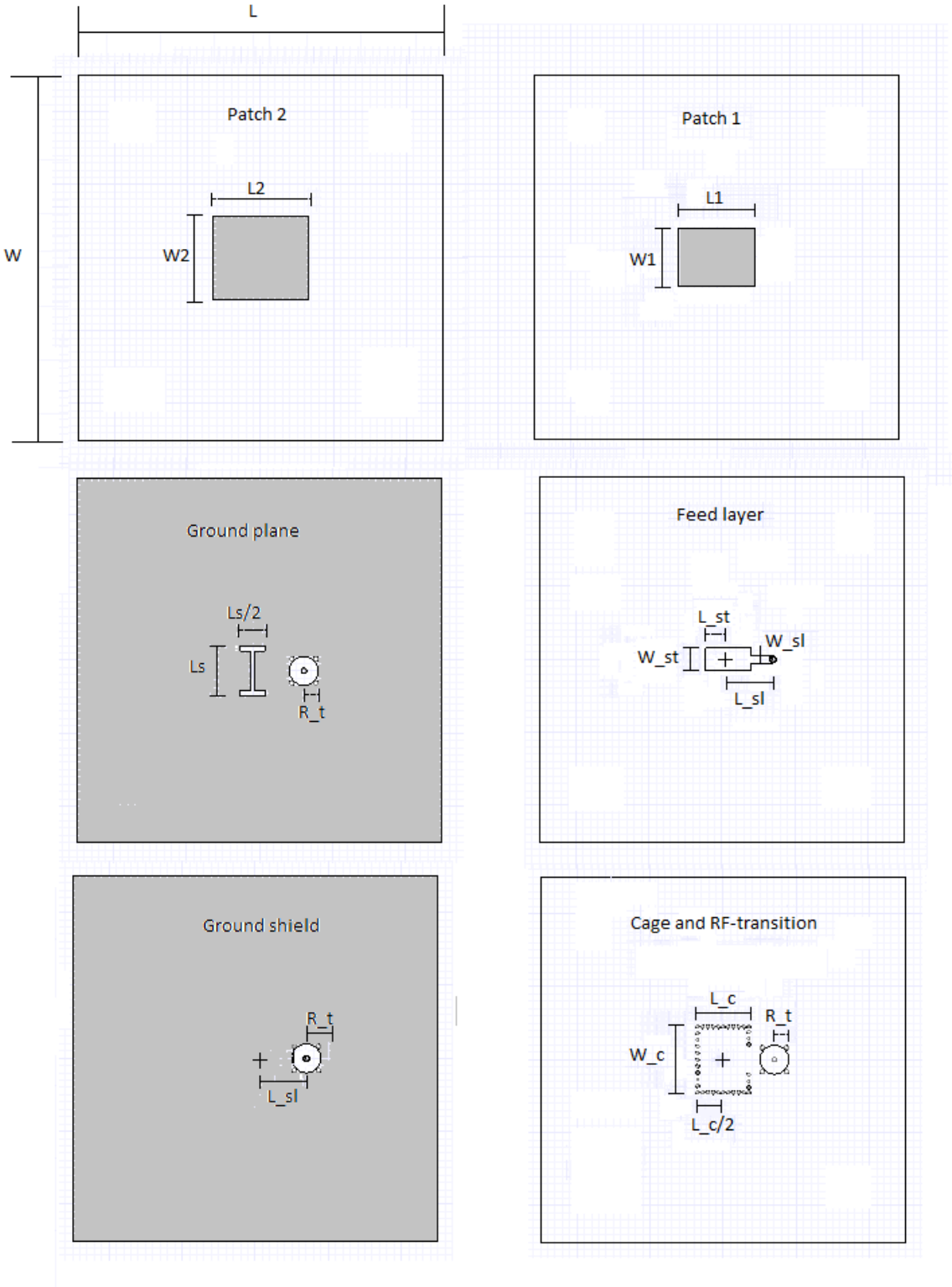

Figure 83: Schematics of the antenna element

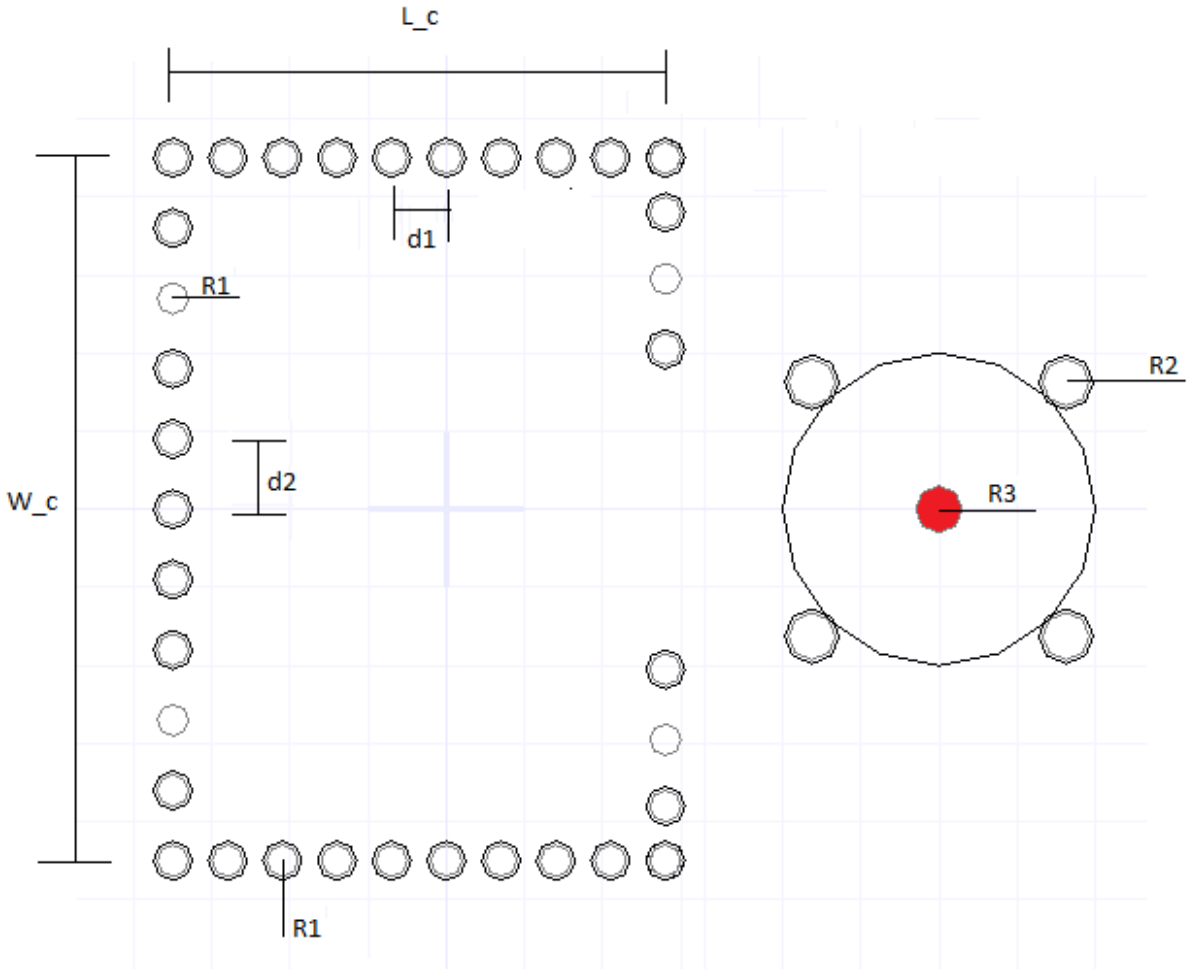

Figure 84: Cage and RF-Transition. Red vias go from ground shield to feed layer. White vias go from ground shield to ground plane

.

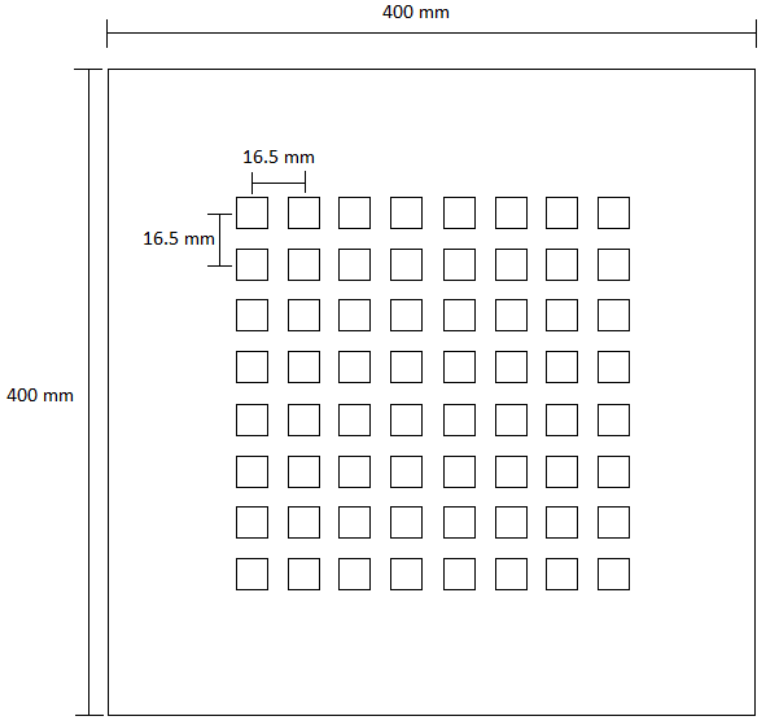

Figure 85: Schematic of the array

Appendix E: Derivations

The propagation direction relative to the z-axis for a Floquet mode is given as [2, p. 73]

$$\tan\theta_n = \frac{\frac{2n\pi+\beta}{d}}{\sqrt{k_0^2 - \left(\frac{2n\pi+\beta}{d}\right)^2}} \tag{E.1}$$

where β is the phase difference and d is the element spacing. Multiple steps are taken to simplify this equation.

$$\tan^2\theta_n = \frac{(2n\pi+\beta)^2}{d^2k_0^2 - (2n\pi+\beta)^2} \tag{E.2}$$

$$\tan^2\theta_n\,(d^2k_0^2 - (2n\pi+\beta)^2) = (2n\pi+\beta)^2 \tag{E.3}$$

$$d^2k_0^2\tan^2\theta_n = (2n\pi+\beta)^2\,(1+\tan^2\theta_n) \tag{E.4}$$

Inserting $\frac{\sin\theta}{\cos\theta}$ for $tan\,\theta$.

$$d^2k_0^2\,\frac{\sin^2\theta_n}{\cos^2\theta_n} = (2n\pi+\beta)^2\left(1+\frac{\sin^2\theta_n}{\cos^2\theta_n}\right) \tag{E.5}$$

Then $\sin^2\theta + \cos^2\theta = 1$ is used

$$d^2k_0^2\,\frac{\sin^2\theta_n}{1-\sin^2\theta_n} = (2n\pi+\beta)^2\left(1+\frac{\sin^2\theta_n}{1-\sin^2\theta_n}\right) \tag{E.6}$$

Solving with respect to θ_n gives

$$d^2k_0^2\,\frac{\sin^2\theta_n}{1-\sin^2\theta_n} = (2n\pi+\beta)^2\left(\frac{1}{1-\sin^2\theta_n}\right) \tag{E.7}$$

$$d^2k_0^2\,\sin^2\theta_n = (2n\pi+\beta)^2 \tag{E.8}$$

$$\sin\theta_n = \pm\frac{2n\pi+\beta}{dk_0} \tag{E.9}$$